

**Studies of photoluminescence characteristics of
 β -Ga₂O₃ and In₂O₃ nanostructures deposited by
different growth techniques**

By
Ravindra Jangir
(PHYS03201004002)

Raja Ramanna Centre for Advanced Technology
Indore-452013
India

A thesis submitted to the
Board of Studies in Physical Sciences
In partial fulfillment of requirements
for the Degree of
DOCTOR OF PHILOSOPHY
of
HOMI BHABHA NATIONAL INSTITUTE

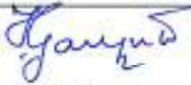
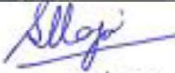
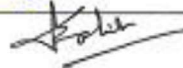
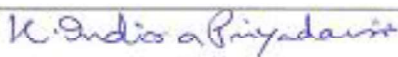
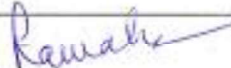


August, 2016

Homi Bhabha National Institute

Recommendations of the Viva Voce Committee

As members of the Viva Voce Committee, we certify that we have read the dissertation prepared by **Ravindra Jangir** entitled "**Studies of photoluminescence characteristics of β -Ga₂O₃ and In₂O₃ nanostructures deposited by different growth techniques**" and recommend that it may be accepted as fulfilling the thesis requirement for the award of Degree of Doctor of Philosophy.

Chairman – Dr. P. K. Gupta		Date: 1/03/18
Guide– Dr. Tapas Ganguli		Date: 01/03/2018
Examiner - Prof. S.S. Major		Date: 20/3/2018
Member 1- Dr. D. K. Palit		Date: 01/03/2018
Member 2- Dr. I. Priyadarshini		Date: 01/03/2018
Member 3- Dr. Rama Chari		Date: 1-3-18
Member 4- Dr. Kaustuv Das		Date: 01/03/18
Member 5- Dr. Alok Dube		Date: 01/03/18
External Member - Dr. S. N. Jha		Date: 01/03/18

Final approval and acceptance of this thesis is contingent upon the candidate's submission of the final copies of the thesis to HBNI.

I hereby certify that I have read this thesis prepared under my direction and recommend that it may be accepted as fulfilling the thesis requirement.

Date: 01-03-2018

Place: Indore

Guide: 
(Dr. Tapas Ganguli)

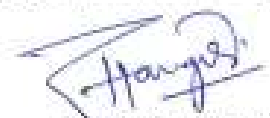
ACKNOWLEDGEMENTS

I would like to express my sincere gratitude to my thesis guide Dr. Tapas Ganguli for his faith, guidance and support throughout the course. I was benefited a lot from his guidance including the discussion we held, the intelligent suggestions he made on my research, his patience on correcting my papers, and his helpful instruction on my presentations and seminars. I am also grateful to him for being patient while critically reviewing this thesis.

I also gratefully acknowledge the help rendered by all the members of Semiconductor Laser Section (SCLS) and Material Research Lab (MRL), RRCAT. I would like to thank all my friends and colleagues especially Dr. Salahuddin Khan, Dr. C. Kamal, for their support and help. It gives me immense pleasure to thank the members of the doctoral committee Prof. P. K. Gupta (Chairman), Dr. D. K. Aswal, Dr. D. K. Palit, Dr. Indira Priyadarshini, Dr. Rama Chari, Dr. S.N.Jha, Dr. Kaustav Das and Dr. Alok Dubey for their critical review and suggestions during the progress review and pre-synopsis viva-voce.

I would like to thank to all my collaborators, Dr. S. K. Rai, Dr. A. K. Srivastava, Smt. Pragya Tiwari, Shri Himanshu Srivastava, Shri Sanjay Porwal, Shri Puspen Mondal and Shri B. Q. Khattak, for their help on performing the experiments and many insightful discussion regarding the experimental results. I would also like to thank to Dr. P. A. Naik Head ISUD, Dr. S. M. Oak, former Head SSLD, Dr. S. K. Deb and Dr. G. S. Lodha, former Head ISUD and Dr P. D. Gupta, former Director, RRCAT for their constant support and encouragement during the course.

Finally, but the most important acknowledgement is to my parent, my wife and my two little daughters for their wholehearted love, unconditional support, understanding, patience and encouragements.


Ravindra Jangir

DEDICATIONS

*This thesis is dedicated to my Parents and my Family
For their endless love, support and encouragement.....*

5. *Photoluminescence study of β -Ga₂O₃ nanostructures under different oxygen pressure conditions*
R. Jangir, S. Porwal, P. Tiwari, S. K. Rai, P. Mondal, T. Ganguli, S. M. Oak, S. K. Deb
AIP Conf. Proc. (2013), 1512, 212.
6. *Study the effect of annealing in different environment on the optical properties of β -Ga₂O₃ nanostructures*
R. Jangir, T. Ganguli, S. Porwal, P. Tiwari, S. K. Rai, A. K. Srivastava, P. Mondal, S. K. Deb
AIP conf. Proc. (2012), 1447, 271.
7. *Facile synthesis and characterization of β -Ga₂O₃ Nanostructures via Vapor Transport Method*
R. Jangir, T. Ganguli, P. Tiwari, H. Srivastava, S. K. Rai, A. K. Das, L. M. Kukreja, S. M. Oak
AIP conf. Proc. (2011), 1349, 373.
8. *Synthesis and characterization of β - Ga₂O₃ nanostructures grown on GaAs substrates*
R. Jangir, T. Ganguli, P. Tiwari, S. Porwal, H. Srivastava, S. K. Rai, S. M. Oak
Proc. of NLS-19, Dec. (2010).



Ravindra Jangir

List of Publications arising from the thesis

Journal

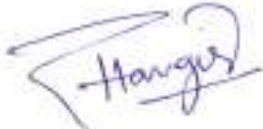
1. *Correlation between surface modification and photoluminescence properties of β -Ga₂O₃ nanostructures*
R. Jangir, S. Porwal, P. Tiwari, P. Mondal, S. K. Rai, A. K. rivastava, I. Bhaumik, T. Ganguli
AIP Advances (2016), 6, 035120.
2. *Applicability of Langmuir equation to oxygen pressure dependent Photoluminescence from β -Ga₂O₃ nanostructures*
R. Jangir, T. Ganguli, S. Porwal, P. Tiwari, S. K. Rai, I. Bhaumik, L. M. Kukreja, P. K. Gupta, S. K. Deb
J. App. Phys. (2013), 114, 074309.
3. *Photoluminescence study of β -Ga₂O₃ nanostructures annealed in different environments*
R. Jangir, S. Porwal, P. Tiwari, P. Mondal, S. K. Rai, T. Ganguli, S. M. Oak, S. K. Deb
J. App. Phys. (2012), 112, 034307.
4. *Synthesis and characterization of β -Ga₂O₃ nanostructures grown on GaAs substrates*
R. Jangir, T. Ganguli, P. Tiwari, S. Porwal, H. Srivastava, S. K. Rai, B. Q. Khattak, S. M. Oak
Applied Surface Science (2011), 257, 9323-9328.

Conferences

1. *Effect of growth parameters in controlling the growth direction of In₂O₃ micro/nanowires* R. Jangir, P. Tiwari, S. K. Rai and Tapas Ganguli 61th DAE-SSPS (2016) KIIT Univ., Bhubaneswar, Odisha Dec. 26-30.
2. *Effect of moisture on oxygen sensing properties of β -Ga₂O₃ nanostructures*
R. Jangir, S. Porwal, P. Tiwari, S. K. Rai, P. Mondal, T. Ganguli
Condensed Matter Physics under Extreme Conditions” (CoMPEC-2016) April 13-16, (2016).
3. *Study of O₂ sensitive photoluminescence of β -Ga₂O₃ nanostructures annealed in moist environments*
R. Jangir, S. Porwal, P. Tiwari, S. K. Rai and Tapas Ganguli
AIP Conf. Proc. (2016), 1731, 050082.
4. *Effect of initial nucleation on the growth direction of In₂O₃ micro/nanowires*
R. Jangir, S. Porwal, P. Tiwari, S. K. Rai, P. Mondal, T. Ganguli
Proc. of NLS-24, December 2-5, (2015).

DECLARATION

I, hereby declare that the investigation presented in the thesis has been carried out by me. The work is original and has not been submitted earlier as a whole or in part for a degree / diploma at this or any other Institution / University.

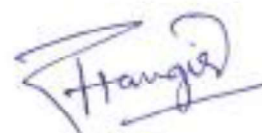


Ravindra Jangir

STATEMENT BY AUTHOR

This dissertation has been submitted in partial fulfillment of requirements for an advanced degree at Homi Bhabha National Institute (HBNI) and is deposited in the Library to be made available to borrowers under rules of the HBNI.

Brief quotations from this dissertation are allowable without special permission, provided that accurate acknowledgement of source is made. Requests for permission for extended quotation from or reproduction of this manuscript in whole or in part may be granted by the Competent Authority of HBNI when in his or her judgment the proposed use of the material is in the interests of scholarship. In all other instances, however, permission must be obtained from the author.



Ravindra Jangir

1.3 XRD and SEM results	77
1.4 Effect of annealing on the PL Properties	79
1.5 Discussion on the changes observed in the PL properties	82
1.6 Summary.....	84
Chapter 6: Synthesis and characterization of β-Ga₂O₃ nanostructures grown on GaAs substrates.....	85-91
6.1 Motivation of the work	85
6.2 Experimental procedure.....	85
6.3 XRD and SEM results	86
6.4 Optical characterization.....	87
6.4.1 Optical absorption properties.....	87
6.4.2 Photoluminescence properties.....	88
6.5 Summary.....	91
Chapter 7: Influence of growth parameters on the morphology and growth orientation of In₂O₃ wires.....	92-109
7.1 Introduction and background.....	92
7.2 Experimental method.....	93
7.3 XRD results.....	96
7.4 SEM results and growth mechanism.....	97
7.5 Discussion on the TEM results and growth orientation of In ₂ O ₃ micro/nano wires.....	103
7.6 PL results.....	107
7.7 Summary.....	109
Chapter 8: Summary and future scope.....	110-115
References.....	116-127

2.3.1.3 X-ray diffraction.....	35
2.3.2 Optical characterization.....	37
2.3.2.1 Absorption spectroscopy.....	37
2.3.2.2 Photoluminescence spectroscopy.....	38
Chapter 3: Dependence of PL from β-Ga₂O₃ nanostructures on oxygen pressure	43-57
3.1 Introduction and background.....	43
3.2 Experimental procedure.....	44
3.3 Structural properties and growth mechanism.....	44
3.4 Effect of O ₂ adsorption/desorption on the PL properties.....	47
3.5 Discussion on the mechanism of PL.....	51
3.6 Summary.....	57
Chapter 4: Study of different growth techniques and optimization of the growth parameters.....	58-75
4.1 Motivation of the work.....	58
4.2 Experimental procedure.....	59
4.3 Structural characterization and growth mechanisms.....	61
4.4 Comparison of PL results	67
4.5 Discussion on the observed PL results.....	70
4.6 Effect of surface defects on the O ₂ partial pressure dependent PL behavior.....	73
4.7 Summary.....	74
Chapter 5: Effect of post growth annealing of β-Ga₂O₃ nanostructures in different environments on the photoluminescence properties.....	76-84
1.1 Introduction and background.....	76
1.2 Experimental procedure.....	76

CONTENTS

	Page No.
Synopsis.....	01
List of figures.....	11
List of tables.....	16
Chapter 1: Introduction.....	17-27
1.1 One dimensional nanostructures.....	17
1.2 Nanostructure fabrication approaches.....	18
1.3 Metal oxide nanostructures and their applications.....	19
1.3.1 Light emitting devices.....	19
1.3.2 Field emission devices.....	20
1.3.3 Photo detector devices.....	20
1.3.4 Optical resonator devices.....	21
1.3.5 Sensor devices.....	22
1.4 Motivation of the thesis.....	24
1.5 Organization of the thesis.....	25
Chapter 2: Experimental techniques and procedures.....	28-42
2.1 Synthesis methods of metal oxide nanostructures.....	28
2.1.1 Vapor phase growth method.....	28
2.2 Growth mechanisms.....	30
2.2.1 Vapor–liquid–solid mechanism.....	30
2.2.2 Vapor–solid mechanism.....	32
2.3 Characterization techniques.....	32
2.3.1 Structural characterization.....	32
2.3.1.1 Scanning electron microscopy.....	32
2.3.1.2 Transmission electron microscopy.....	34

19. J.S. Jeong, J.Y. Lee, C.J. Lee, S.J. An and G.-C. Yi, Chem. Phys. Lett. 384, 246 (2004)
20. S.M. Prokes, W.E. Carlos and E.R. Glaser, Int. J. Nanotech.. 5, 475 (2008).
21. Z. Liu, T. Yamazaki, Y. Shen, T. Kikuta, N. Nakatani, Y. Li, Sensors and Actuators B 129, 666 (2008)

- (2006)
7. E. Joanni, R. Savu, L. Valadares, M. Cilense, and M. A. Zaghete, *Rev. Sci. Instrum.* **82**, 065101 (2011)
 8. P. Feng, X. Y. Xue, Y. G. Liu, Q. Wan, and T. H. Wang, *Appl. Phys. Lett.* **89**, 112114 (2006)
 9. E. Nogales, J. Á. García, B. Méndez and J. Piqueras, *Appl. Phys. Lett.* **91**, 133108 (2007)
 10. Y. P. Song, H. Z. Zhang, C. Lin, Y. W. Zhu, G. H. Li, F. H. Yang, and D. P. Yu, *Phys. Rev. B* **69**, 075304 (2004)
 11. E. Nogales, J. Á. García, B. Méndez and J. Piqueras, *J. Appl. Phys.* **101**, 033517 (2007)
 12. C. Jin, H. Kim, K. Baek, H. W. Kim, and C. Lee, *Cryst. Res. Technol.* **45**, 199 (2010)
 13. H. W. Kim, J. W. Lee, M. A. Kebede, H. S. Kim, C. Lee, *Materials Science and Engineering B* **163** 44 (2009)
 14. S. Park, J. Jun, H. W. Kim and C. Lee, *Journal of the Korean Physical Society* **55**, 1591 (2009)
 15. G. Faglia, C. Baratto, G. Sberveglieri, M. Zha and A. Zappettini, *Appl. Phys. Lett.* **86**, 011923 (2005)
 16. C. E. Comini, C. Baratto, G. Faglia, M. Ferroni and G. Sberveglieri, *J. Phys. D: Appl. Phys.* **40** 7255 (2007)
 17. S. Lettieri, A. Setaro, C. Baratto, E. Comini, G. Faglia, G. Sberveglieri and P. Maddalena, *New J. of Phys.* **10** 043013 (2008)
 18. L. Binet and D. Gourier, *J. Phys. Chem. Solids* **59**, 1241 (1998)

the case of In_2O_3 nanostructures. Hence these nanostructures are not suitable for applications to PL based sensors.

8. Summary and future scope:

In this chapter, the summary of the results of the thesis are described briefly. The mechanism of PL in $\beta\text{-Ga}_2\text{O}_3$ and In_2O_3 nanowires and its oxygen sensitivity have been explored in this work. The variation of the PL intensity from $\beta\text{-Ga}_2\text{O}_3$ nanowires with O_2 concentration, indicates that these nanowires have possible application in an all optical (excitation and emission) based gas sensor. It is further observed that moisture exposure, especially at high temperatures, reduces the sensitivity significantly. A comparison of $\beta\text{-Ga}_2\text{O}_3$ nanostructures with the isoelectronic In_2O_3 nanowire system shows that unlike $\beta\text{-Ga}_2\text{O}_3$, where a significant component of the PL intensity arises due to electrons in conduction band recombining via self trapped excitons, the PL intensity in In_2O_3 is primarily due to deep donor-acceptor recombination and hence insensitive to changes at the surface. Various aspects of the growth of these In_2O_3 nanowires have also been explored in this thesis.

References:

1. Z.L.Wang Nanowires and Nanobelts, Kluwer Academic, New York Vol I, 3 (2003)
2. X. Fang and L. Zhang, J. Mater. Sci. Technol. 22, 1 (2006)
3. L.C. Tien, C.H. Ho, X.T. Yao, J.R. Cai Appl Phys A 102, 105 (2011)
4. N. Ueda, H. Hosono, R. Waseda and H. Kawazoe, Appl. Phys. Lett. 71, 933 (1997)
5. G. Sinha, A. Datta, S. K. Panda, P. G. Chavan, M. A. More, D. S. Joag and A. Patra, J. Phys. D: Appl. Phys. 42, 185409 (2009)
6. P. Feng, J. Y. Zhang, Q. H. Li, and T. H. Wang, Appl. Phys. Lett. 88, 153107

nanostructures, thereby modifying the acceptor defect level of β -Ga₂O₃. The results indicate that this technique can be a simple and an effective method for doping and hence tailoring the PL properties of β -Ga₂O₃ nanostructures.

7. Influence of growth parameters on the morphology and growth orientation of In₂O₃ wires:

In this chapter, we present the work carried out on the growth of In₂O₃ micro/nanostructures. We have shown that the morphology and growth direction of the In₂O₃ nanostructure can be manipulated by changing the growth temperature and the distance of the substrate from the source material. This study highlights a route to grow the In₂O₃ nanostructures with a desired growth direction ((111) or (100)) and morphology. The PL spectra of In₂O₃ nanostructures exhibit an orange-yellow emission band. The PL data is found to be strongly dependent on the morphology of the nanostructures, which in turn depends upon the growth parameters. A study of the dependence of PL intensity on the environmental oxygen partial pressure (similar to the ones carried out for β -Ga₂O₃ nanostructures) has also been carried out. No significant sensitivity to oxygen exposure was observed as the PL is only observed from deep donor to acceptor pair (DAP) transition, in which the carriers (electrons and holes) are localized. This localization makes the PL intensity insensitive to the changes on the surface of the nanostructure, thereby rendering the In₂O₃ nanostructures unsuitable for gas sensing applications using PL technique. Change in the PL intensity with the partial pressure of a particular gas can be observed only if the carriers respond to the change at the surface of the nanostructures. This can be possible if one can get PL from either a) band to band transitions, b) self trapped exciton and/or c) shallow DAP transitions etc., none of which are applicable in

In this chapter, we report the changes in the PL properties brought about by post growth annealing in different ambient conditions like, dry O₂, moisture and moist ammonia. Exposure to O₂ at high temperature permanently reduces the PL intensity typically by 10% to 20%. This is mainly due to the diffusion of oxygen in the bulk thereby reducing the oxygen vacancies. However the sensitivity of PL intensity to ambient O₂ concentration is maintained. Moisture exposure at high temperature attenuates the PL intensity by more than 70% and this attenuation is permanent in nature. Thus this reduction in the PL intensity is due to the formation of permanent defects (surface traps) on the surface of the nanostructures, which are created due to the exposure to water molecules. It is already reported in literature that reducing environment like H₂ and NH₃, enhance the PL intensity from β -Ga₂O₃ nanostructures [20, 21]. However when the β -Ga₂O₃ nanostructures were annealed at high temperatures in moist ammonia ambient, we have observed a drastic reduction in the PL intensity, which is almost identical to the case of annealing in moist environment. These results clearly suggest that the PL intensity from the nanowires is extremely sensitive to moisture and applications of β -Ga₂O₃ nanowires as sensors working in moist environments and simultaneous high temperatures would be limited.

6. Synthesis and characterization of β -Ga₂O₃ nanostructures grown on GaAs substrates:

In this chapter, we present the results related to the synthesis and characterization of β -Ga₂O₃ nanostructures made by thermal annealing of gold coated doped GaAs substrates in N₂ ambient. The effect of silicon (Si) and tellurium (Te) dopants in the GaAs substrate has been analyzed using PL from the grown nanostructures. The PL spectra indicate that the dopants present in the GaAs substrates diffuse into the β -Ga₂O₃

nanostructures have also been reported. In thermal annealing technique, growth starts from the molten gallium which is present on the GaAs substrate. Side growth of structures has been observed, which is due to diffusion of Gallium from the base to the tip. Further in these nanostructures, the UV luminescence is not as strong as compared to the blue luminescence, indicating a poor surface quality. The quality of the nanowires synthesized by the thermal evaporation technique is very sensitive to the relative position of the source and the substrate. At the optimized growth parameters, the UV luminescence is very strong. However, there is a large size distribution of the wires. Using the vapour transport method, good quality nanostructures with very strong UV luminescence were obtained. Further, a significantly improved size distribution of the nanostructures, as compared to the thermal evaporation technique, was observed. Growth by vapour transport has also been studied using dry and moist N₂ carrier gas. This study was motivated by the fact that in several metal oxide nanostructures it is reported that faster and better quality growth is obtained in moist environment [19] In the case of β -Ga₂O₃, the morphology of the nanostructures is the same for deposition carried out in moist N₂ and dry N₂ case, but there is a significant difference in the PL characteristics. In the case of moist N₂, the PL spectrum is completely dominated by the blue band. As the blue band is less sensitive to the surface states, significant reduction in the sensitivity of PL intensity to O₂ concentration is observed in these nanostructures, as compared to the case of growth in dry N₂ carrier gas. All the above results indicate that among the three techniques used, vapour transport method using dry N₂ as the carrier gas, gives the best quality β -Ga₂O₃ nanostructures from the point of O₂ sensing.

5. Effect of post growth annealing of β -Ga₂O₃ nanostructures in different environments on the photoluminescence properties:

is insensitive to ambient O₂ pressure. This behavior is repeatable and reversible. After deconvolution of PL spectra, it has been observed that the change in PL intensity from β -Ga₂O₃ nanostructures, with O₂ partial pressure for both the UV and blue band follows the Langmuir equation. Langmuir equation relates the adsorption/desorption of the gases on the surface of a material to the partial pressure of the gas. A large change in the UV luminescence intensity (8000 times) has been observed as compared to a much smaller change in the blue luminescence intensity (80 times). This large change is related to the origin of the UV luminescence. The electrons in the conduction band are mobile and have a large probability of getting trapped at the surface states created by the adsorption/desorption of O₂ molecules. However in the case of blue luminescence, both electrons and holes are trapped in the donor and acceptor sites respectively and hence are less prone to the surface trapping centers. These results provide an understanding of adsorption/desorption related mechanism in the β -Ga₂O₃ nanostructures and highlights the possibility of using β -Ga₂O₃ nanostructures for room-temperature sensing of O₂ based on its PL properties.

4. Study of different growth techniques and optimisation of the growth parameters:

In this chapter, we report the results related to the synthesis of β -Ga₂O₃ nanostructures using three different methods. The growth parameters were optimized, and the qualities of the nanostructures synthesized by these techniques are compared. The synthesis techniques adopted for the fabrication of the nanostructures were: a) thermal annealing, b) thermal evaporation and c) vapor transport. Having established that a close relationship between the presence of surface states and the PL characteristics (chapter 3), in this chapter, we present the PL results of the nanostructures synthesized by different techniques. X-ray diffraction and transmission electron microscopy results of these

the possibility of optochemical sensing of O₂ in β -Ga₂O₃ and In₂O₃ have been explored in this thesis [15-17].

The outline of the thesis is as follows:

1. Introduction:

This chapter contains details about the various physical properties of the nanomaterials and their applications in different fields. The properties of β -Ga₂O₃ and In₂O₃ have also been discussed. The motivation of the work reported in this thesis is also explained.

2. Experimental techniques and procedures:

This chapter presents an overview of the growth of nanomaterials, and their characterization techniques. The characterization techniques include X-ray diffraction (XRD), Scanning electron microscopy (SEM), Transmission electron microscopy (TEM), Photoluminescence (PL) spectroscopy and Optical absorption spectroscopy. Basic principles of all the above characterization techniques have also been discussed.

3. Dependence of PL from β -Ga₂O₃ nanostructures on Oxygen pressure:

In this chapter, the effect of O₂ gas partial pressure on the observed PL spectra from β -Ga₂O₃ nanostructures has been analyzed. PL spectra consist of mainly two components, an UV band and a blue band in the visible region. The characteristics of the UV band is similar to self-trapped excitation, which is reported in literature[18]. The blue luminescence band is from the recombination of trapped electrons in a donor states with trapped holes in acceptor states [18]. It has been observed that the total PL intensity depends strongly on the ambient O₂ gas pressure; decreasing pressure reduces the PL intensity in the β -Ga₂O₃ nanostructures. In contrast to this, PL from single crystal β -Ga₂O₃

Photoluminescence (PL), which is a non-destructive characterization method, is an important tool to characterize the optical properties of nanowires arising from both the bulk and the surface states. Effect of doping on the recombination mechanism in the nanostructures has also been investigated in details using PL spectroscopy [9-11]. The core-shell nanostructures, which have attracted attention for fabricating heterojunction nanodevices in the radial direction and passivation to protect them from contamination and oxidation, has been extensively characterized by PL spectroscopy. These results have provided an understanding of the dependence of luminescence properties on the coating material and the annealing atmosphere [12-14]. Recently, uses of PL are also reported in gas sensing activities. This approach, referred to as optochemical sensing, is based on the changes in the optical responses of a material induced by the interaction of the surface of the nanostructures with the gas molecules. As compared to sensors based on change in resistivity with gas exposure (chemoresistive devices), optochemical methods have some distinct advantages. These include operation at room temperatures and the elimination of complications that arise due to electrode fabrication [15-17].

Considering the importance of metal oxide nanostructures in several applications and the role of PL spectroscopy in understanding their optical properties, in this work two different metal oxides namely β -Ga₂O₃ and In₂O₃, which are both group III-oxide systems with similar bulk optical properties, have been investigated. It may be noted that not much work exist till date towards the understanding of the mechanism of PL from these two nanostructure systems. The primary objective of this work was thus to investigate the mechanism of PL in these nanostructures. PL results have been used to optimize the growth parameters of the nanostructures. PL has also been used to study the effect of different ambient conditions and doping in β -Ga₂O₃ nanostructures. In view of the fact that chemoresistive sensing of O₂ in β -Ga₂O₃ and In₂O₃ has already been reported [7, 8],

Synopsis

The field of nanotechnology presents an exciting research area that crosses the boundaries between physical, chemical, material, life and engineering sciences [1-2]. There are two approaches for the formation of nanomaterials: top-down and bottom-up. Conventional fabrication methods that include attrition, milling, lithography and etching methods are the typical top-down methods for making nanoscale features. Bottom-up approaches refer to the development of a material from the atomic level. There is a better chance to obtain nanostructures with less defects and more homogeneous chemical composition by the bottom-up approaches. The science of nanostructure deals with objects on a size scale of 1–100 nm. At these length scales, various interesting phenomena are observed, which are related to the exciton Bohr radius (quantization of levels), phonon mean free path (thermal properties), critical size of magnetic domains (magnetic properties), carrier diffusion length (electrical properties) etc. Among the one dimensional (1D) nanomaterials and nanostructures, metal oxides nanostructures with their wide band gap, have been useful for applications covering several areas including white light generation [3], transparent conducting electrodes [4], field emission (FE) [5], photo-detectors [6], gas sensing [7, 8] etc.. Another aspect of nanostructures is the large surface to volume ratio as compared to their bulk counterparts. For example, if we compare a thin film (1 μm thick and 5 mm radius) with nanowires (100 nm diameter and length of 1 μm) grown on the same area with a typical surface coverage of 10%, the surface to volume ratio is found to be about 10^8 times more in the case of nanowires. The surface thus plays a crucial role by providing additional carrier trapping centres, which significantly modifies the optical and electrical properties of the nanostructures. The trapping by these surface states becomes more important when the dimensions of the nanostructures are comparable to the diffusion length of the carriers.

thickness profile for the furnace. The source and substrate positions are also indicated.....	100
Figure 7.9: (a-c) shows TEM, SAED and HRTEM images of the In_2O_3 nanowire of sample C3. The nanowire is 45 nm in diameter with lattice spacing 0.49 nm which corresponds to the (200) plane, SAED pattern is indexed to [100]; (d) The SEM picture of hexagonal cross section micro wire with the (111) top surface.....	104
Figure 7.10: Schematic pictures of circular cross section wires showing with different surface/interface energies.....	105
Figure 7.11: Schematic pictures of hexagonal and square cross section wires and area calculations for the different faces. For comparison with the cylindrical wire, dimensions are taken in the form of diameter ($2r$) and length (L). In the both hexagonal and square cross section wires, length of apothem is taken as r	106
Figure 7.12: (a) Room temperature PL spectra of In_2O_3 nano/microstructure samples A1, B1 and C1; (b) samples A2, B2 and C2.....	107

List of Tables

Table I: Detail of the parameters used for growth of $\beta\text{-Ga}_2\text{O}_3$ Nanostructures.....	61
--	----

plot of $(\alpha hv)^2$ versus hv for determination of direct band gap of the β -Ga ₂ O ₃ nanostructures.....	88
Figure 6.4: Room temperature PL spectrum of β -Ga ₂ O ₃ nanostructures grown on sample A, sample B and sample C.....	89
Figure 6.5: The PL data for the samples A, B and C fitted with three Gaussian curves (dotted lines), the PL data of corresponding β -Ga ₂ O ₃ films are shown in the inset.....	90
Figure 7.1: A schematic illustration of the experimental setup for the growth of In ₂ O ₃ nano/micro structures.....	94
Figure 7.2: Details of the samples with the growth temperature (in parenthesis) and distance from the source. The source temperature (ST) is also shown in the Y-axis.....	95
Figure 7.3: The GIXRD pattern of the as-synthesized In ₂ O ₃ nano/micro structures for samples A1, B1, B2, C1 and C2.....	96
Figure 7.4: SEM images of (a) In ₂ O ₃ microwire structures and (b) In ₂ O ₃ film, grown in sample A1 and sample A2 respectively.....	97
Figure 7.5: SEM images of (a) In ₂ O ₃ microwire structures and (b) In ₂ O ₃ nanowire with thin nanosheet structures, grown in sample B1 and sample B2 respectively.....	97
Figure 7.6: The SEM images of (a) In ₂ O ₃ microwire structures, (b) In ₂ O ₃ nanowire with branched structures and (c) In ₂ O ₃ nanowires, grown in samples C1, C2 and C3 respectively.....	98
Figure 7.7: The SEM image of In ₂ O ₃ microstructures shows the bending tips, which is related to the displacement of the catalyst particle from the apex due to growth related instability, resulting in the deflection of the growth direction.....	99
Figure 7.8: Schematic of the chemical vapor deposition process and boundary layer	

respectively.....	69
Figure 4.12: Room temperature PL spectra of β -Ga ₂ O ₃ nanostructures in (a) sample 3A and (b) sample 3B.....	70
Figure 4.13: (a-b) Room temperature PL spectrum of β -Ga ₂ O ₃ nanostructure sample 3A and 3B at different O ₂ pressure conditions.....	73
Figure 5.1: A schematic illustration of experimental setup for annealing of β -Ga ₂ O ₃ nanostructures.....	77
Figure 5.2: The GIXRD pattern of as synthesized β -Ga ₂ O ₃ nanostructures, in sample A, sample B, sample C and sample D.....	78
Figure 5.3: The SEM images of β -Ga ₂ O ₃ nanostructures grown on sample A. There is an extensive growth of nanowires which have diameter of around 40-100 nm and length up to a few hundred microns.....	78
Figure 5.4: Room temperature PL spectrum of β -Ga ₂ O ₃ nanostructure sample A, B, C and D which shows that PL intensity is sensitive to the annealing in different environments.....	79
Figure 5.5: Integrated intensity plot of peaks 360 nm and 410 nm for sample A, B, C and D. Inset shows the fitting of two Gaussian peak for the PL data of sample A.....	80
Figure 5.6: (a-c) Room temperature PL spectrum of β -Ga ₂ O ₃ nanostructure sample A, B and C at different O ₂ pressure conditions.....	81
Figure 6.1: The GIXRD pattern of as synthesized β -Ga ₂ O ₃ nanostructures grown on sample A, sample B and sample C.....	86
Figure 6.2: The SEM images of β -Ga ₂ O ₃ nanostructures grown on (a) sample A, (b) sample B, (c) sample C.....	87
Figure 6.3: Optical absorption spectrum of β -Ga ₂ O ₃ nanostructures. The inset shows a	

Figure 4.4: (a-f) The SEM images of β -Ga₂O₃ nanostructures grown on sample 2A, 2B and 2C. In the spot-1 region thick structures (plates, rods etc. in the micron range) are seen which was just above the source material whereas nanostructures are observed away from the source region in the spot-2 region..... 63

Figure 4.5: (a-b) shows the as grown nanostructures on the samples 3A and 3B respectively. An extensive growth of β - Ga₂O₃ nanowires, which have diameter of around 40-100 nm and length up to a few hundred microns, is observed in both the samples..... 64

Figure 4.6: TEM and HRTEM images of β -Ga₂O₃ nanowire of sample 1; (a) TEM image of an individual nanowire, (b) the corresponding SAED pattern along [100] zone axis, (c) HRTEM image of the (001) planes with interlayer spacing of 0.56 nm..... 65

Figure 4.7: TEM and HRTEM images of β -Ga₂O₃ nanowires of sample 2A. Nanowire is 60 nm in diameter with lattice spacing 0.368 nm which correspond to (201) lattice planes..... 65

Figure 4.8: TEM and HRTEM images of the β -Ga₂O₃ nanowires grown in sample 3B. HRTEM have been done at various places of the nanowires (on the nanowire and side grown structure). Same lattice spacing 0.282 nm, which correspond to the (-202) lattice planes, is observed. SAED pattern is indexed along the [202] zone axis..... 66

Figure 4.9: Room temperature PL spectra of (a) β -Ga₂O₃ nanostructures in sample1 and (b) β -Ga₂O₃ thin film grown on GaAs substrate..... 67

Figure 4.10: Room temperature PL spectra of β -Ga₂O₃ nanostructures in the (a) sample 2A (for spot-1 and spot-2), (b) sample 2B (for spot-1 and spot-2) and (c) sample 2C (for spot-1 and spot-2)..... 68

Figure. 4.11: Comparative room temperature PL spectra of sample 2A, sample 2B and sample 2C for spot-1 and spot-2 are shown in figure (a) and (b)

sample fitted with two Gaussian peaks, using the excitation energy of 4.66 eV.....	47
Figure 3.5: Room temperature PL spectra of β -Ga ₂ O ₃ (a) nanostructure and (b) bulk sample, at different oxygen pressure conditions using the excitation energy of 4.66 eV.....	48
Figure 3.6: (a) Plot of O ₂ pressure versus integrated intensity for the 360 nm (3.44 eV) peak in the ascending and descending pressure conditions, (b) the same for the 400 nm (3.10 eV) peak.....	49
Figure 3.7: (a) The temperature dependent PL spectra of sample 3A, (b) the plot of UV luminescence integrated intensity as a function of temperature in which an enhancement of the UV luminescence at 250 K is observed, similarly (c) shows the temperature dependent PL spectra of bulk gallium oxide single crystal and (d) the plot of UV luminescence integrated intensity as a function of temperature in which an enhancement of the UV luminescence at 160 K is observed.....	50
Figure 3.8: Model for the UV-visible luminescence mechanism in β -Ga ₂ O ₃ nanostructure samples in which defect created on the nanowire surface are shown.....	52
Figure 3.9: (a, b) Langmuir equation fitting for 360 nm (3.44 eV) and 400 nm (3.10 eV) PL bands.....	55
Figure 3.10: Room temperature PL spectrum of β -Ga ₂ O ₃ nanostructure sample with 3.81 eV He-Cd laser, at different oxygen pressure conditions.....	56
Figure 4.1: Schematic of the growth process for (a) sample 1, (b) samples 2A, 2B, 2C and (c) samples 3A, 3B and 3C.....	60
Figure 4.2: The GIXRD pattern of as synthesized β -Ga ₂ O ₃ nanostructures for sample 1, sample 2B, sample 3A and sample 3B.....	61
Figure 4.3: SEM image of β -Ga ₂ O ₃ nanostructures grown on sample 1.....	62

List of Figures

Figure 2.1: A schematic of a thermal furnace synthesis system that is used in vapor phase growth methods; a) thermal annealing method, b) thermal evaporation method and c) vapor transport method.....	29
Figure 2.2: Vapor-liquid-solid mechanism illustrated for the metal oxide nanowires.....	31
Figure 2.3: (a) Schematic diagram showing the components of a scanning microscope (b) shows the signals which are observed as a result of incident beam and sample interaction and are used in the SEM.....	33
Figure 2.4: (a) Schematic diagram showing the components of a TEM microscope in imaging and diffraction modes (b) shows the signal which are observed as a result of incident beam and sample interaction and are used in the TEM.....	34
Figure 2.5: Schematic of X-ray diffraction from the lattice planes of single crystal.....	36
Figure 2.6: Schematic of ultraviolet-visible spectroscopy experimental setup.....	37
Figure 2.7: Schematic of the photoluminescence experimental setup.....	41
Figure 3.1: a schematic illustration of experimental setup for the growth of β -Ga ₂ O ₃ nanostructures.....	44
Figure 3.2: (a) GIXRD pattern of as synthesized β -Ga ₂ O ₃ nanostructures and (b) their SEM image	45
Figure 3.3: TEM, SAED and HRTEM images of the β -Ga ₂ O ₃ nanowire which contain gold on the tip, nanowire is 40 nm in diameter with lattice spacing 0.234 nm.....	46
Figure 3.4: Room temperature PL spectra of β -Ga ₂ O ₃ (a) nanostructure and (b) bulk	

indicate that the impurities (doping) present in GaAs substrates diffuse into the β -Ga₂O₃ nanostructures as dopants, thereby modifying the defect levels of β -Ga₂O₃. Modification in the defect levels shifts the PL emission band of β -Ga₂O₃ nanostructures. The tuning of optical properties of β -Ga₂O₃ nanostructures indicates possible applications of these nanostructures in optoelectronic nano-devices.

In **chapter 7**, we discuss in detail the growth mechanism of In₂O₃ micro/nanowires grown by vapor transport method. It has been found that the growth of In₂O₃ micro/wires, in terms of morphology and growth directions, can be manipulated by controlling the growth parameters like growth temperatures and incoming reactant vapor concentrations. This study highlights a route to grow the In₂O₃ micro/nanostructures with a desired growth direction ($\langle 111 \rangle$ or $\langle 100 \rangle$) and morphology. Orange-yellow emission bands have been observed in the PL spectra of In₂O₃ micro/nanostructures. The strong dependence of PL data on the morphology of the grown wire structures has been found which in turns depends upon the growth parameters. No significant PL sensitivity to oxygen exposure has been observed in the PL measurements carried out at different oxygen partial pressure.

In **chapter 8**, we conclude the thesis and briefly discuss the possible future work.

using above mentioned three methods, are presented in **chapter 4**. It has been observed that PL spectra of β -Ga₂O₃ nanostructures consist of two luminescence bands centered at the UV and visible regions. The intensity of UV luminescence band is found to be strongly dependent on the surface quality of the nanostructures as compared to the visible luminescence band intensity. The reason for this has been explained using our proposed band model. By comparing the relative intensity of UV to visible bands, quality of the nanostructures in term of surface defects has been evaluated. The results suggest that vapor transport method is the better technique among the three methods. The effect of surface defects, formed during the growth, on the PL intensity response to O₂ concentration has also been analyzed. It has been concluded that the defects produced on the surface of the nanostructure during growth processing reduce the sensitivity of PL intensity to O₂ concentration.

In **chapter 5**, we summarize our results of effects of different ambient at high temperatures on the optical properties of the β -Ga₂O₃ nanostructures. This was done by annealing the as grown β -Ga₂O₃ nanostructures in the different ambient (O₂, moisture and moist ammonia) at high temperatures ($\sim 800^\circ\text{C}$ for half an hour). It has been observed that annealing in different ambient changes the defect structures inside and at the surface of nanostructures. By comparing the UV and visible luminescence band intensity, it has been confirmed that moisture at high temperature produces permanent surface defects. It has also been observed that at high temperatures, adsorption of water dominates over the effect of other gases. These permanent surface defects, produced due to annealing, leave less effective surface area for the oxygen adsorption/desorption and hence the nanostructures show reduction in the PL intensity variation with the oxygen pressure.

We discuss the effect of doping, present in the GaAs substrate, on growth of β -Ga₂O₃ nanostructures using thermal annealing method in **chapter 6**. The PL spectra

1.5 Organization of the thesis:

In **chapter 2**, we present an overview of the experimental techniques, including the vapor based method, used for the syntheses of nanostructures and their characterization techniques. The characterization techniques include X-ray diffraction (XRD), Scanning electron microscopy (SEM), Transmission electron microscopy (TEM), Photoluminescence (PL) spectroscopy and Optical absorption spectroscopy. Basic principle of the all the above characterization techniques is also discussed.

The results of detailed photoluminescence studies for β -Ga₂O₃ nanostructures have been included in **chapter 3**. It has been observed that the PL intensity depends on the ambient oxygen gas pressure; decreasing pressure reduces the PL intensity. This is contrary to the observation in single crystals of β -Ga₂O₃, which are insensitive to ambient oxygen pressure. The variation of PL intensity with O₂ ambient pressure is repeatable and reversible. The luminescence mechanism with the inclusion of surface states to explain this behavior has been proposed. The change in the PL intensity with oxygen pressure follows the Langmuir equation, which relates the adsorption/desorption of the gases on the surface of the nanostructures to the partial pressure of the gas. PL measurements with below band gap excitation have also been carried out to find the tentative location of the surface defects. These results provide an understanding of adsorption/desorption related mechanism for β -Ga₂O₃ nanostructures and this will be important for the application in the room-temperature optical luminescence based sensing of oxygen.

β -Ga₂O₃ nanostructures have been grown by three different growth methods (thermal annealing, thermal evaporation and vapor transport methods) to find out the best growth method for the good quality β -Ga₂O₃ nanostructures. Our results of the investigation based on the PL spectroscopy, on the quality of the nanostructures grown

1.4 Motivation of the thesis

From the above discussion, it is clearly evident that among metal oxide based 1D nanostructures, β -Ga₂O₃ and In₂O₃ nanostructures are very important and widely used in almost every field of photonics and optoelectronic devices. Nanostructures have large surface to volume ratio. Hence, it is important to study and understand the parameters which influence the surface along with other parameters. Surface related effects greatly influence the properties of these nanostructures. To obtain the good quality nanostructures for the application in the photonic field, detail studies of growth optimization and knowledge of recombination mechanism are necessary. Growth optimization includes investigation of different growth techniques and optimization of their growth parameters. To probe the details of the recombination mechanism, PL as a nondestructive characterization technique serves as an indispensable tool. It can characterize both bulk and surface related properties of the nanostructures. Considering the importance of β -Ga₂O₃ and In₂O₃ material systems, in this thesis different growth techniques have been used to grow good quality nanostructures of these materials. The recombination mechanisms in these nanostructures have been investigated using PL spectroscopy. We wish to mention here that there is not much study available for these two nanostructure systems in literature. PL spectroscopy has also been used to optimize the growth parameters of these nanostructures. The effect of doping in the nanostructures and post growth annealing in different ambient have also been investigated using PL spectroscopy. A possibility of sensing by all optical means has been explored in these nanostructures similar to reported for other metal oxide (ZnO and SnO₂) nanostructures. This work aims at providing an insight into the growth optimization and PL mechanism in these nanostructures with special emphasis to optical and sensing applications.

300°C is comparable with that from thin film sensors at 600-1000°C) [49]. Operation of sensing devices above room temperature involve the need to incorporate heating and temperature control units, thereby increasing the complexity and power consumption [47-49].

Thus realizing the importance of 1D nanostructures over thin film, for the use in gas sensors (eg. low power consumption, simple system configuration, reduced explosion hazards, and longer device lifetime); there have been several reports on the development of gas sensors using metal oxide nanostructures [50-54]. Gallium oxide and indium oxide nanostructures among these materials are also used in the field of gas sensing. P. Feng et. al. have reported fast oxygen response in individual β -Ga₂O₃ nanowire by ultraviolet illumination [55]. S. Bianchi et. al. have reported indium oxide nanowires for CO and NO₂ or ethanol vapors sensing in the single and multiple wire configurations [56]. Zhang and co-workers have worked extensively on In₂O₃ nanowire-based sensors. They have demonstrated the operation of a single In₂O₃ nanowire as a chemical sensor for NO₂ and NH₃ at room temperature [57]. Zhou and co-workers [58] also demonstrated detection of NO₂ down to ppb level using transistors based on both single and multiple In₂O₃ nanowires operating at room temperature.

Similarly, sensing via optical luminescence measurements have also emerged as an alternative route for gas sensing. This is important due to the elimination of all the complications that arise due to electrode fabrication and contact making. In addition, the sensing response time and recovery time are also comparable with the response times of electrical based chemical sensors. The optical luminescence properties in the nanostructures are significantly affected by the surface because of high surface to volume ratio. The most commonly used sensors based on all optical means are reported to be of ZnO and SnO₂ nanostructures [59-60].

developed. Recently, Indium oxide has also emerged as an important material for such type of applications [40, 41]. Optical whispering gallery resonators from In_2O_3 nanowires with hexagonal cross section have been fabricated by using a simple in-situ thermal oxidation method [42].

High contrast between the refractive indices of the wires, (typically 1.75–4), and the surroundings make them very good materials for optical waveguides [43-44]. $\beta\text{-Ga}_2\text{O}_3$ has a refractive index between 1.85–1.91, which makes this material suitable for light guiding and for optical antireflection coatings [43-44]. Undoped as well as Cr and Er doped Ga_2O_3 nano- and microwires grown by thermal treatments at 1500°C under argon flow, show wave guiding behavior for the dopant ion luminescence light. [45]

1.3.5 Sensor devices

The nanotubes, nanorods, nanobelts, and nanowires based sensors represent a powerful detection platform for a broad range of applications, including biological sensors, electrochemical sensors, gas sensors, optical sensors, pH sensors, orientation sensors, etc. The sensing devices include individual nanostructured sensors, multi-nanostructured sensors and MOSFET-based sensors. These nano sensor devices have a number of key features, including high sensitivity, selectivity, fast response and recovery, and potential for integration into addressable arrays, which sets them apart from other technologies for sensors available today [46].

They have superior sensitivity than their thin film counterparts. In order to achieve maximum sensitivity, thin film gas sensors are often operated at elevated temperature [47-49]. In addition to the high sensitivity of the 1D oxide nanostructures based gas sensors, their operating temperatures are also much lower than their thin film counterparts (eg: the efficiency of O_2 sensing by $\beta\text{-Ga}_2\text{O}_3$ nanostructure through electrical means at

optoelectronic circuits [23-24]. Active 1D nanostructure photodetector elements can be configured either as resistors, whose conduction is altered by a charge-transfer process or as field-effect transistors (FET), whose properties can be controlled by applying appropriate potentials onto the gates. Photo-response of several metal oxide 1D nanostructures of materials like ZnO, SnO₂, Cu₂O, Ga₂O₃, Fe₂O₃, In₂O₃, CdO and CeO₂ have been demonstrated. Individual β -Ga₂O₃ and In₂O₃ nanowires as a solar-blind photo-detector have been demonstrated with detailed electronic transport and ultraviolet photo detection properties [25-28].

1.3.4 Optical resonator devices

As a result of miniaturization in the field of electronics and photonics, very small optical resonators have gained importance [29]. Nanowires with flat ends (rectangular or hexagonal) can also be exploited as optical resonance cavities to generate coherent light on the nanoscale. The high crystalline quality of the nanowires along with their flat surfaces makes a perfect combination for applications to optical resonators. The Fabry-Perot (FP) modulations represent the reflections between wire flat ends whereas whispering gallery modes (WGMs) represent the total internal reflections in microstructures with regular polyhedral cross-sections. Inside a whispering gallery resonator, the light wave circulates around, due to multiple total internal reflections at the resonator's boundary. This effect typically leads to high Q factors and low laser threshold [30]. The electromagnetic field and the photon density of states can be precisely controlled in a predefined manner which is essential for various purposes including lasers [31], optical waveguides [32], tunable filters [33], and optical sensors [34]. Waveguide resonators with different geometries, such as rings [35], microspheres [36], cylinders [37], nanonails [38], and nanowires with hexagonal cross section [39], have been

applied for the heterojunction based ZnO LED including p-GaN/n-ZnO, p-polymer/n-ZnO and p-Si-Ge/n-ZnO [9-12]. Apart from this, gallium oxide and indium oxide with band gap of about ~ 5 eV and 3.6 eV respectively also provide the possibility of light emission in the ultraviolet region. Due to wide band gap they are already used as the host material for multicolor-emitting phosphors [13-14] and as a broadband white light emitter [15, 16].

1.3.2 Field emission devices

Field emission (FE) is an electron escape process from the surface of material under the presence of sufficiently large electric field. The oriented nanostructures with a high packing density have the advantages of faster device turn-on time, compactness and low voltage operation, as compared with conventional bulk material based technologies [17-18]. A lot of research has been conducted on the FE behaviour of carbon nanotubes (CNTs) and it is observed that an array of densely packed CNTs greatly reduce the field-enhancement factor at the CNT tip to a level not much different from a flat metal plate [19-20]. Alternatively, metal oxide semiconducting nanowires are very good and efficient FE sources, because of their resistance to mechanical stresses induced by the intense applied electric field and ion bombardment [21]. Field-emission characteristics of indium oxide pyramids have also been reported. The field-emission current density of the nano-pyramids is comparable to that of carbon nanotubes and can guarantee sufficient luminescence brightness in a flat panel display [22].

1.3.3 Photo detector devices

Photo detectors are critical for applications as binary switches in imaging techniques and light-wave communications, as well as in future memory storage and

Bottom up: In this approach, methods have been developed for the atom-by-atom, molecule-by-molecule, and/or cluster-by-cluster growth of the nanostructures. The bottom-up approach promise a better chance to obtain nanostructures with much less defects, and more homogeneous chemical composition. Thus, this approach has the ability to go far beyond the limits and functionality of top-down based technology.

1.3 Metal oxide nanostructures and their applications

Among inorganic semiconductor nanomaterials, 1D metal oxide nanostructures are the focus of current research efforts in nanotechnology since they are the most commonly available materials. Their specific shapes, composition, chemical, and physical properties have been used for several applications [8]. Due to their wide band gap, metal oxide nanowires have attracted a lot of attention for making transparent conducting electrodes and UV photo detectors. Furthermore, the strong influence of surface chemistry on the conductive and photoconductive properties of metal oxide nanowires, make them especially suitable for gas and chemical sensing. Some of the applications of metal oxide nanostructures are elaborated in the following sub-section.

1.3.1 Light emitting devices

1D nanostructures exhibit interesting electronic and optical properties intrinsically associated with their low dimensionality. A branch of these applications is light emitting diode (LED) devices. Currently available commercial LEDs based on III-V including III-Nitride have revolutionized our lives. Among metal oxide based nanostructure LEDs, ZnO based devices have attracted the maximum attention. This is primarily due to the large exciton binding energy ~ 60 meV and ease of fabrication. Since the fabrication of high quality p-ZnO is still difficult, various combination of p-type materials have been

the material, resulting in quantized energy states. This quantization leads to different properties of the 1D nanostructure which are different with respect to their bulk counterparts like electrical transport, magnetic properties, optical properties etc. Surface related effects arise because atoms at the surface of a crystalline solid experience a different environment as compared to those inside the bulk. In bulk materials, the proportion of surface atoms to bulk atoms is negligible, and processes that take place at the surface are usually of very little consequence to the behavior of the material as a whole. As, the surface-to-volume ratio in 1D nanostructures increase significantly, the surface effects cannot be ignored at nanoscale. Their large surface-to-volume ratio allows for distinct structural and chemical behavior as well as greater chemical reactivity [4].

1.2 Nanostructure fabrication approaches

There are two distinct approaches for creating nanostructures: top-down and bottom-up.

Top down: In this approach, conventional fabrication methods, like attrition, milling or the combination of thin film growth, lithography, and etching methods, are used for obtaining nano sized features. This approach is very successful in several systems, the most important being microelectronics. The main drawback of the top-down approach is the imperfections at the surface structure caused by the processing steps like lithography, etching, ion milling etc. These imperfections have a significant impact on the properties of nanostructures. Further, the costs of the photolithographic techniques increase significantly with decreasing size. Based on these limitations, 1D nanostructures, grown by bottom-up approach, represent attractive building blocks for hierarchical assembly of functional nanoscale devices.

Chapter 1

Introduction

The field of nanotechnology represents an exciting and rapidly expanding research area that crosses the boundaries between the physical, chemical, materials, life and engineering sciences. In the area of nanometer scale research, much excitement has arisen from the recognition that new phenomena and unprecedented integration density are possible with nanometer scale structures [1-2]. There are a large number of new opportunities that could be realized by down-sizing the currently existing structures into the regime of nanometer scale. Nanowire photonic circuitry constructed from one-dimensional building blocks offers numerous opportunities for the development of next-generation optical information processors and spectroscopy [3-4].

1.1 One dimensional nanostructures

The term nano, derived from the Greek word nanos which means dwarf, designates a billionth fraction of a meter. Thus the science of nanostructures deals with objects on a size scale of 1–100 nm. For the characterization of this research field the notations “Nanostructured Science” or “Nanotechnology” were coined by K.E. Drexler [5-7]. One dimensional (1D) nanostructures have received increasing interest as a result of their unusual physical properties and fascinating applications compared with their bulk counterparts. The properties of 1D nanostructure can be roughly separated into two primary categories: quantum confinement effects and surface-related effects. Quantum effects occur when the radial dimension of the 1D nanowire is of the same order as the de-Broglie wavelength of carrier in the material. This limits the motion of an electron in

higher than 700 nm, was recorded with the 600 lines/mm grating blazed at 1000 nm. A Hamamatsu make (model no. R928) photomultiplier tube (PMT) was used as a photon detector.

The actual sample response is obtained by removing the instrument response from the measured luminescence spectra. The equation used for the actual sample response was: $S(\lambda) = (I_{\text{sample}}/I_{\text{lamp}})*L(\lambda)$. I_{sample} is the intensity measured from the sample which is equal to $= S(\lambda)*O(\lambda)*M(\lambda)*D(\lambda)$; where $S(\lambda)$ is sample response, $O(\lambda)$ is optics response, $M(\lambda)$ is monochromator response and $D(\lambda)$ is detector response. Similarly, I_{lamp} is the intensity measured from a lamp of known response which is equal to $= L(\lambda)*O(\lambda)*M(\lambda)*D(\lambda)$; where $L(\lambda)$ is the spectral response of the lamp.

the nanostructures. Thus quantization effects due to carrier confinement are not observed in such systems. However as the dimensions are in the nanometer range, the surface to volume ratio is very large compare to the bulk. Dimensions of the nanostructures are also less than the carriers (electron and hole) diffusion lengths. Therefore, the carriers easily respond to the changes at the surface and the corresponding recombination rates change. These changes along with the recombination mechanism can be probed effectively by PL measurements.

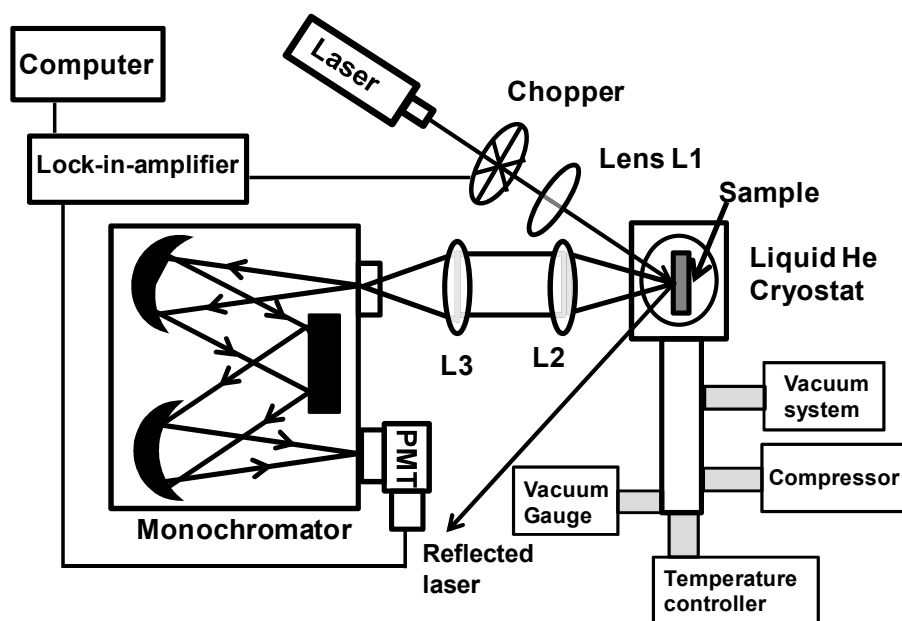


Figure 2.7 Schematic of the photoluminescence experimental setup

In the present work, luminescence properties of the β -Ga₂O₃ and In₂O₃ nanostructures are investigated using PL spectroscopy. The experimental setup diagram of the PL experiment is shown in fig.2.7 Nd-YAG fourth harmonic laser (make: Crylas) with excitation wavelength of 266 nm and power of 10 mW was used for most of our samples. For temperature dependent PL study, the closed circuit liquid Helium cryostat (Compressor model no.: ARS-2HW; cold head model no.: DE-202AL) was used. Cooling temperature was controlled by the thermo controller (Model no.: Cryocon 332B). For the PL measurements, Sciencetech ¼ meter monochromator with 1200 lines/mm grating blazed at 500 nm was used to record the PL spectra from 300 nm to 700nm. The spectra

R_{Auger} denotes Auger recombination rate which is a three particle interaction where a conduction band electron and a valence band hole recombine, with the excess energy being transferred to a third free electron or hole.

$$R_{Auger} = C_n n^2 p + C_p n p^2 \quad (5)$$

$C_n n^2 p$ denotes *eeh* process denotes where the excess energy is transferred to another electron and $C_p n^2 p$ denotes *ehh* process denotes where the excess energy is transferred to another hole. C_n and C_p are Auger coefficients.

$R_{surface}$ denotes recombination rate of recombination via surface states. The surfaces or interfaces of a crystal represent a severe discontinuity in its crystalline structure that leaves a large numbers of dangling bonds. This leads to a huge number of defect levels within the bandgap near the crystal surface. This recombination is a special kind of SRH type recombination in which recombination events are taken as per unit surface area, rather than per unit volume.

$$R_{surface} = \frac{n_s p_s - n_i^2}{\frac{(n_s + n_1)}{S_{p0}} + \frac{(p_s + p_1)}{S_{n0}}} \quad (6)$$

$$\text{where } S_{n0} = \sigma_n v_{th} N_{ts} ; S_{p0} = \sigma_p v_{th} N_{ts}$$

where n_s and p_s are the concentrations of electrons and holes at the surface, and N_{ts} is the density of surface states per unit area.

In the bulk material, bulk recombination (R_{bulk}) dominates over the surface recombination because the contribution of the surface is very small in the bulk crystals. In the nanostructures, due to large surface to volume ratio, surface recombination plays a crucial role in defining the properties of these nanostructure materials. Most of the reported metal oxide nanostructures including the nanostructure studied in this thesis has the dimensions larger than their de-broglie wavelength which define the quantization in

$$\begin{aligned}
R_{rad} &= B(np - n_i^2) \\
&= B(n_0 + p_0)\Delta n + B\Delta n^2
\end{aligned} \tag{3}$$

where B, the coefficient of radiative recombination, is the quantum-mechanical probability of a radiative transition. It depends on the band structure of the material.

The non-equilibrium concentration (arises due to external excitation) are taken as $n = n_0 + \Delta n$ and $p = p_0 + \Delta p$ where $n_0 p_0 = n_i^2$ is the thermal equilibrium carrier concentrations. As the number of electrons and holes produced by external excitation is same, $\Delta n = \Delta p$.

R_{SRH} , is recombination rate for the Shockley-Read-Hall (SRH) Recombination [71-72]. This is related to the recombination through a two-step process where a free electron from the conduction band first relaxes to the defect level and then annihilates with a hole in the valence band. These defects, in a crystal, arise due to impurities or crystallographic imperfections such as dislocations. These defects, also known as traps, produce discrete energy levels within the bandgap.

$$\begin{aligned}
R_{SRH} &= \frac{np - n_i^2}{\tau_{p0}(n + n_1) + \tau_{n0}(p + p_1)} \tag{4} \\
\text{where } \tau_{n0} &= \frac{1}{\sigma_n v_{th} N_t}; \tau_{p0} = \frac{1}{\sigma_p v_{th} N_t}
\end{aligned}$$

$$\text{and statical factors } n_1 \equiv N_C \exp\left(\frac{E_t - E_C}{k_B T}\right);$$

$$p_1 \equiv N_V \exp\left(\frac{E_C - E_G - E_t}{k_B T}\right)$$

τ_{n0} and τ_{p0} are electron and hole lifetimes. N_t is density of recombination defects. σ_n and σ_p are capture cross-sections of the defects. N_C and N_V are effective density of states at the conduction and valence band edges. E_C and E_G are the conduction band and bandgap energies. E_t is the energy level of the defect.

contains the solvent in which the sample is dissolved and this is referred to as the reference. For each wavelength, the intensity of light passing through both reference cell (I_0) and the sample cell (I) is measured. The absorbance (A) of the sample is related to I and I_0 according to the equation: $A = -\log(I/I_0)$. The absorption is plotted as a function of the wavelength in an absorption spectrum. There are various possible transitions like band to band, exciton, between subbands, between impurities and bands, transition by free carriers within a band etc. that can be probed by this method. In this work, CECIL 7500 Double Beam UV/Visible Spectrophotometer with wavelength range 190-1100 nm was used.

2.3.2.2 Photoluminescence spectroscopy

Once the electron-hole pairs are generated by absorption of photon in the material, they are exposed to several recombination mechanisms. These processes occur in parallel and the recombination rate is the sum of those for individual processes. The radiative recombination process gives rise to PL. Total recombination rate for the different recombination mechanisms is expressed as [70]

$$\begin{aligned} R_{Total} &= (R_{rad} + R_{SRH} + R_{Auger}) + R_{surface} \\ &= R_{bulk} + R_{surface} \end{aligned} \quad (2)$$

The four main terms, R_{rad} , R_{SRH} , R_{Auger} and $R_{surface}$, are explained in detail below.

R_{rad} is recombination rate for the radiative recombination which is simply the direct annihilation of an electron-hole pair. It is the inverse process to optical absorption, the excess energy being released mainly as a photon with energy close to that of the bandgap. It depends on the concentration of electron in the upper level and holes in the lower level.

strength. Bruckers D8 GIXRD system with Cu K_{α} radiation which have wavelength $K_{\alpha} = 0.15405$ nm is used in this work.

2.3.2 Optical characterization

In this section, two main optical techniques used in the work, namely absorption and photoluminescence is discussed in detail.

2.3.2.1 Absorption spectroscopy

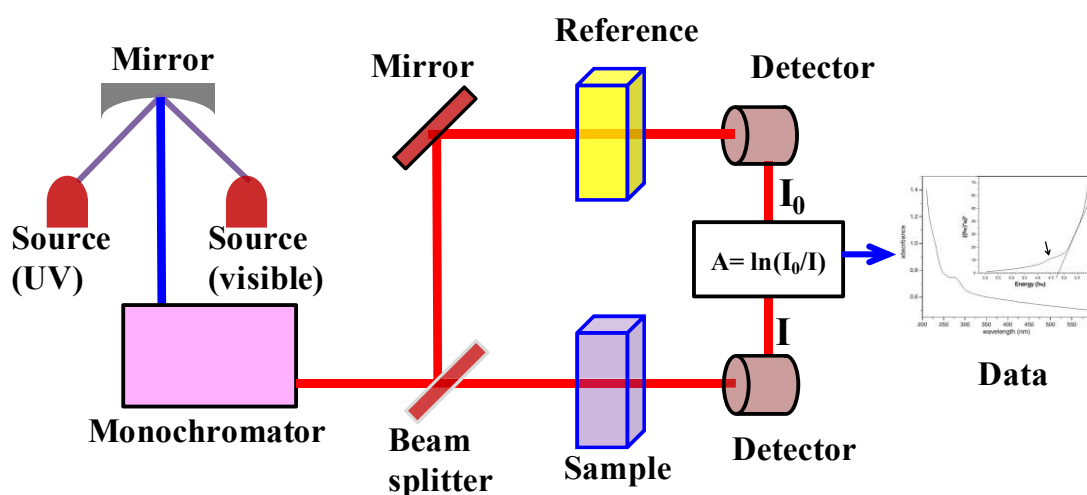


Figure 2.6 Schematic of ultraviolet-visible spectroscopy experimental setup

In this work Ultraviolet-visible spectroscopy (UV-Vis) is used to investigate the absorption processes. Ultraviolet-visible spectroscopy (UV-Vis) refers to absorption spectroscopy in the ultraviolet-visible spectral region. UV region ranges from 190 to 400 nm and visible region ranges from 400 to 800 nm. A schematic diagram of a UV-visible spectrometer is shown in fig. 2.6. The light source (a combination of tungsten/halogen and deuterium lamps) provides the visible and near ultraviolet radiation covering the 200 – 800 nm. The output from the light source is monochromatized to splits the incoming light into its component colors of different wavelengths. For liquids, the sample is placed in an optically flat, transparent container called a cuvette. The reference cell or cuvette

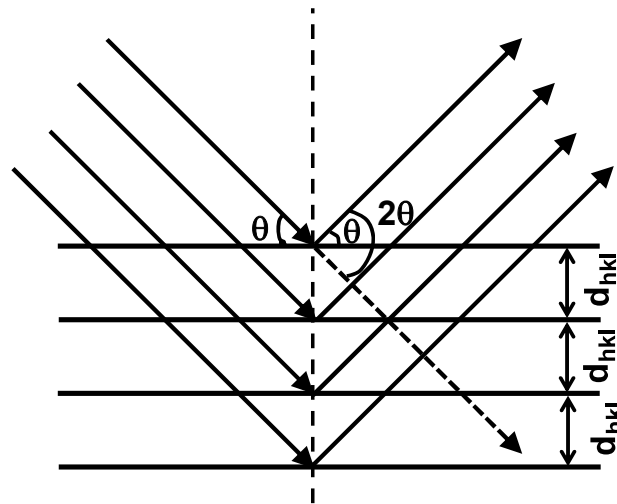


Figure 2.5 Schematic of X-ray diffraction from the lattice planes of single crystal.

Bragg's law calculates the angle where constructive interference from X-rays scattered by parallel planes of atoms will produce a diffraction peak.

$$\lambda = 2d_{hkl} \sin(\theta) \quad (1)$$

where λ is X-ray wavelength and d_{hkl} is the distance between parallel planes of atoms in the family (hkl) . Consequently, a family of planes produces a diffraction peak only at a specific angle 2θ . X-rays have large penetration depth inside any matter. In our case, it is difficult to analyze the nanostructures grown on the silicon substrate due to their small diffracting volumes, which result in low diffracted intensities compared to the substrate and background. Thereby, grazing incidence x-ray diffraction (GIXRD) is used to overcome this restriction. In this geometry, the stationary incident beam makes a very small angle with the sample surface (typically 1° to 3°), which increases the path length of the X-ray beam through the nanostructure's film grown on the silicon substrate. This increases the diffracted intensity of the nanostructures with simultaneous reduction in the diffracted intensity from the substrate. This results in a significant increase in the signal-to-background ratio. Apart from this, due to increase in the path length, the diffracting volume also increases. Increase in the diffracting volume further increases the signal

distribution of electron intensity is then displayed on the screen (coated with a phosphor or scintillator material) to get the results.

Conventional TEM uses only the transmitted beams or some of the forward scattered beams to create an image. HRTEM uses the phase contrast mechanism, in which the image is formed from the interference between waves of different phases. By tilting the crystal such that the incident beam is parallel to a zone axis in the crystal, many strong diffracted beams can be produced. Selecting several beams allows a structure image (HRTEM image) to be formed. The many lattice fringes intersect and give a pattern of dark (or bright) spots corresponding to the atom columns. Good HRTEM image can only be obtained from thin specimens, since inelastic scattering degrades the image quality. In this work, Philips CM200 TEM system is used. This TEM is equipped with a LaB₆ and tungsten sources and is maintained at a base pressure of 10⁻⁹ mbar. The acceleration voltage is 200 keV and the line resolution is 0.14 nm at 200 keV and point resolution is 0.24 nm at 200 keV.

2.3.1.3 X-ray diffraction

X-ray diffraction (XRD) is one of the most important non-destructive tools to analyze all kinds of matter e.g fluids, powders and crystals. Each crystalline solid has its unique characteristic X-ray powder pattern which may be used as a “fingerprint” for its identification. Diffraction is a scattering phenomenon in which a large number of atoms cooperate. Since the atoms are arranged periodically on a lattice, the rays scattered by them have definite phase relationship; these phase relationship are such that destructive interference occurs in most directions of scattering, but in a few directions constructive interference takes place and diffracted beams are formed. The position of the diffraction peaks are determined by the distance between parallel planes of atoms.

2.3.1.2 Transmission electron microscopy

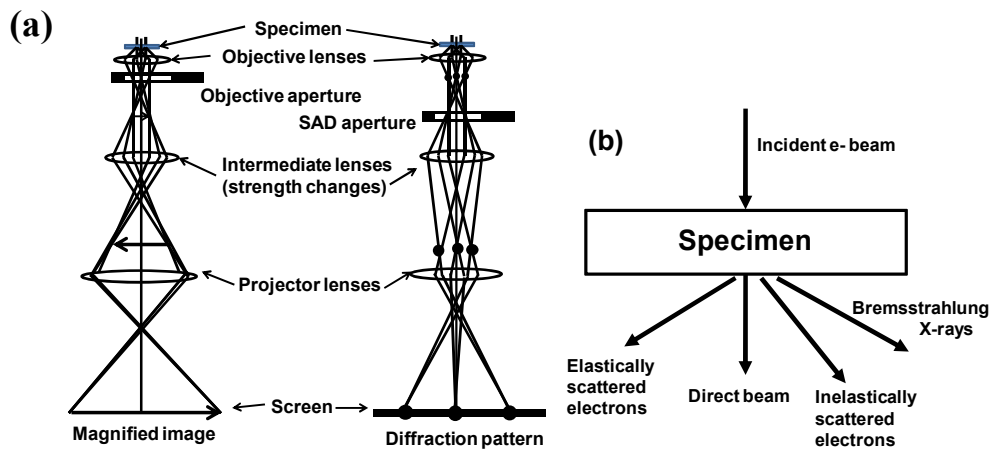


Figure 2.4 (a) Schematic diagram showing the components of a TEM microscope in imaging and diffraction modes (b) shows the signal which are observed as a result of incident beam and sample interaction and are used in the TEM

TEM and high resolution transmission electron microscopy (HR TEM) are powerful imaging tools to study nanowires at the atomic scale. They usually provide more detailed geometrical features than are seen in SEM images. TEM studies also yield information regarding the crystal structure, crystal quality, grain size, and crystal orientation of the nanowires. When operating in the diffraction mode, selected area electron diffraction (SAED) patterns can be made to determine the crystal structure of nanowires. The high resolution of the TEM also allows for the investigation of the surface structure of the nanowires. In many cases the nanowires are sheathed with a native oxide layer, or an amorphous oxide layer that forms during the growth process.

Unlike SEM, TEM uses a relatively higher voltage (40 keV to 400 keV) electron beam to create an image. The electron beam with high energy is transmitted through the sample and this transmitted electron beam carries information about the sample structure that is magnified by the objective lens system. As they pass through the sample, they get scattered by the sample in several ways. The spatial (imaging) and angular (diffraction)

backscattered electrons, emission of secondary electrons and emission of electromagnetic radiation, each of which is detected by specialized detectors. The resulting image shows a distribution map of the intensity of the signal being emitted from the scanned area of the sample.

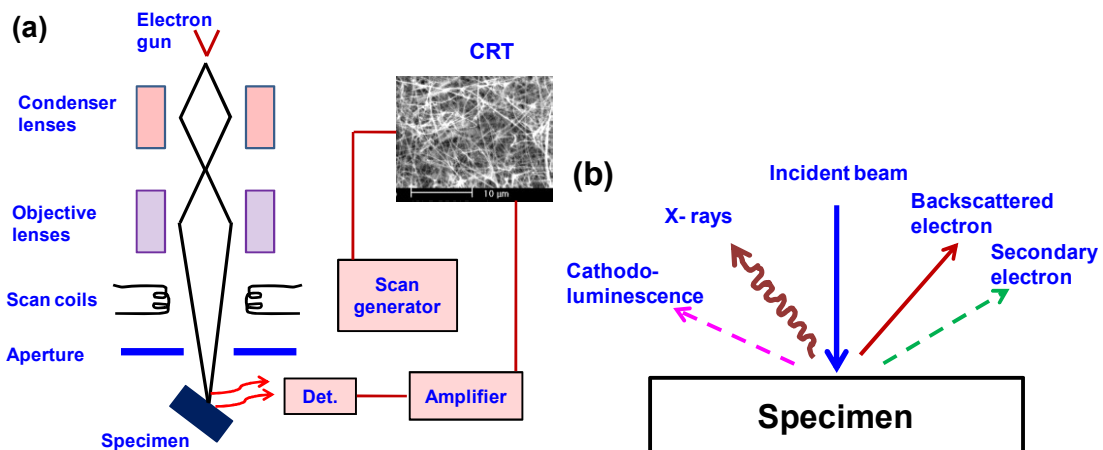


Figure 2.3 (a) Schematic diagram showing the components of a scanning microscope (b) shows the signals which are observed as a result of incident beam and sample interaction and are used in the SEM

In the SEM system (figure 2.3(a)), the electrons, emitted from the source (or gun), are accelerated to an energy which is usually between 1 keV and 30 keV. Two or three condenser lenses then demagnify the electron beam, so that the electron beam hits the specimen. It has a diameter of only 2-10 nm. The region into which the electrons penetrate the specimen is known as the interaction volume. The various processes that take place in the interaction volume are shown in fig. 2.3(b). The secondary electrons are those electrons which escape from the specimen with energies about 50 eV and below. These secondary electrons, which have a high yield, commonly are used for imaging in an SEM. In this work, Philips XL30CP SEM system is used. This SEM is equipped with a tungsten (W) source and is maintained at a base pressure of 10^{-6} mbar. The acceleration voltage is 30 keV and the resolution is 5 nm at 30 keV. It is equipped with everhart-thornley, RBS and EDS detectors.

2.2.2 Vapor–solid mechanism

VS process occurs in many catalyst-free growth processes. Under high temperature condition, source materials are vaporized and then directly condensed on the substrate. Once the condensation process take places, the initially condensed molecules form seed crystals serving as the nucleation sites. As a result, they facilitate directional growth to minimize the surface energy. It is often called self-catalytic growth since the nanostructures grow directly from vapor phases.

2.3 Characterization techniques

In this section, characterization techniques used to investigate the properties of nanostructures are explained.

2.3.1 Structural characterization

Structural and geometric factors play an important role in determining the various aspects of nanowires, such as their electrical, optical and magnetic properties. In this section, scanning electron microscopy (SEM), transmission electron microscope (TEM), and X-ray diffraction (XRD) techniques are discussed. These techniques have been extensively used for the preliminary characterization of the nanostructures.

2.3.1.1 Scanning electron microscopy

SEM usually produces images down to length scales of ~ 10 nm and provides valuable information regarding the structural arrangement, spatial distribution, wire density, and geometrical features of the nanowires. SEM produces images by probing the sample with an electron beam with an energy ranging from a few hundred eV to 30 keV. The incident electron beam interacts with the sample and resulting in the reflection of

nucleation seeds. The typical feature of the VLS reaction is that the nanowires grow only in the areas seeded by metal catalysts, and their diameters are mainly determined by the sizes of the catalysts. The surface of the liquid is a preferred site for deposition because of its large accommodation coefficient. The liquid solution in contact with the crystalline substrate tries to maintain the equilibrium composition at a given deposition temperature. The concentration gradient in the solution provides the driving force for the diffusion from the liquid surface to the liquid-solid interface and crystal growth occurs by precipitation at the solid-liquid interface.

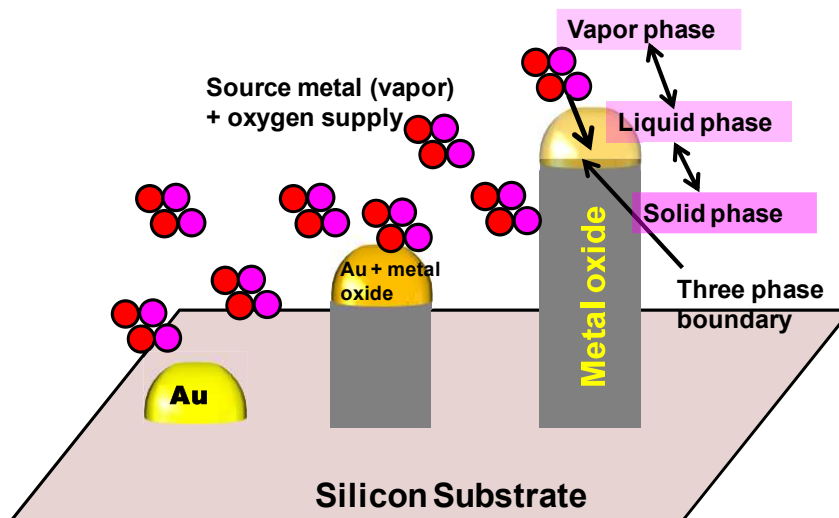


Figure 2.2 Vapor-liquid-solid mechanism illustrated for the metal oxide nanowires

Thus, the unidirectional growth of nanostructures is the result of the difference in the sticking coefficients of the impinging vapor source atoms on the liquid (the catalytic droplet) and on solid surfaces. An ideal liquid surface captures all impinging source atoms, while a solid surface of nanostructure/substrate rejects almost all source atoms. This classical VLS mechanism is applicable to the growth of many nano-scale wires produced today. A large number of oxide nanowires has been synthesized via this catalyst-assisted mechanism, such as ZnO [64], CdO [65], TiO₂ [66], SnO₂ [67], In₂O₃ [68], and Ga₂O₃ [69].

material already present in the substrate. At high temperatures, source material reacts with the O_2 and participates in the growth of nanostructures. Gold coating of about 10-20 nm is done for the initial nucleation to start the growth of nanostructures. In thermal evaporation method, reactant material directly deposits on the substrate, which is put above the source material. In the vapor transport method, substrate deposited with 10-20 nm gold film is placed at downstream from the source material for nanostructure growth. The basic process involve in this method is the evaporation of source materials at higher temperature and the reactant vapors are transported to the substrate by a carrier gas. Various gases such as Ar, N_2 and O_2 are used for the vapor transport.

2.2 Growth mechanisms

There are different growth mechanisms for the nanowires, i.e. Vapor phase, oxide assisted growth and self assembly growth from the solution [62]. In this thesis, the nanostructures were grown by vapor phase; hence vapor phase growth mechanism is discussed in detail. In this mechanism, the source material once evaporated is transported by a gas carrier towards the growth site where it nucleates. The nucleation can start from the particles or catalyst, following the VS, VLS mechanisms.

2.2.1 Vapor–liquid–solid mechanism

Vapor liquid solid (VLS) mechanism has been proposed by Wagner and Ellis in 1964 [63]. VLS is one of the most important methods for preparing 1D structures, it is promising as a scalable, economical and controllable growth of different materials. In short, “any unidirectional growth with a liquid mediating phase and precursors supplied from a vapor phase is considered to grow by the VLS growth mechanism”. VLS is a catalyst-assisted growth process, which uses metal nanoclusters or nanoparticles as the

structures are fabricated by this method. The growth parameters such as substrate temperature, pressure, and flow rate, are critical parameters for the formation of nanowires in this method. To generate the vapor phases of the source materials, vacuum conditions are sometimes needed. This is because some materials may not evaporate at atmospheric pressures.

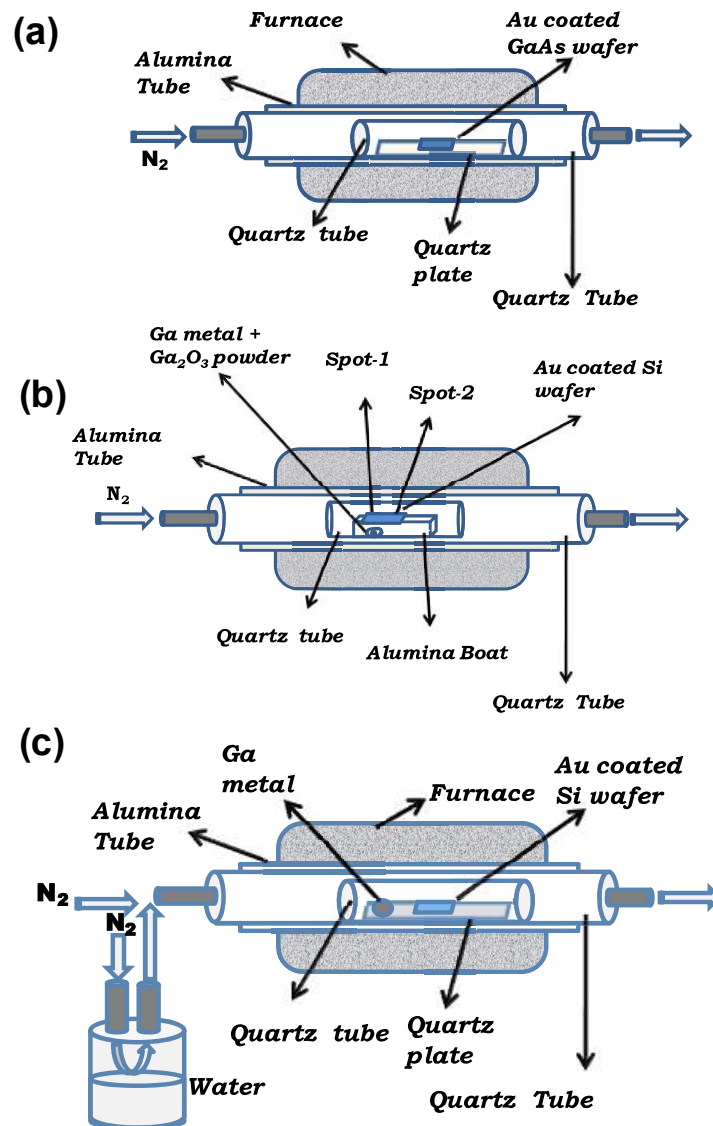


Figure 2.1 A schematic of a thermal furnace synthesis system that is used in vapor phase growth methods; a) thermal annealing method, b) thermal evaporation method and c) vapor transport method

Figure 2.1 shows three types of thermal growth methods used for the growth of β -Ga₂O₃ and In₂O₃ nanostructures. In thermal annealing method, constituent source

Chapter 2

Experimental techniques and procedures

In this chapter, experimental techniques used in this thesis are explained. These include the growth and characterization techniques. The mechanism of growth of the nanostructures and the various mechanism of PL are also described in this chapter.

2.1 Synthesis methods of metal oxide nanostructures

A variety of methods have been utilized to grow nanostructures. These are mainly divided into two categories: vapor phase growth and liquid (solution) phase growth. Most of the metal oxide nanostructures are grown via vapor phase technique, which is based on the reaction between metal vapor and oxygen gas. On the other hand, solution-phase growth methods are more flexible and an alternative to achieve lower cost. Several vapor sources are investigated for the synthesis of one dimensional nanostructures, including thermal and pulsed laser induced evaporation, chemical vapor deposition (CVD) and molecular beam epitaxy (MBE). The detail of these growth methods can be found in review articles [61]. Here, only vapor phase growth technique used in this work is discussed.

2.1.1 Vapor phase growth method

Among the available vapor phase growth methods, evaporation of source materials at high temperatures is one of the simplest, inexpensive and most popular methods used for the synthesis of oxide nanostructures. Nanowires and some interesting morphologies of nanostructures such as nanoribbons, nano-tetrapods and comb-like

3.6 Summary

In summary, the effect of O₂ gas pressure in the β -Ga₂O₃ nanostructures has been analyzed using PL spectroscopy. We observe that the PL intensity depends on the ambient O₂ gas pressure; decreasing pressure reduces the PL intensity. In comparison, single crystals of β -Ga₂O₃ are insensitive to ambient O₂ pressure. This behavior in the nanostructures is repeatable and reversible. The change in the PL intensity with O₂ pressure follows the Langmuir equation, which relates the adsorption/desorption of the gases on the surface of the material to the partial pressure of the gas. The observation is explained in terms of the surface states present beyond 4.21 eV above the valence band that are produced due to the O₂ adsorption/desorption. This model can also explain previously reported results on the photo-induced electrical properties of β -Ga₂O₃ nanostructures. The results provide an understanding of adsorption/desorption related mechanism in β -Ga₂O₃ nanostructures and a route for room-temperature sensing of O₂ by β -Ga₂O₃ nanostructures.

nanostructures by O₂ desorption. From the band model, it is clear that carriers cannot be excited from the valence band or the shallow acceptor defect levels (0.4 eV above the valence band) to the conduction band or the shallow donor levels with the 3.81 eV excitation. The only excitation channel possible is from the valence band to some localized defect levels inside the bandgap [80-81]. These excited carriers eventually recombine with the shallow acceptor defect levels giving the emission at 475 nm (2.61 eV). As the generated carriers are trapped and localized at the defects in the bulk material, they are not affected by the surface states. Thus, this emission band is unaffected with oxygen adsorption/desorption process. This experiment also helps us identify the tentative location of the surface states inside the bandgap. These surface states must be at least 4.21 eV (3.81 eV + 0.4 eV) above the valence band and thus no excitation into the surface states from 3.81 eV source (laser) is observed.

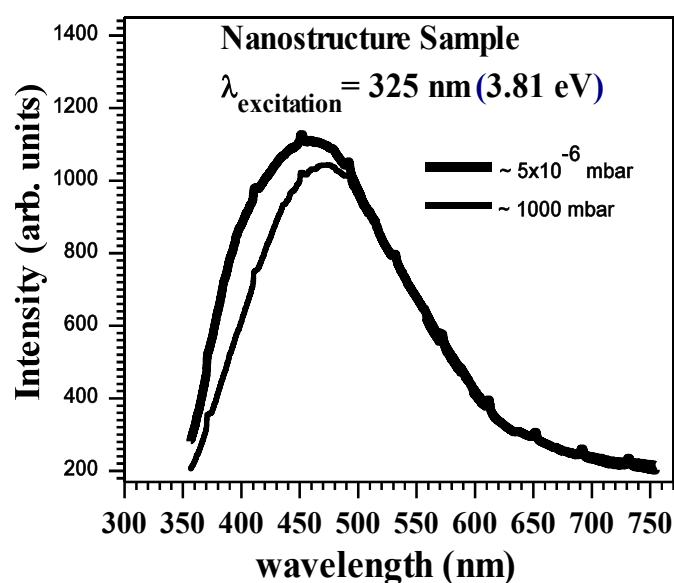


Figure 3.10. Room temperature PL spectrum of β -Ga₂O₃ nanostructure sample with 3.81 eV He-Cd laser, at different oxygen pressure conditions

conduction band are mobile and hence have a large probability of getting trapped at the surface states. However, in the case of visible luminescence both the electrons and holes are trapped in the donor and acceptor sites respectively and hence less prone to be affected by the surface trapping centers. The intensity of visible luminescence decreases only because the electron concentration in the donor is in thermal equilibrium with the conduction band. The equilibrium carrier concentration in the conduction band changes due to trapping at the surface defects and thus the intensity of the visible luminescence also decreases, but significantly less as compared to the UV luminescence. These results indicate that UV luminescence band is more prone to be effected by the surface defects as compared to the visible luminescence band.

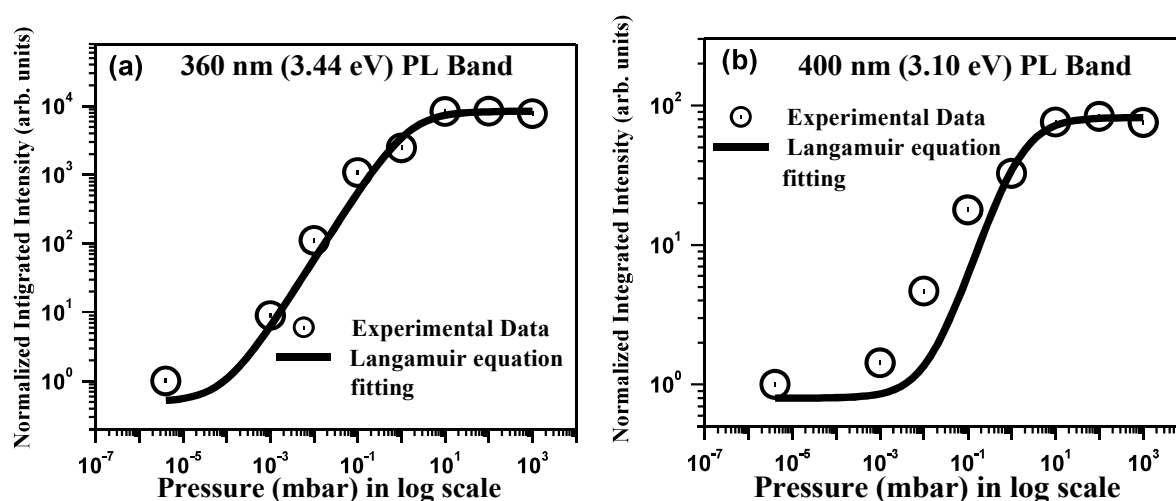


Figure 3.9. (a, b) Langmuir equation fitting for 360 nm (3.44 eV) and 400 nm (3.10 eV) PL bands

PL studies using sub-bandgap illumination at 3.81 eV from He-Cd laser have also been carried out for the β -Ga₂O₃ nanostructures. With this excitation, the carriers are excited from the valence band/shallow acceptor defect levels to mid band defect levels, from where they recombine and emit a broad band visible emission centered at 475 nm (2.61 eV), as shown in fig. 3.10. The intensity of this band is nearly constant at 1000 mbar and 5×10^{-6} mbar oxygen partial pressure conditions. This shows that the excited carriers in this case, are not affected by the defects produced on the surface of the

where, C is a constant which defines the value of PL intensity when all oxygen molecules desorbs from the surface, k is a constant which depends upon the exact role of the surface state in the PL process.

The integrated PL intensity (after deconvolving the two peaks at ~ 360 nm (3.44 eV) and ~ 400 nm (3.10 eV)) as a function of the oxygen partial pressure are shown in the fig. 3.9 (a and b). Further, the experimental data (integrated intensity) is normalized with respect to the 4×10^{-6} mbar data point in both (360 nm and 400 nm PL band) case. The normalized integrated PL intensity as a function of oxygen partial pressure is observed to fit the Langmuir equation and shown in the fig. 3.9 (a and b). In fig. 3.9 (a) 360 nm (3.44 eV) PL band is fitted with $K = 8411$ (+/- 5%) and $B=0.7$, which gives the Langmuir pressure $P_L = 1.43$ mbar. PL band centered at ~ 400 nm (3.02 eV) is fitted with $k = 81$ (+/- 5%) and $B = 0.7$, which also give the Langmuir pressure $P_L = 1.43$ mbar (shown in fig. 3.9(b)). The fact that the observed intensity variation follows the Langmuir equation, proves that the adsorption/desorption of oxygen at the surface of the nanostructure plays the dominant role in determining the PL intensity. From these observations, we conclude that the surface states are formed due to oxygen-desorption from the surface of nanostructures. Reduction in pressure reduces the oxygen coverage on the nanowire surface due to O_2 desorption. Reduced O_2 at the surface increases the surface state density that trap carriers from the conduction band thereby reducing the PL intensity. Conversely, increase in pressure enhances the adsorption of O_2 on the nanowire surface thereby neutralizing the surface states and hence the PL intensity increases.

It has also been observed (Figure 3.9 (a and b)) that the integrated intensity of 360 nm PL band reduces about 8500 times, whereas the integrated intensity of 400 nm PL band reduces only 80 times. From the proposed band model, it is confirmed that UV band is more prone to be affected by the surface state trapping centers because the electrons in

below the conduction band of $\beta\text{-Ga}_2\text{O}_3$, electrons are expected to be predominantly excited from acceptor defect levels located ~ 0.42 eV above the valence band to shallow donor levels located ~ 0.04 eV below the conduction band [77]. In bulk $\beta\text{-Ga}_2\text{O}_3$, the electrons in these shallow donor levels can be thermally excited into the conduction band. In the case of nanostructures, a significant fraction of itinerant electrons in the conduction band, diffuse to the surface of the nanostructures and get trapped at the surface states. This opens a parallel non-radiative recombination path, which reduces the intensity of the PL spectra.

Our PL results clearly show that the PL from the $\beta\text{-Ga}_2\text{O}_3$ nanostructures has strong dependence on the O_2 pressure. The volume V of the adsorbed gas at a particular pressure on a surface is given by Langmuir equation [79]

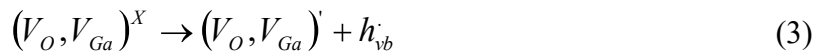
$$V = V_{\max} \left(\frac{B \times P}{1 + B \times P} \right) \quad (4)$$

where, V_{\max} is the maximum possible volume of adsorbed gas on a solid surface to have a monolayer of gas molecules, P is the partial pressure of the gas whose molecules are adsorbed on the surface and B is a constant referred to as the Langmuir constant, which is the reciprocal of the Langmuir pressure (P_L); P_L is defined as the pressure that gives an adsorbed gas content equal to one-half of the monolayer capacity.

In the case of nanostructures, the process of adsorption/desorption of the gases on the surface is an important phenomenon due to the large surface to volume ratio and this is governed by eq.(1). Thus, the PL intensity is expected to be proportional to the volume V of the adsorbed gas (O_2 in this case). Therefore, the PL intensity dependence on oxygen partial pressure can be written as:

$$I = K \left(\frac{B \times P}{1 + B \times P} \right) + C \quad (5)$$

and holes are detrapped from an acceptor to the valence band according to:



These processes are shown in fig. 3.8. The detrapped electron and holes gives the UV luminescence (~ 360 nm) via self trap excitons.

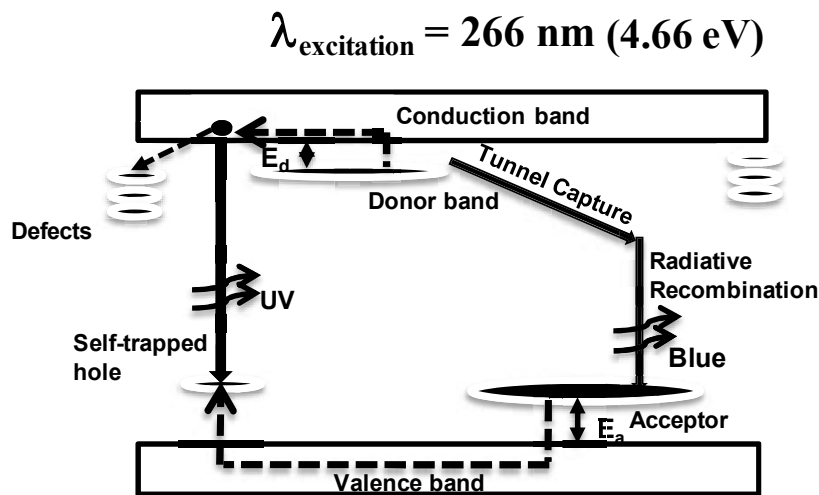


Figure 3.8. Model for the UV-visible luminescence mechanism in β - Ga_2O_3 nanostructure samples in which surface defect created on the nanowire surface are shown.

In our case, β - Ga_2O_3 nanostructures have dimensions about 40 nm to 200 nm. The bohr radius is reported to be 1.8 nm for the β - Ga_2O_3 [77]. The dimensions of the nanostructures studied in this work are much larger than the bohr radius. Hence, quantum confinement of carriers is not important in our samples. However significant surfaces to volume ratio in the nanostructures enhance the role of surface states in UV-visible PL properties. Recombination at the surface via surface states is a special case of SRH defect recombination. At the surface, the crystal lattice ends abruptly, which leaves a large number of dangling bonds and possibly also contamination from the environment. The dangling bonds and contaminants become recombination sites for carriers. Hence, considering the role of surface states on the PL properties of β - Ga_2O_3 nanostructures, Binet's model is modified to explain the PL results of β - Ga_2O_3 nanostructures with the inclusion of surface states (shown in Fig. 3.8). On excitation with 4.66 eV, which is

enhancement is a thermally stimulated luminescence and the temperature at the maximum of UV luminescence is determined by the deepest trap. From the Urbach law [77-78], a rough estimate of the trap depth can be obtained (E_a (eV) $\sim T_m$ (K)/500, where, T_m is the temperature at which the intensity of the UV luminescence is maximum). We obtain a value of $E_a \sim 0.5$ eV. Similar experiments have also been done with the bulk single crystal of β -Ga₂O₃. The intensity of the UV emission band (fig. 3.7 (c) and (d)) has a maximum at $T \sim 160$ K which corresponds to $E_a \sim 0.32$ eV. These values of activation energy, for both the bulk single crystal and nanostructures, are in reasonable agreement with the reported values ($E_a \sim 0.3$ eV in optical method and $E_a \sim 0.42$ eV in electrical method) [77]. Thus, by confirming that the temperature dependent UV PL band has similar features in single crystal β -Ga₂O₃ and β -Ga₂O₃ nanostructures, we conclude that the mechanism of UV PL in single crystal β -Ga₂O₃ and β -Ga₂O₃ nanostructures is same.

3.5 Discussion on the mechanism of PL

Based on the experimental results of PL and its dependence on the oxygen partial pressure, we now propose a mechanism to explain our results. The starting point of our model is the scheme proposed by the Binet and Gourier [77]. This model is generally used for explaining PL of bulk gallium oxide. According to this model, after excitation of the acceptor, a hole on the acceptor and an electron on a donor are created according to the following equation:



and the visible emission occurs (at ~ 400 nm in our case) via the reverse reaction.

At room temperature, electrons are detrapped from the donor level to the conduction band according to:



are fitted with the two Gaussians centered at UV region (360 nm) and visible region (~410 nm). The intensity of the UV emission at 360 nm is plotted in fig. 3.7(b) and it has a maximum at $T \sim 250$ K.

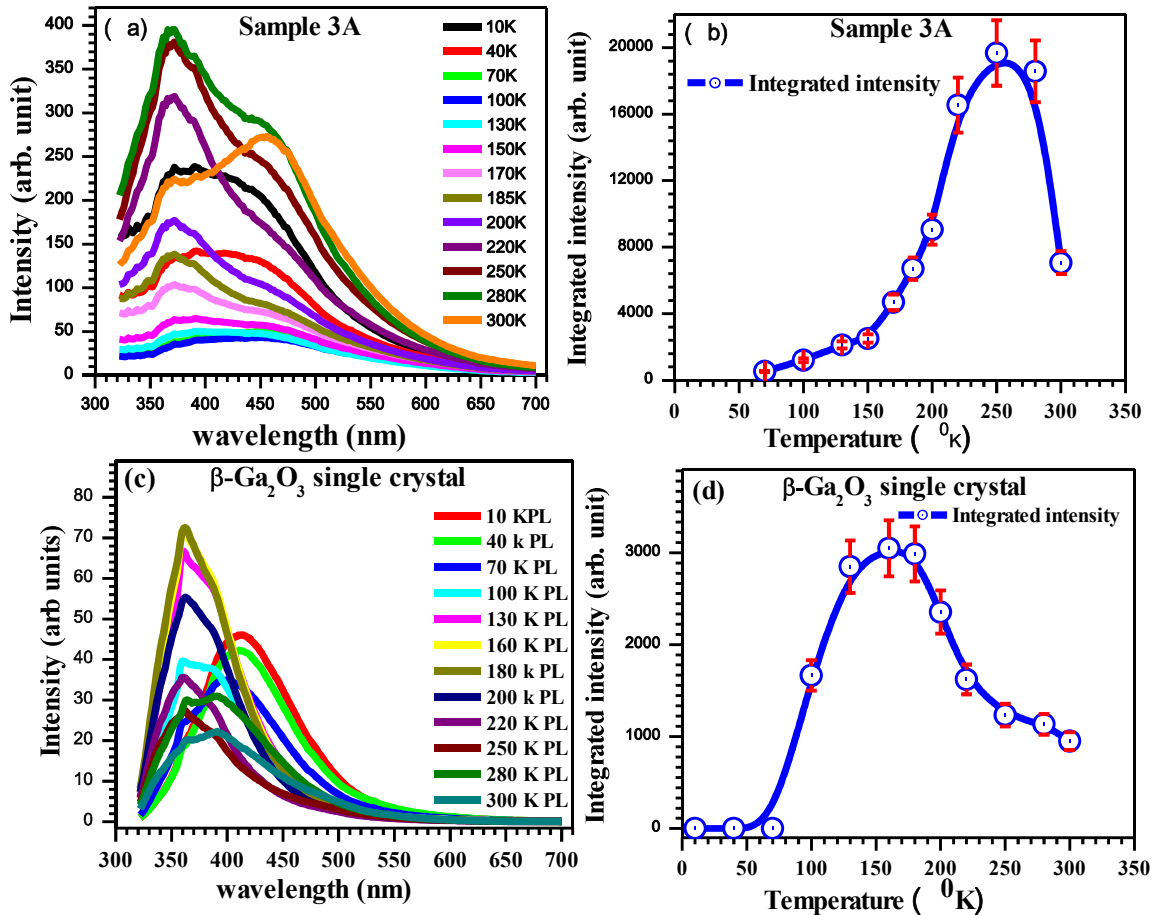


Figure 3.7 (a) Temperature dependent PL spectra of $\beta\text{-Ga}_2\text{O}_3$ nanostructures, (b) the plot of UV luminescence integrated intensity as a function of temperature (with $\pm 10\%$ error bar) in which an enhancement of the UV luminescence at 250 K is observed, similarly (c) shows temperature dependent PL spectra of bulk gallium oxide single crystal and (d) the plot of UV luminescence integrated intensity as a function of temperature (with $\pm 10\%$ error bar) in which an enhancement of the UV luminescence at 160 K is observed.

The enhancement of the UV luminescence at 250 K can be explained by the model proposed for $\beta\text{-Ga}_2\text{O}_3$ single crystal by Binet and Gourier. According to this model both electrons and holes are detrapped and can migrate through the solid and meet to form a self-trapped exciton which recombines and emits a UV photon. Therefore, the UV

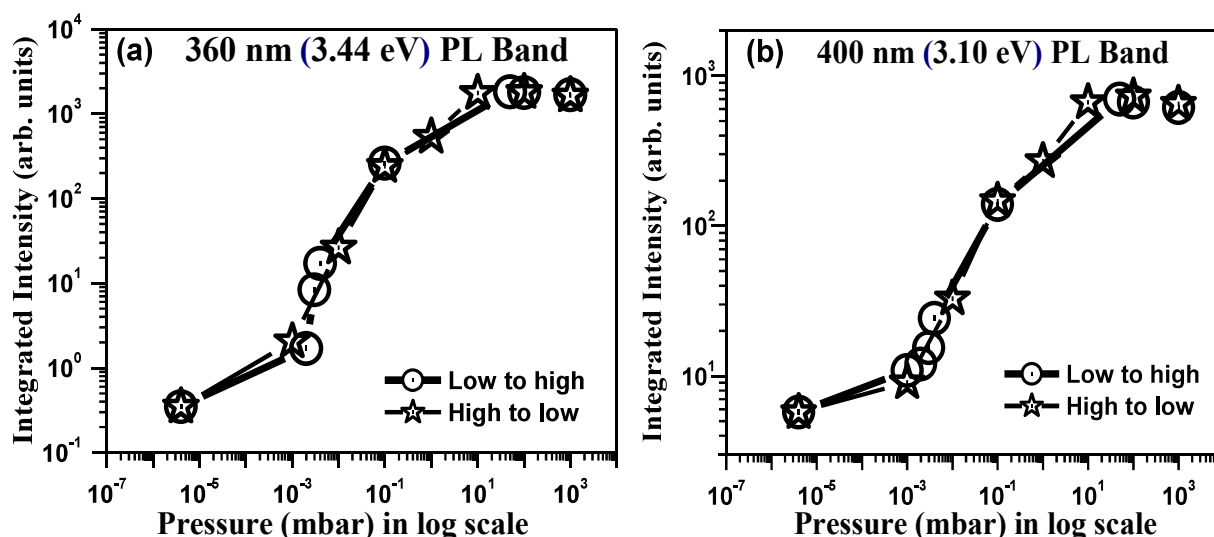


Figure 3.6. (a) Plot of O_2 pressure versus integrated intensity for the 360 nm (3.44 eV) peak in the ascending and descending pressure conditions, (b) the same for the 400 nm (3.10 eV) peak

All the PL spectra of nanostructures have been fitted with two Gaussian profiles centered at UV (360 nm) and visible (400 nm) region. The integrated intensity of these two peaks is plotted as a function of O_2 pressure and is shown in fig. 3.6 (a) & (b). It can be clearly seen that for both peaks, the integrated intensity decreases as we lower the pressure and increases as pressure increases. This characteristic is highly repeatable. Minor differences in the integrated intensity between descending and ascending pressure conditions may be due to various reasons like fitting errors, non uniformity of the nanostructures, uncertainties in the pressure measurements, laser fluctuations during measurement etc. It has also been observed that reduction in the integrated intensity of UV band (360 nm) is very large compared to the visible band (400 nm).

Temperature dependent PL measurements have been carried out to investigate the origin of UV luminescence in the bulk β - Ga_2O_3 and β - Ga_2O_3 nanostructures, which helps in correlating the observed surface related modification and the optical properties. The temperature dependent PL spectra are shown in the fig. 3.7 (a). It can be clearly seen that an enhancement of the UV luminescence is observed, with a shoulder rising in the UV domain (about 360 nm) in the spectra and has a maximum at $T \sim 250$ K. The PL spectra

PL spectrum of bulk β -Ga₂O₃ single crystal also consists of two luminescence bands centered in UV (~370 nm) and visible region (437 nm). Qualitatively, the PL spectrum from the nanowires sample is identical to single crystal β -Ga₂O₃ sample and both have two luminescence bands in the UV and visible region. There is a difference in the peak positions of the UV and visible band. This is due to different growth mechanism and size of the nanostructures.

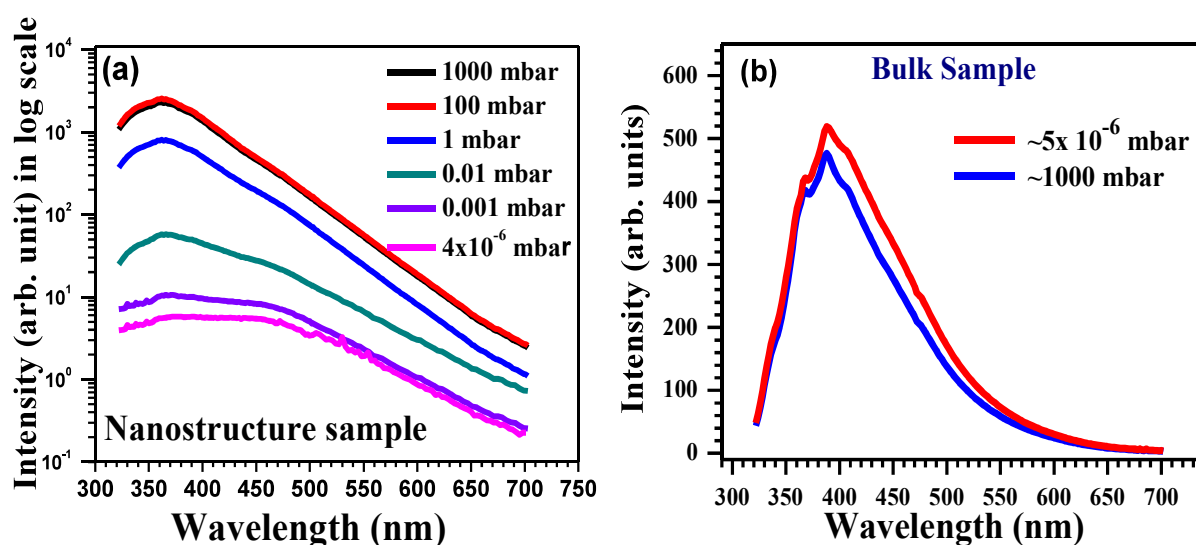


Figure 3.5. Room temperature PL spectra of β -Ga₂O₃ (a) nanostructure and (b) bulk sample, at different oxygen pressure conditions using the excitation energy of 4.66 eV

PL measurements have also been done at different O₂ partial pressure. Figure 3.5(a and b) shows the room temperature PL spectra of β -Ga₂O₃ nanostructures and bulk β -Ga₂O₃ single crystal under different O₂ pressures ranging from 1000 to 4×10^{-6} mbar. We have observed that the PL intensity decreased with decreasing O₂ partial pressure in the case of nanostructures. No significant change in PL intensity from β -Ga₂O₃ single crystal is observed when the O₂ pressure changes from 1000 to 5×10^{-6} mbar. The results observed in the nanostructures clearly indicate the emergence of nonradiative recombination processes due to the O₂ deficiency at the surface of the nanostructures.

distributed on the substrate surface. During the process of heating, Ga vapor reaches the substrate and forms Au-Ga eutectic clusters, which are the initiation points for the wire growth. Trace amounts of oxygen in the furnace tube, oxygen impurities in the nitrogen gas and the thin oxide film on the substrate act as sources of oxygen. The β -Ga₂O₃ wires have a gold droplet at the tip, suggesting the classical VLS growth mechanism for nanowires [63]. The presence of other kinds of nanostructures like nanosheets and nanoribbons follow the vapor-solid (VS) mechanism [75] where the degree of super saturation in the gaseous phase is a critical factor for morphology of the final growth products.

3.4 Effect of O₂ adsorption/desorption on the PL properties

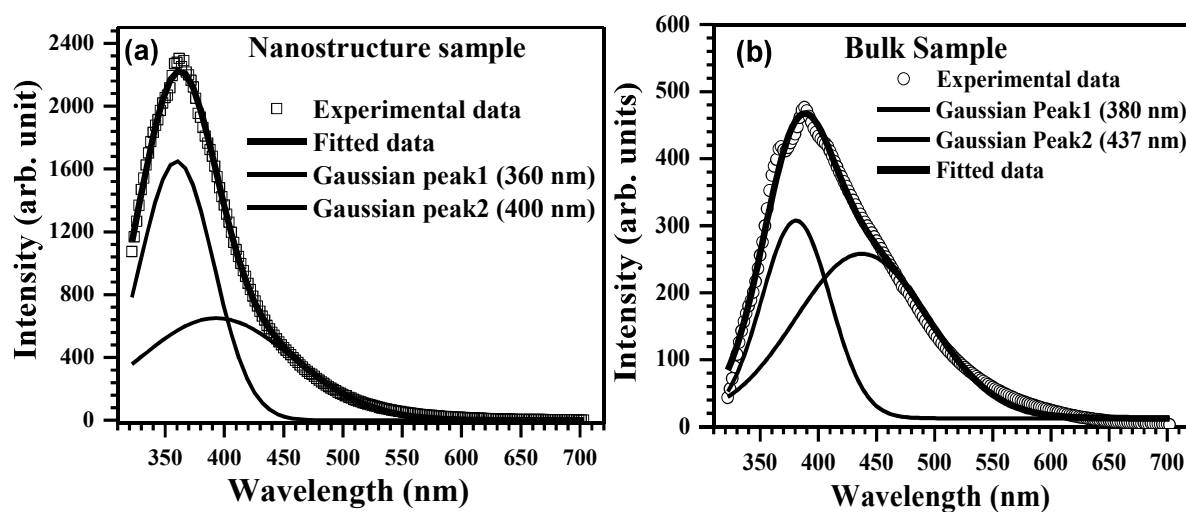


Figure 3.4. Room temperature PL spectra of β -Ga₂O₃ (a) nanostructure and (b) bulk sample fitted with two Gaussian peaks, using the excitation energy of 4.66 eV

Figure 3.4(a) shows the room temperature PL spectra of β -Ga₂O₃ nanostructure sample. The PL spectrum is fitted by two Gaussian and the fitting is shown in the fig. 3.4(a). This shows that PL spectrum consists of two luminescence band centered at UV (360 nm) and visible (400 nm) region. For comparison, PL study has also been carried out on bulk single crystal β -Ga₂O₃ sample (details of the sample are provided elsewhere [76]).

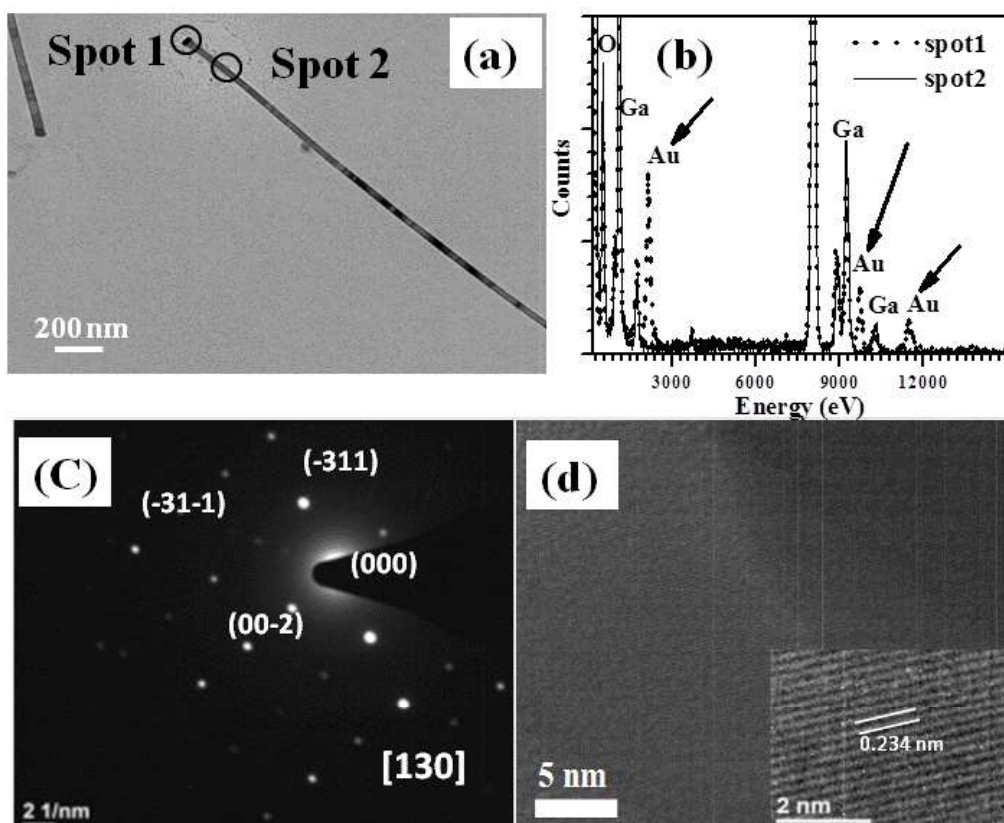


Figure 3.3. TEM, SAED and HRTEM images of β -Ga₂O₃ nanowire which contain gold on the tip, nanowire is 40 nm in diameter with lattice spacing 0.234 nm

Figure 3.3 (a) shows a TEM image of a single β -Ga₂O₃ nanowire that is about three microns long and 40 nm in diameter. The nanowire is straight and smooth with an Au tip at the end as shown in fig. 3.3(b) in which EDS spectrum was taken at two spots as shown in the fig. 3.3 (a). Spot (1) is taken near the tip and spot (2) is taken on the wire away from the tip. The EDS results show that the wire contains gold at the tip. This indicates that the β -Ga₂O₃ nanowires are grown via a VLS growth mechanism. Figure 3.3 (c) and (d) show a defect-free, electron diffraction pattern and high resolution image of the nanowire with an inter-atomic spacing of 0.234 nm, which correspond to the (-3 1 1) lattice planes. The selected area electron diffraction (SAED) pattern of this nanowire is indexed to [1 3 0] zone axis of β -Ga₂O₃.

In our experiments, the Si wafers coated with a thin film of gold, are used as substrates. On increasing the temperature, the gold film forms gold clusters, uniformly

nm, $b=0.304$ nm, $c=0.580$ nm, $\beta=103.7^\circ$ (JCPDS card no. 76-0573) of $\beta\text{-Ga}_2\text{O}_3$. Figure 3.2 (b) shows the SEM image of the as synthesized ensemble of nanostructures grown on Si substrate. The nanowires were found to have diameter in the range of 40-100 nm and length up to few hundred microns.

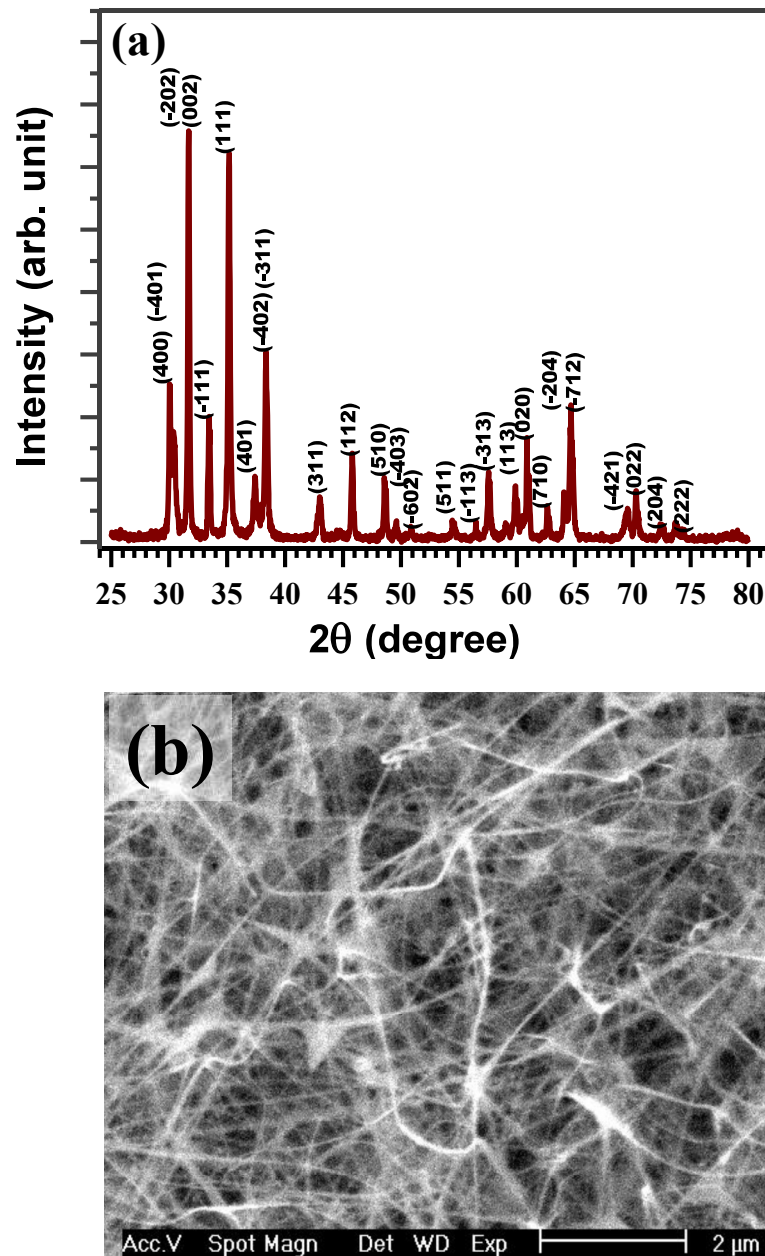


Figure 3.2. (a) GIXRD pattern of as synthesized $\beta\text{-Ga}_2\text{O}_3$ nanostructures and (b) their SEM image

3.2 Experimental procedure

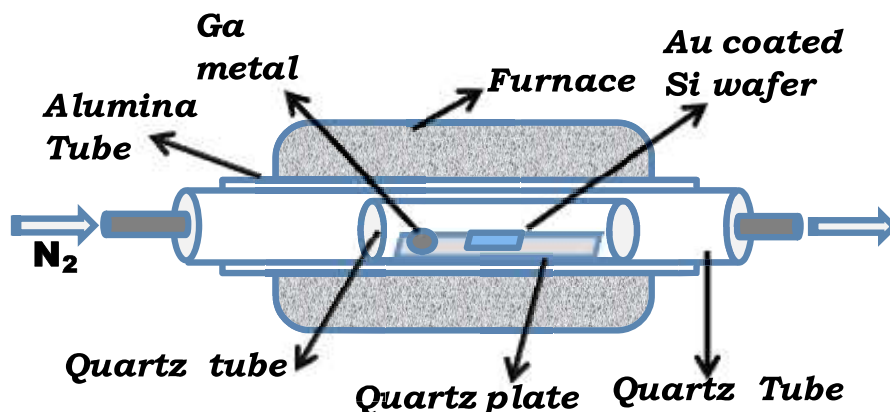


Figure 3.1. a schematic illustration of the experimental setup for the growth of β -Ga₂O₃ nanostructures

The Gallium oxide nanostructures were synthesized by vapor transport method. Ga metal (Alfa-Aesar, 99.999%) was used as the Ga source for the growth of β -Ga₂O₃ nanostructures. The Si (100) substrates (15 mm X 15 mm) coated with a gold film of about 10-20 nm thickness by thermal evaporation at 10^{-6} Torr, were used as a substrates for nanostructure deposition. A drop of gallium metal (~ 1 gm) and as prepared gold coated Si substrates were placed 10 mm apart on a quartz plate. This quartz plate was inserted into a 25 mm quartz tube which was inserted into another 42 mm quartz tube. They were then loaded into a 2 inch alumina tube of the tube furnace. The furnace was purged with 99.999% pure nitrogen gas for 10 min. and its temperature was then raised to 900°C in 45 mins. This temperature was maintained for one hour in a continuous flow of nitrogen at 0.5 lpm. After the reaction, the furnace was naturally cooled down to room temperature.

3.3 Structural properties and growth mechanism

Figure 3.2 (a) shows a typical GIXRD pattern of the β -Ga₂O₃ nanostructures deposited on Si substrate. All the diffraction peaks in the pattern are indexed to β -Ga₂O₃ with monoclinic structure. They are in good agreement with the lattice constants $a=1.223$

Chapter 3

Dependence of PL from β -Ga₂O₃ nanostructures on oxygen pressure

3.1 Introduction and background

Nanostructures have large surface to volume ratio, therefore surface plays an important role in determining its properties. Applications of nanostructures, based on surface related properties are extremely important. β -Ga₂O₃ nanowire gas sensors show a reversible response to O₂ and CO gases [49]. The electrical conductivity of β -Ga₂O₃ nanowires is also extremely sensitive to NH₃ and NO₂ [73]. Surface-related processes, especially O₂ adsorption, show significant effects on the photoelectric properties of ZnGa₂O₄ nanostructures [74]. Most of the electrical conductivity based sensing devices of gallium oxide nanostructure, at room temperatures, are reported to be insensitive to O₂ without photo-excitation [55].

Recently, sensing via Photoluminescence (PL) measurements have also emerged as an alternative route of gas sensing at room temperatures [59-60]. The principal advantage of an all optical sensors is that the complications, which arise due to electrode fabrication and contact making, are eliminated. Thus, the approaches based on PL from nanostructure metal oxides are promising for application to sensors. This has motivated us to investigate the PL properties of β -Ga₂O₃ nanostructures in this direction. In this chapter, effect of O₂ pressure on the PL properties of Gallium oxide nanostructures, grown by vapor transport method, have been investigated. The mechanism of PL and the role of surface states in determining the PL characteristics are also discussed.

sensitive PL properties of β -Ga₂O₃ nanostructures that arise due to the carrier gas has also been discussed.

the dominating emission band in the sample 3A and its intensity reduces about 100 times, whereas the visible luminescence band is the dominating emission band in sample 3B and its intensity reduces by about 10 times only. The reduction in the visible luminescence intensity is less in the sample 3B as compared to the UV luminescence in the sample 3A. As mentioned before, the UV luminescence is more sensitive to the surface defect states because the conduction band electrons which are responsible for this luminescence band are trapped at the surface defects and recombine non-radiatively. In the case of sample 3B, permanent surface defects that are already present due to growth in moist environment, suppress all the UV luminescence. As the visible luminescence is less sensitive to the surface defect states, the sensitivity of PL to oxygen concentration reduces.

4.7 Summary

In summary, three growth methods (thermal annealing, thermal evaporation and vapor transport) have been used for the synthesis of β -Ga₂O₃ nanostructures, and the structural, morphology and optical properties have been compared. The study shows that β -Ga₂O₃ nanostructures grown by all three methods have single crystalline phase. The vapor transport method has the best morphology control among all the three methods. Based on the analysis of the PL data, we conclude that β -Ga₂O₃ nanostructures grown by thermal evaporation and vapor transport methods have significantly less surface defects as compared to those synthesized by thermal annealing method. The lack of morphology control and the presence of surface particulates observed in the thermal evaporation make vapor transport, a more suitable method for the growth of good quality β -Ga₂O₃ nanostructures. In the vapor transport method, effects of different carrier gas (dry N₂ and moist N₂) have also been investigated. The effect of the surface defects on the oxygen

UV luminescence band intensity dominates the PL spectra for the samples which have fewer surface defects. Although XRD and TEM measurements confirm pure single crystalline β -Ga₂O₃ phase in all the cases, the reduced surface defect density is observed in samples 2A and 2B at spot-2 and sample 3A as compared to the samples synthesized under other deposition conditions. As discussed above, thermal evaporation method (used in case of sample 2A, 2B and 2C) have poor control on the morphology of the β -Ga₂O₃ nanostructures and have surface particulate related issues, hence vapor transport method with dry N₂ carrier gas comes out as a better method.

4.6 Effect of surface defects on the O₂ partial pressure dependent PL behavior

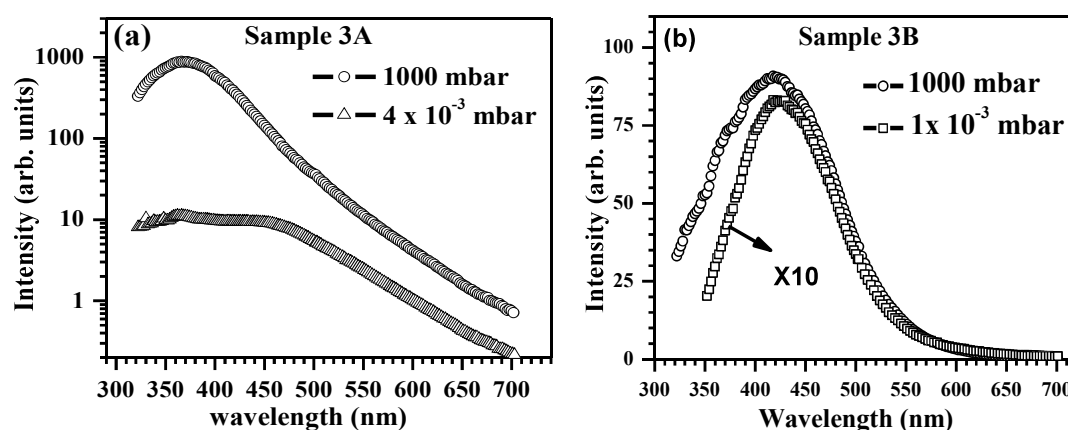


Figure 4.13. (a-b) Room temperature PL spectrum of β -Ga₂O₃ nanostructure sample 3A and 3B at different O₂ pressure conditions

To determine the role of these surface defects on the sensitivity of β -Ga₂O₃ to ambient O₂ concentration, PL data for two samples, 3A and 3B are recorded at different ambient oxygen partial pressure. These two samples are nearly identical in the morphology and density of the nanostructures and hence easily comparable. Figure 4.13 (details of the experiment can be found in chapter 3) show that the total PL intensity reduces in both the samples as the O₂ concentration reduces. UV luminescence band is

visible luminescence. Similar case is observed for the sample 2C at spot-2, where the change in the morphology of the as grown structure (the surface particulates seen in the SEM figure of the spot-2) is directly correlated to the relative reduction in the UV emission intensity.

Samples 3A and 3B are grown in the same condition except the carrier gas is moist N₂ in case of sample 3B instead of dry N₂ used in sample 3A. The crystal quality determined from the XRD and TEM shows that both are crystalline. The SEM shows the similar morphology and nearly same density of the nanostructures for both the samples. But in the PL measurements, one can see from the fig. 4.12(a) and (b) that the UV luminescence intensity decreases drastically in the sample 3B as compared to 3A. Unlike the samples 2A, 2B and 2C, PL intensity of samples 3A and 3B can be compared because of the similar morphology and nearly the same density of the grown nanostructure. After fitting the PL spectrum with two gaussians (one each for the UV and visible emissions), it is found that the total integrated intensity of visible luminescence in sample 3B is about half of sample 3A, while the UV luminescence peak in sample 3B nearly disappeared. Sample 3B was grown in moist N₂ environment and the water vapor deposited on the surface of the nanostructures in OH⁻ form, which acts as nonradiative trap centers [83, 90].

From the above discussion it is clear that the states on the surface of β -Ga₂O₃ nanostructures are formed due to gallium diffusion on the as grown β -Ga₂O₃ nanostructures in sample 1, due to the presence of surface particulates on the as grown β -Ga₂O₃ nanostructures in the sample 2 series, and due to moisture in sample 3B. Contrary to the surface defects discussed in the previous study (chapter 3) where they were formed by gas adsorption/desorption and were bonded weakly on the surface, the surface defects discussed in this chapter are permanently bonded on the surface. It has been observed that

is the same (i.e. same spot) and there is a change in the surface state density e.g. in our previous O₂ pressure dependent study, the density of the nanostructures did not change (measurement were done at the same spot (~ 500 μm laser spot)) and the surface defects were the only responsible factor for the reduction in the total PL intensity. In this study it has been shown that decrease in the total PL intensity was ~ 300 times, while the change in the UV luminescence integrated intensity (~ 8000 times) is large compared to the visible luminescence integrated intensity (~ 80 times) [84]. Hence, the relative intensity of the UV and visible luminescence does not depend on the density of the nanostructures and only gives the information about the surface defects. If defects produced on the surface of the nanostructures (either by chemical adsorption which is permanent type or by physical adsorption/desorption), UV to visible luminescence intensity ratio changes [83-84]. We have thus used the model, discussed in chapter 3 for the β-Ga₂O₃ nanostructures, to explain the observed PL results.

In sample 1, the UV luminescence intensity is less as compared the visible luminescence intensity. In this method, the growth starts from the molten gallium which is present on the GaAs substrate. Side growth on the nanostructure surface is observed which is attributed to the diffusion of gallium along the nanowires. This diffusion of gallium on the as grown nanostructures produces surface defects which affects the UV and visible luminescence intensity and their ratio. In case of samples 2A, 2B and 2C, spot-1 is just above the source material and hence the vapor concentration is very high and the material is directly deposited on the as grown gallium oxide structures (shown in fig. 4.4). It can be seen that the deposition of gallium oxide particulates increase as the growth temperature increases. These surface particulates are the source of the non-radiative defect centers. Thus, UV emission, which is significantly affected by the surface defects as compared to the visible emission, decreases much more as compared to the

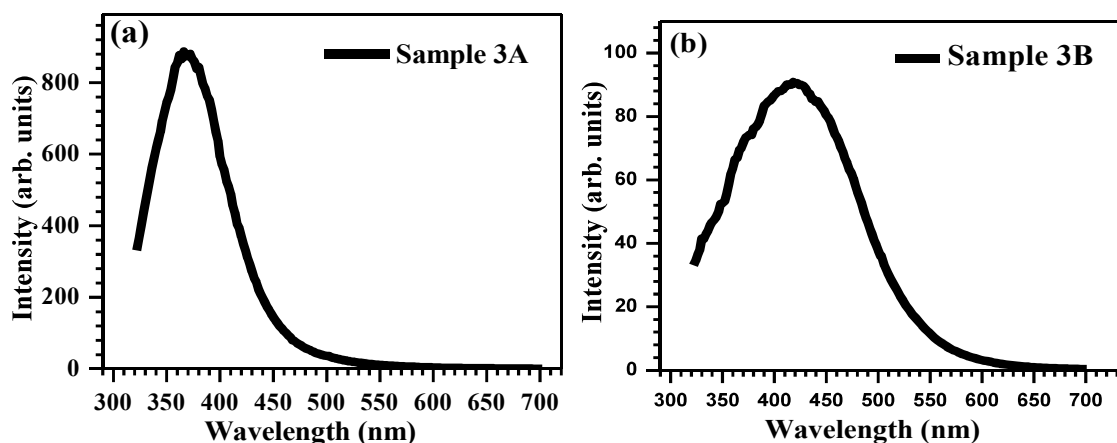


Figure 4.12. Room temperature PL spectra of β -Ga₂O₃ nanostructures in the (a) sample 3A and (b) sample 3B.

Figure 4.12(a-b) shows the room temperature PL spectra obtained from samples 3A and 3B in which a broad UV-visible emission band is observed. Sample 3A and sample 3B are grown at the same temperature with the carrier gases being dry nitrogen and moist nitrogen (bubbled through water) respectively. The SEM results show similar morphology in both the cases and XRD data does not show any change in the crystal structure. But, the PL intensity of sample 3B reduces about 10 times with respect to the sample 3A. The PL spectrum also shows that the UV luminescence intensity decreases drastically with respect to the visible luminescence intensity in the sample 3B.

4.5 Discussion on the observed PL results

In this study, two factors have been identified for the total PL intensity reduction; one is density of nanostructures on the substrate and second is defects on the surface of the nanostructures. It is difficult to distinguish the responsible factor (between both of them) for reduction in the total PL intensity in the different samples. If there is a change in the density of the nanostructures only, the total PL intensity changes without any significant change in the relative intensity of the UV and visible luminescence (e.g. sample 2A/spot-2, sample 2B/spot-2 and sample 3A). The other case is when the density

The PL spectra for samples 2A, 2B, and 2C are plotted in fig. 4.10 (a-c). Figure 4.7(a) shows the PL spectra taken at spot-1 and spot-2 in sample 2A. UV luminescence band, measured at spot-2, dominates the spectra whereas both the UV and visible band have comparable contribution in PL spectra measured at spot-1. The relative intensity of UV luminescence with respect to the visible luminescence reduces from spot-2 to spot-1. Similarly for sample 2B (shown in fig. 4.10(b)), the relative intensity of UV luminescence with respect to the visible luminescence reduces from spot-2 to spot-1. PL spectra, taken at spot-1 in sample 2C, show the complete reduction in the UV luminescence band (shown in fig. 4.7(c)). Further, in spot -2, total PL intensity reduces along with the reduction in the relative intensity of UV and visible band.

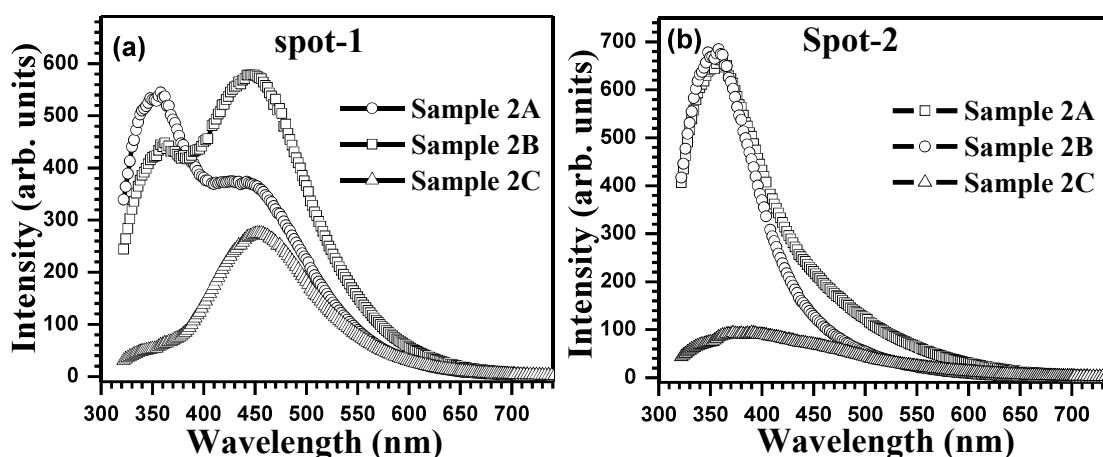


Figure. 4.11. Comparative room temperature PL spectra of sample 2A, sample 2B and sample 2C for the spot-1 and spot-2 are shown in the figure (a) and (b) respectively.

A comparison of the luminescence from samples 2A, 2B and 2C for both the spots-1 and 2 are shown separately in fig. 4.11 (a and b). Figure. 4.11(a) shows a reduction in the UV luminescence intensity with respect to the visible luminescence intensity as the growth temperature increases for spot-1. The relative intensity of the UV luminescence with respect to the visible luminescence also decreases at spot-2 for sample 2C (shown in fig. 4.11(b)).

using three Gaussian curves. The fitting shows the PL spectrum consist of three luminescence bands centered at ~ 371 nm (UV), ~ 443 nm (visible) and 457 nm (visible) respectively. Figure 4.9 (b) shows PL spectrum centered at 455 nm of Ga_2O_3 film grown on GaAs substrate during the initial optimization of the growth parameters. Therefore, the peaks centered at 371 nm and at 443 nm are attributed to the nanostructures and higher wavelength peaks (457 nm) is attributed to the underlying Ga_2O_3 film. The results reveal that PL intensity of UV luminescence is relatively less as compared to the visible luminescence intensity in the $\beta\text{-Ga}_2\text{O}_3$ nanostructures.

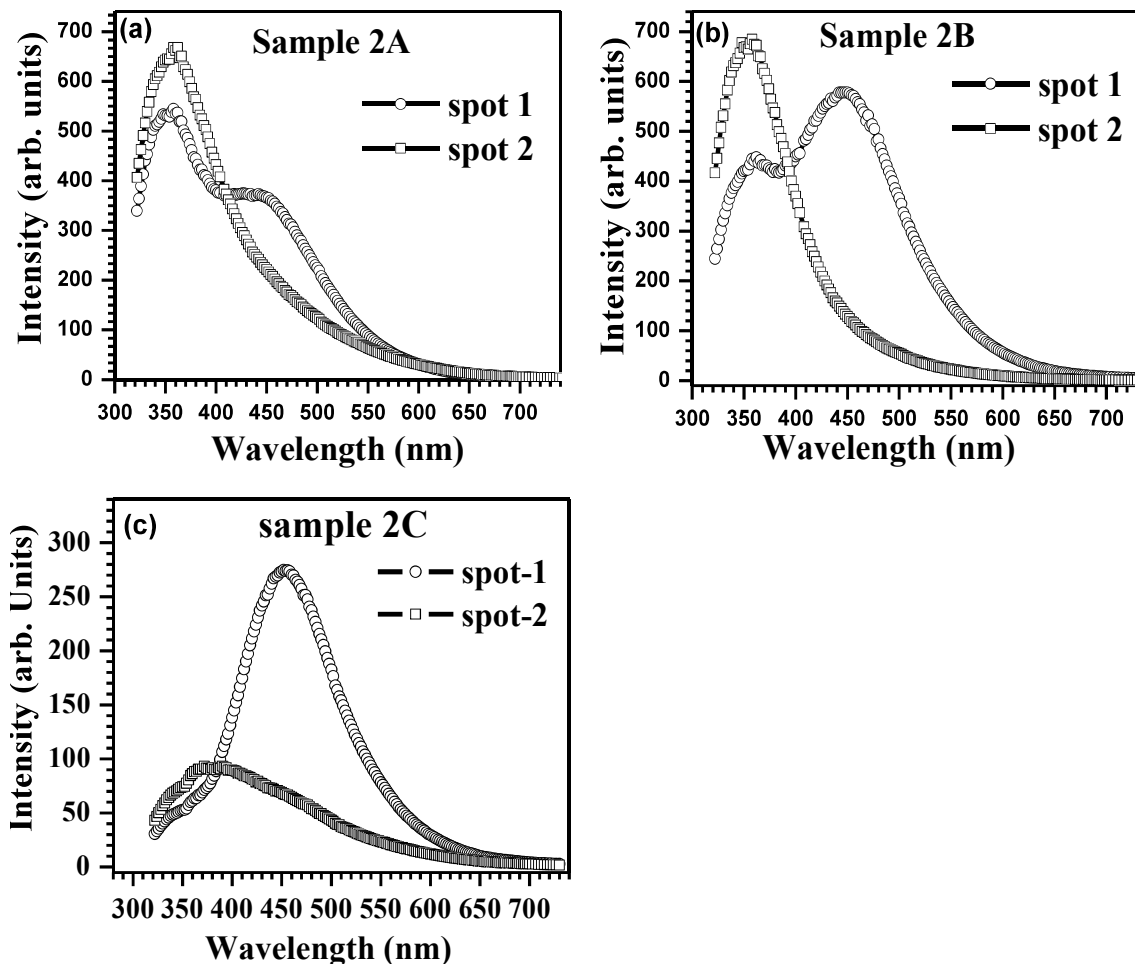


Figure 4.10. Room temperature PL spectra of $\beta\text{-Ga}_2\text{O}_3$ nanostructures in the (a) sample 2A (for spot-1 and spot-2), (b) sample 2B (for spot-1 and spot-2) and (c) sample 2C (for spot-1 and spot-2).

is indexed to [202] zone axis of β -Ga₂O₃. The VLS growth of nanowires has been confirmed in this method and has already been discussed in the previous chapter.

SEM and TEM analysis reveal important information of the grown β -Ga₂O₃ nanostructures. Nanostructure observed in sample 1 has pure and single crystalline β -Ga₂O₃ phase but the nanowires are tapered and growth control is not very good. In the case of thermal evaporation method (set of sample 2), good quality nanowires have been observed at spot-2. Our results show that control of morphology on the entire sample is not possible in this method. These samples show different morphologies at spot-1 and 2. Since for the substrates that are just above the source material, there is a large possibility of particulates on the as grown nanostructures. Vapor transport method show a better morphology control and size distribution on the entire substrate with the equal good quality nanostructure observed in other methods. The analysis concludes that the vapor transport method is best among the used three methods in terms of quality and morphology control.

4.4 Comparison of PL results

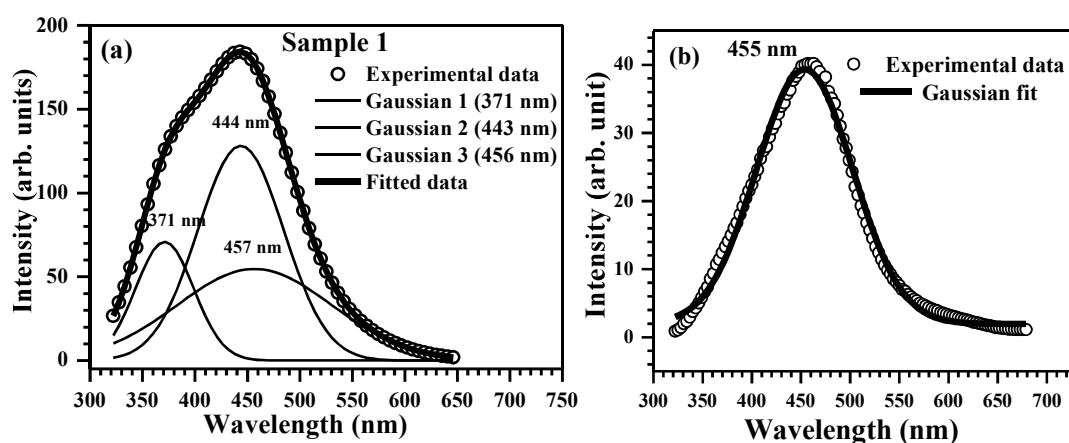


Figure 4.9. Room temperature PL spectra of (a) β -Ga₂O₃ nanostructures in sample 1 and (b) β -Ga₂O₃ thin film grown on GaAs substrate.

Figure 4.9(a) shows the room temperature PL spectrum of sample 1 in which a broad UV-visible emission band is observed. The PL spectrum has been deconvoluted

Figure 4.7 shows a TEM image of a single β -Ga₂O₃ nanowire of sample 2A that is few microns long and 60 nm in diameter. Inset of fig. 4.7 shows a high resolution image of the nanowire with an inter-atomic spacing of 0.368 nm, which correspond to the (201) lattice planes. The nanowires lack any catalytic droplets at the tip which indicates that Au particles act as a catalyst to initiate growth of β -Ga₂O₃ nanostructures. These results suggest a base growth model where nanowires grow from catalytic particles attached to the substrate surface [87].

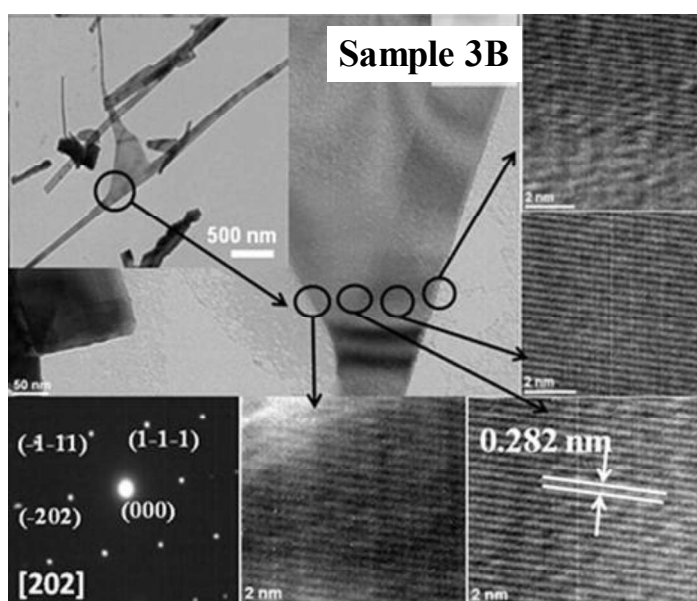


Figure 4.8. TEM and HRTEM images of the β -Ga₂O₃ nanowires grown in sample 3B. HRTEM have been done at various places of the nanowires (on the nanowire and side grown structure). Same lattice spacing 0.282 nm, which correspond to the (-202) lattice planes, is observed. SAED pattern indexed along the [202] zone axis

Figure 4.8 shows a TEM image of a single nanowire of sample 3B with side growth. Insets of fig. 4.8 show a defect-free, electron diffraction pattern and high resolution image of the nanowire with an inter-atomic spacing of 0.282 nm, which correspond to the (-202) lattice planes. Some HRTEM images were also taken from the side grown region of the nanowire. Same inter-atomic spacing is observed in all the HRTEM images. The selected area electron diffraction (SAED) pattern of this nanowire

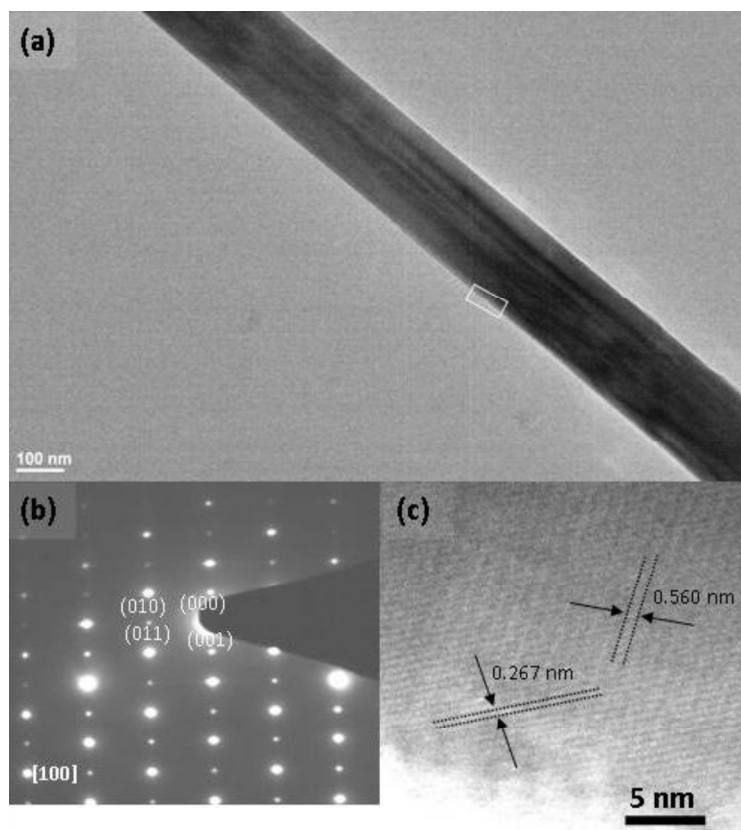


Figure 4.6. TEM and HRTEM images of β -Ga₂O₃ nanowire of sample 1; (a) TEM image of an individual nanowire, (b) the corresponding SAED pattern along [100] zone axis, (c) HRTEM image of the (001) planes with interlayer spacing of 0.56 nm.

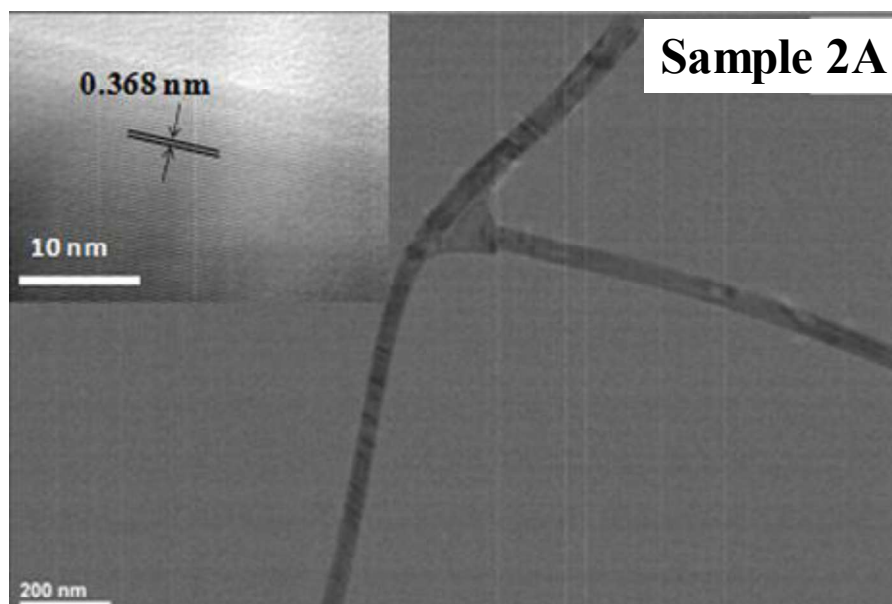


Figure 4.7. TEM and HRTEM images of the β -Ga₂O₃ nanowires of sample 2A. Nanowire is 60 nm in diameter with lattice spacing 0.368 nm which correspond to the (201) lattice planes.

nanowires are found to have diameter between 40-100 nm and length up to a few hundred microns. Similar morphology are also observed in the case of sample 3B (figure 4.5(b)). SEM pictures do not show any difference in the morphology of both the samples because of the change in the carrier gas.

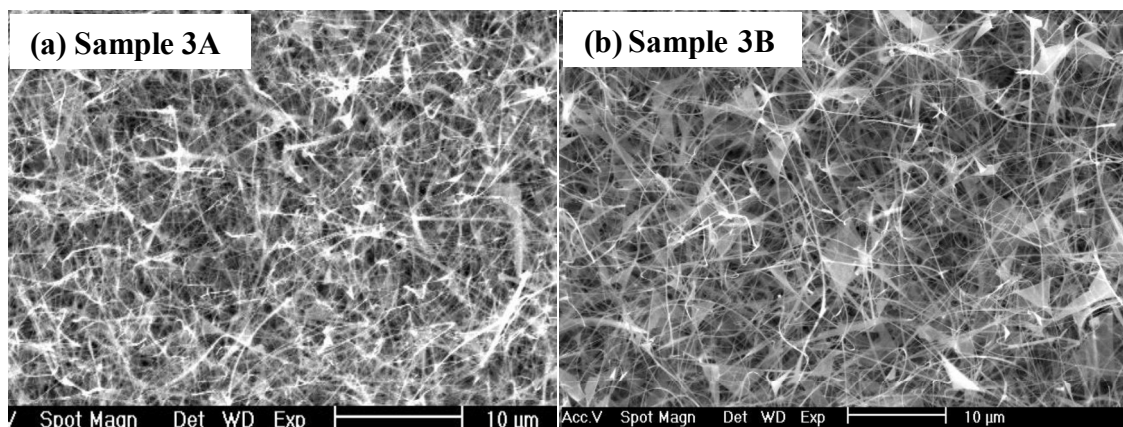


Figure 4.5. (a-b) shows the as grown nanostructures on the samples 3A and 3B respectively. An extensive growth of β -Ga₂O₃ nanowires, which have diameter of around 40-100 nm and length up to a few hundred microns, is observed in both the samples.

Figure 4.6(a) shows a TEM image of β -Ga₂O₃ nanowires grown in sample 1. The diameter of nanowire is 130 nm. The SAED pattern of this nanowire is indexed to [100] zone axis of β -Ga₂O₃ (fig. 4.6(b)). The high resolution TEM image is shown in fig. 4.6(c). The lattice fringes with a d-spacing of 0.56 nm have been observed, which correspond to the (001) lattice planes. The HRTEM and SAED results confirm the growth of nanowire along the (001) direction. In this method, GaAs wafers were coated with a thin film of gold. On increasing the temperature, the gold film forms gold clusters on the substrate surface. During the process of substrate heating, arsenic atoms evaporate from the GaAs surface, which leads to a gallium rich surface forming Au-Ga eutectic clusters. No catalytic droplets have been found at the tip of the nanostructures. This suggests that these clusters serve as the initiation point for the growth of nanostructures [87]. Trace amounts of oxygen in the furnace tube, oxygen impurities in the nitrogen gas and thin Ga₂O₃ film on the substrate act as the source for oxygen.

structures are also observed in sample 2B and 2C which are shown in figs. 4.4 (c and e) for the spot-1 (above the source) and figs. 4.4 (d and f) for the spot-2 respectively.

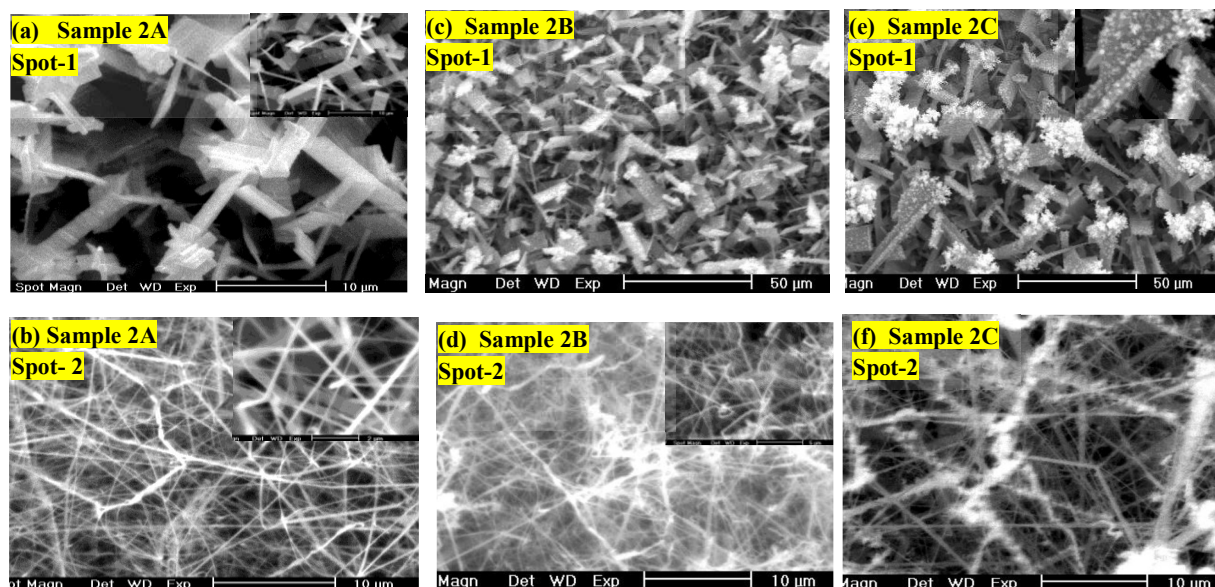


Figure 4.4. (a-f) The SEM images of β -Ga₂O₃ nanostructures grown on sample 2A, 2B and 2C. In the spot-1 region thick structures (plates, rods etc. in the micron range) are seen which was just above the source material whereas nanostructures are observed away from the source region in the spot-2 region.

On analyzing in details, it has been found that the deposition of gallium oxide particulates increases at spot-1 on the as grown β -Ga₂O₃ structures as the growth temperature increases from sample 2A to 2C. The morphology of the structures remains same (plate like); the only change is increase in the density of surface particulates. Spot-1 was just above the source material and material is directly deposited on the as grown gallium oxide structures. Similarly in spot-2, increased density of surface particulates are observed with increase in the growth temperature.

Figure 4.5 shows the SEM images of the samples grown by vapor transport method (sample 3A and 3B). The only difference between the two samples was the carrier gas used during deposition. Dry N₂ was used in sample 3A whereas moist N₂ (N₂ was flower through water, details are shown in Fig.1). Figure 4.5(a) shows the SEM images of sample 3A where an extensive growth of β -Ga₂O₃ nanowires is observed. The

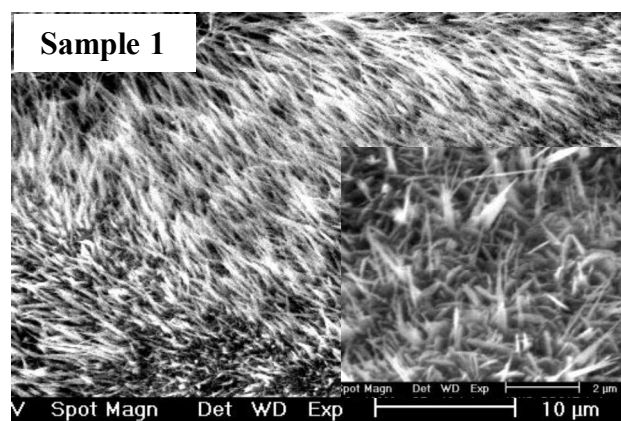


Figure 4.3. SEM image of β -Ga₂O₃ nanostructures grown on sample 1

Figure 4.3 shows SEM image of as grown product on the GaAs substrate (sample 1). The nanowires are found to have diameter between 60–200 nm and length up to a few microns. The nanobelts have width of several hundred nanometers and thickness of few tens of nanometers. The nanowires have side growth features at the bottom. This structural feature is possibly due to surplus gallium vapor, which directly deposits as gallium oxide layers on the surface of pre-formed β -Ga₂O₃ nanowires through an epitaxial growth mechanism [89].

Figure 4.4 shows SEM images of the samples grown by thermal evaporation method (samples 2A, 2B and 2C). For each of the samples, SEM data is shown for two spots 1 and 2. Spot-1 was located just above the source material and spot-2 was located around 8 mm away from the source. It may also be noted that in each sample, spot-1 and 2 have the same temperatures, the only difference being the amount of the incoming reactant flux as a result of distance from the source. Sample 2A was grown at 925°C and has two types of the structures. At spot-1, which was just above the source material, thick structures (plates, rods etc. in the micron range) are found (fig. 4.4 (a)). β -Ga₂O₃ nanostructures are observed at the spot-2 (fig.4.4 (b)). The nanowires are found to have diameter in the range of 50-200 nm and length up to a few hundred microns. Similar

Table I: Detail of the parameters used for growth of β -Ga₂O₃ Nanostructures

Sample	Source material	Carrier gas	Substrate	Growth method	Growth temperature
1.	Ga metal from GaAs material	Dry Nitrogen (99.999% pure)	Gold coated GaAs wafer	Thermal annealing	950 °C
2A.	Ga metal + Ga ₂ O ₃ powder	Dry Nitrogen (99.999% pure)	Gold coated Si wafer	Thermal evaporation	925 °C
2B.	Ga metal + Ga ₂ O ₃ powder	Dry Nitrogen (99.999% pure)	Gold coated Si wafer	Thermal evaporation	950 °C
2C.	Ga metal + Ga ₂ O ₃ powder	Dry Nitrogen (99.999% pure)	Gold coated Si wafer	Thermal evaporation	980 °C
3A.	Ga metal	Dry Nitrogen (99.999% pure)	Gold coated Si wafer	Vapor transport	900 °C
3B.	Ga metal	Moist Nitrogen (99.999% pure)	Gold coated Si wafer	Vapor transport	900 °C

4.3 Structural characterization and growth mechanism

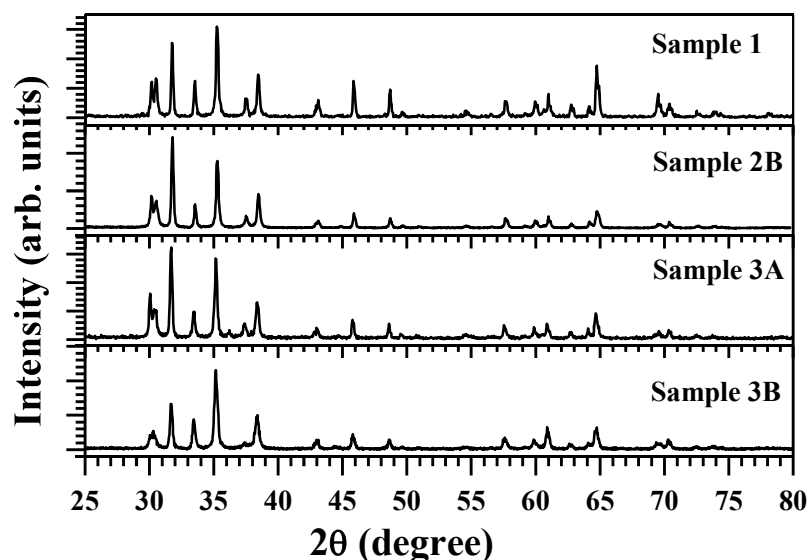


Figure 4.2. The GIXRD pattern of as synthesized β -Ga₂O₃ nanostructures for sample 1, sample 2B, sample 3A and sample 3B.

Figure 4.2 shows a typical GIXRD pattern of the β -Ga₂O₃ nanostructures deposited on the samples 1A, 2B, 3A and 3B. All the XRD peaks were indexed to the monoclinic structure with the lattice constants $a=1.223$ nm, $b=0.304$ nm, $c=0.580$ nm, $\beta=103.7^\circ$ (JCPDS card no. 76-0573) thereby confirming the formation of single phase β -Ga₂O₃. The XRD does not show any change in the crystal structure for all the cases.

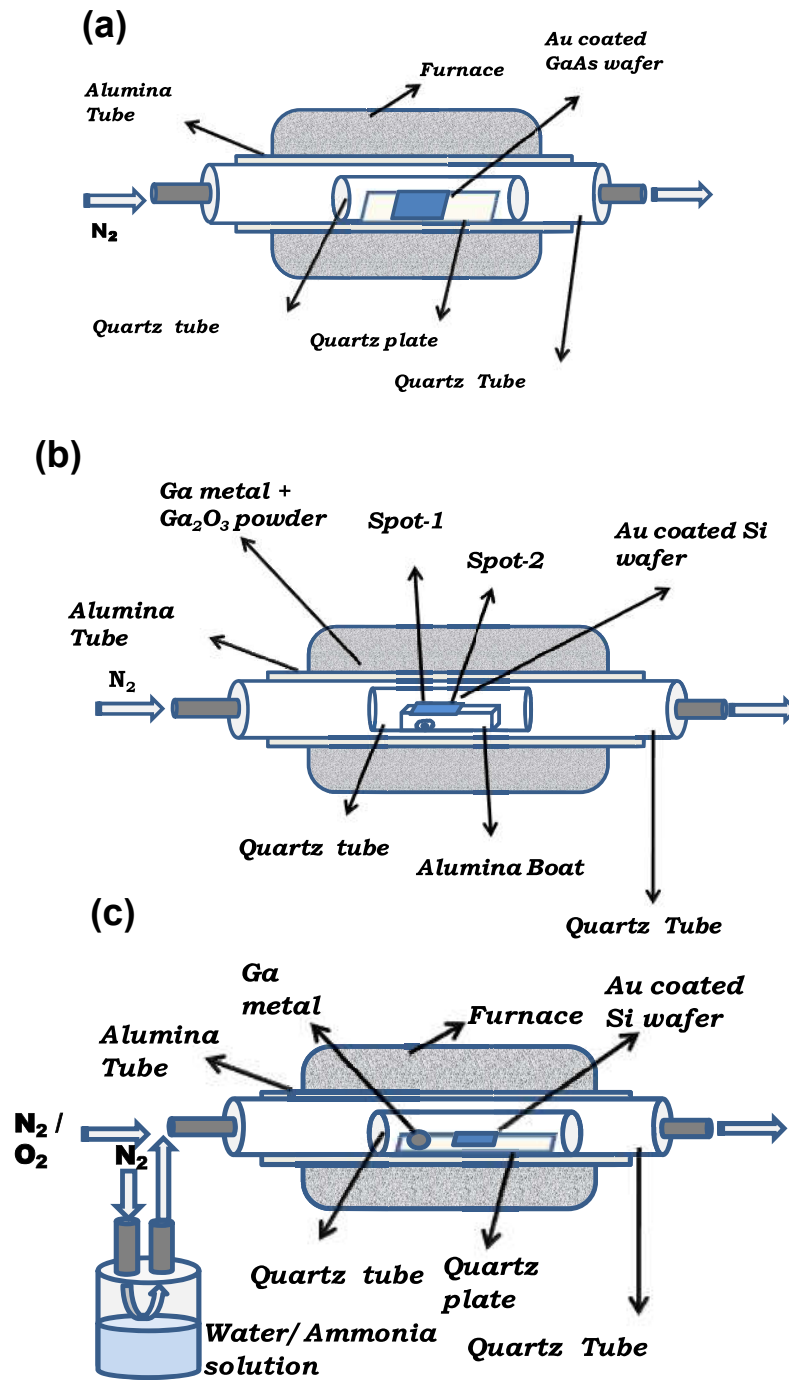


Figure 4.1. Schematic of the growth process for (a) sample 1, (b) samples 2A, 2B, 2C and (c) samples 3A, 3B and 3C.

4.2 Experimental procedure

Three growth methods were used to grow the β -Ga₂O₃ nanostructures. In the first growth method (thermal annealing process), GaAs wafer with 20 nm gold coating was used as the substrate. This gold coated GaAs substrate was put inside the horizontal quartz tube furnace (as shown in the fig. 4.1 (a)) and furnace temperature was ramped to 950°C. The growth period was three hours. This sample is denoted as sample 1. In the second method, β -Ga₂O₃ nanostructures were synthesized by thermal evaporation method. Ga metal and Ga₂O₃ powder were used as the source material and samples were put above the source material as shown in the fig. 4.1(b). The Si (100) wafer (15 mm X 15 mm) was coated with about 10-20 nm of gold film by thermal evaporation at 10⁻⁶ Torr and used as the substrate. Three samples were grown at 925°C, 950°C and 980°C for one hour and denoted as sample 2A, sample 2B and sample 2C respectively.

In the third method (Figure 4.1(c)), β -Ga₂O₃ nanostructures were synthesized by vapor transport method (also discussed in chapter 3) at 900°C for one hour. This sample is denoted as sample 3A. In the second sample 3B, the N₂ gas saturated with water vapor was used as the carrier gas, keeping all the other parameters same as sample 3A. Water vapor saturated N₂ gas was obtained by bubble the N₂ gas through a water container. In all the three cases, the growth was carried out at atmospheric pressure. The details of all the samples are summarized in the table 1.

Chapter 4

Study of different growth techniques and optimization of the growth parameters

4.1 Motivation of the work

An understanding of the mechanism of PL and the influence of ambient oxygen on the PL properties has been discussed in chapter 3. These results provide a route for room-temperature sensing of O₂ by β -Ga₂O₃ nanostructures. From the previous results, it is also clear that in β -Ga₂O₃ nanostructures, intensity of UV band is more prone to surface state trapping centers as compared to visible luminescence [83-84]. This is because, the photo excited electrons which give the UV luminescence, are in the conduction band and mobile. Hence, they get trapped at the surface states. In contrast to this, in visible luminescence both the electrons and holes are trapped in the donor and acceptor levels respectively and hence are less prone to be affected by surface trapping centers [83-84].

Having established that a close relationship between the presence of surface states and the intensity of the UV luminescence exist in β -Ga₂O₃, in this chapter, we have mainly concentrated on analyzing the PL data from these nanostructures synthesized by different techniques. The techniques, used to grow the nanostructures, have a significant influence on the optical sensing properties. Hence, a comparative study of different growth techniques like thermal annealing [85], thermal evaporation [86-88] and Vapor transport method [83-84] have been carried out to study the growth parameters that affect the optical properties of β -Ga₂O₃ nanostructures. The dependence of the PL properties as a function of deposition conditions and synthesis techniques are analyzed to optimize the growth process. The effect of the surface defects on the PL intensity response to O₂ concentration has also been studied.

reduces in all the cases. Sample C and sample D is annealed the moist environments and the surface of the nanostructures is dominated by the permanent surface defects. Surface defects which are created (permanently) due to annealing in moist environments on the surface of the nanostructures, leave only a small surface area for the O₂ adsorption/desorption. Hence, the PL intensity variations with the O₂ concentration reduce.

5.6 Summary

We have studied the effect of annealing in different atmosphere on the structural and optical properties of the β -Ga₂O₃ nanostructures. The PL spectra show that annealing of β -Ga₂O₃ nanostructures in different atmospheres produce defects on the surface of the nanostructures, which alters the PL of these nanostructures. Further the effects of the different atmospheres are nonrecoverable. In the presence of water, at high temperature adsorption of water dominates over the effect of other gases, which indicates that sensitivity at high operating temperature and the life of devices will be significantly affected in presence of water vapor. Further, these permanent defects on the surface of the nanostructures leave a small surface area for the O₂ adsorption/desorption and hence reduce the PL intensity variation with the O₂ concentration. These results can be helpful for exploring the possibility of use of β -Ga₂O₃ nanostructure as sensors working in the moist environments and high temperatures.

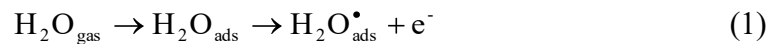
it is observed that this effect on the β -Ga₂O₃ nanostructure surface is not changed in the course of many repetitive PL (up to one year) experiments i.e. the effect (or bonding of water molecules) is permanent. Due to the formation of such chemical bonding on the H₂O exposure, the PL intensity never recover to the intensity level of sample A and B.

Sample D was annealed in ammonia solution (35% ammonia in water). It has been reported that the PL intensity increases significantly upon annealing in a reducing atmosphere [93]. Ammonia acts as a reducing agent for the gallium oxide [49], so as reported previously, the PL intensity should increase. But in our case the PL shows similar characteristics as observed in the sample C. It indicates that in the presence of water, the affect of ammonia is suppressed. Various results indicate that, when water is present with other gasses simultaneously, water competes with the other gases for reaction with the oxygen vacancy sites and impact the absorption of the other gases. Further, water induced surface structural changes have also been observed in literature [94-95]. In the case of sample D, where ammonia solution (moist ammonia) is used, the effect of water dominates and corresponding PL intensity and UV to visible luminescence intensity ratio decreases similar to sample C.

The third observation can also be understood using this model. It has been explained in chapter 3 that the intensity of photoluminescence from the β -Ga₂O₃ nanostructures in O₂ gas ambience is correlated with the O₂ pressure through the Langmuir equation. The nanostructures have oxygen sensing properties due to formation of oxygen deficiency related trap levels at the surface which are strongly related to the volume of the adsorbed of O₂ atoms on the surface. At low O₂ pressures, these surface states are formed due to O₂-desorption from the surface of nanostructure. UV and Visible luminescence bands are prone to these surface state trapping centers because the conduction electrons trap there and recombine non-radiatively. Hence the PL intensity

5.5 Discussion on the changes observed in the PL properties

To understand the observations made from the PL measurements, we use the extended model of Binet and Gourier for the β -Ga₂O₃ nanostructures discussed in the **chapter 3**. The effect of the annealing in the O₂ ambient has already been discussed above. In sample C, the total PL intensity reduces with the drastic change in the ratio of UV to visible luminescence intensities. In chapter 4, it has been shown that defects present on the surface of the nanostructures change the UV to visible luminescence intensity ratio along with the total PL intensity. This has been attributed to the more sensitivity of the UV luminescence mechanism towards the surface defects as compared to the visible luminescence. This indicates that surface defects create in sample C due to annealing in the moist ambient. The justification of change in the ratio of UV to visible luminescence intensity using band model, also strengthen the explanation of surface defects reported in the literature for the moist ambient annealing. It has been reported that water vapor reacts with the metal oxides in the two ways. At low temperatures, water is adsorbed in its molecular form according to the equation (1):



At high temperatures (780°C and above), the adsorption of OH group dominates according to the following equation:[90]



In sample C which was annealed at 800°C, the dominating mechanism is adsorption of the OH⁻ groups according to equations 2(a,b). Reaction of the OH⁻ group at the surface of the nanostructures which is primarily expected to be GaO_x, creates surface states, which quench the PL by creating competitive nonradiative paths. Apart from this,

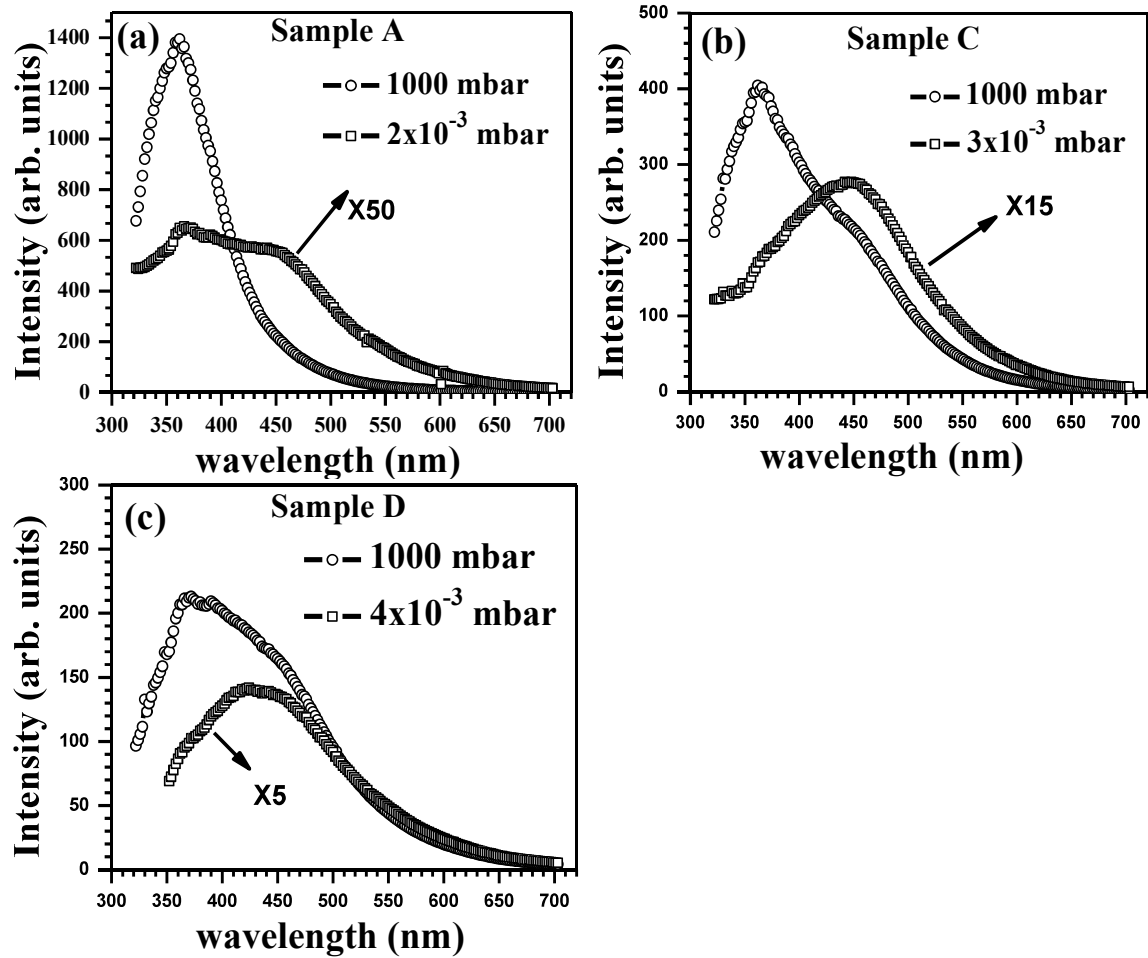


Figure 5.6. (a-c) Room temperature PL spectrum of β - Ga_2O_3 nanostructure sample A, C and D at different O_2 pressure conditions

O_2 partial pressure dependent room temperature PL measurements have also been done for sample A, sample C and sample D which are shown in the fig. 5.6. The PL intensity reduces in all the samples as the O_2 concentration reduces. The reduction in the PL intensity is less in the sample C and sample D as compared to the sample A (shown in the fig. 5.6 (a-c)). From the PL studies, three observations have been made, first: total PL intensity reduces in all the annealing processes, second: the intensity ratio of UV to visible luminescence change significantly in the sample C and sample D and third: O_2 partial pressure dependent PL behavior decrease in sample C and sample D significantly.

luminescence are closely related to the concentration of O^{-2} vacancies in the bulk and so their intensity decreases after annealing in O_2 atmosphere [91] in comparison with sample A. In case of sample C and sample D, the intensity of UV-visible luminescence decreases drastically as compared to sample B.

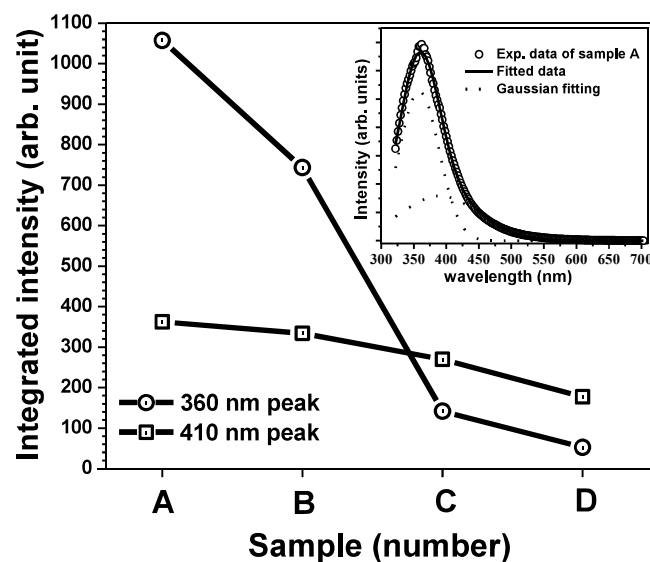


Figure 5.5. Integrated intensity plot of peak 360 nm and 410 nm for the sample A, B, C and D. Inset shows the fitting of two Gaussian peak for the PL data of sample A.

Figure 5.5 show the integrated intensity plot of PL spectra for the sample A, B, C and D. In all samples the PL spectra are fitted by two Gaussians, peaked at 360 nm and 410 nm. The peak at around 410 nm is associated with the recombination of a trapped electron in a donor with a trapped hole in an acceptor [92]. From fig. 5.5, it can be clearly seen that in case of sample B the integrated intensity of both peaks decrease about 1.2-1.3 times. But in case of sample C and D, the integrated intensity decreases about 1.5 times for peak at 410 nm and 10 times for peak at 360 nm. The integrated intensity for peak 360 nm is decreases more than the peak at 410 nm.

to a few hundred microns. The Transmission Electron Microscopy (TEM) and Energy dispersive X-ray spectroscopy (EDS) results have been shown in chapter 3. It showed that the wires contained gold at their tips which indicates the Vapor-Liquid-Solid (VLS) growth mechanism for β -Ga₂O₃ nanowires.

5.4 Effect of annealing on the PL Properties

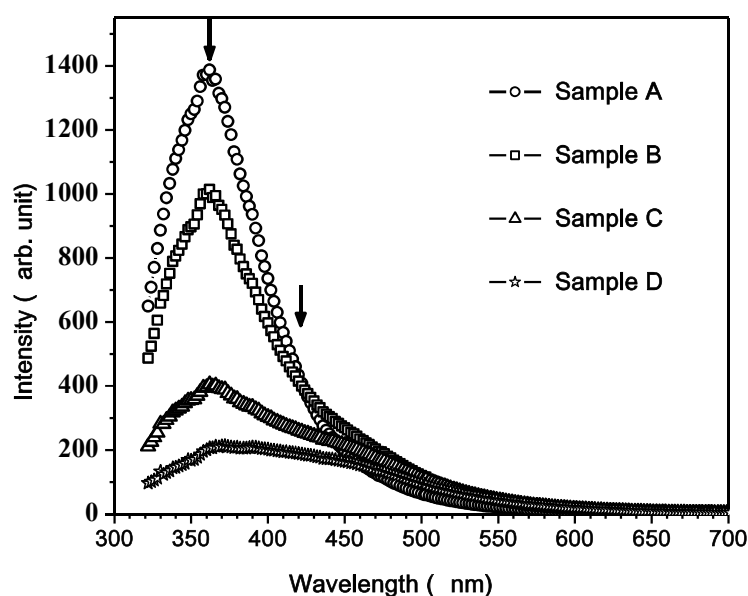


Figure 5.4. Room temperature PL spectrum of β -Ga₂O₃ nanostructure sample A, B, C and D which shows that PL intensity is sensitive to the annealing in different environments.

Figure 5.4 shows the room temperature PL spectra of β -Ga₂O₃ nanostructures (samples A, B, C and D). It can be observed that a broad UV-visible emission peak centered on 360 nm is present in all the samples and is independent of the sample's process parameters. This is in good agreement with the Binet and Gourier's results [77] (but slightly blue shifted, possibly due to the formation of nanostructures), where this has been attributed to self trapped excitons. The intensity of 360 nm peak decreases in sample B, sample C and sample D respectively.

In sample B, the photoluminescence intensity decreases with respect to sample A, but the shape of the spectra does not change significantly. The UV and visible

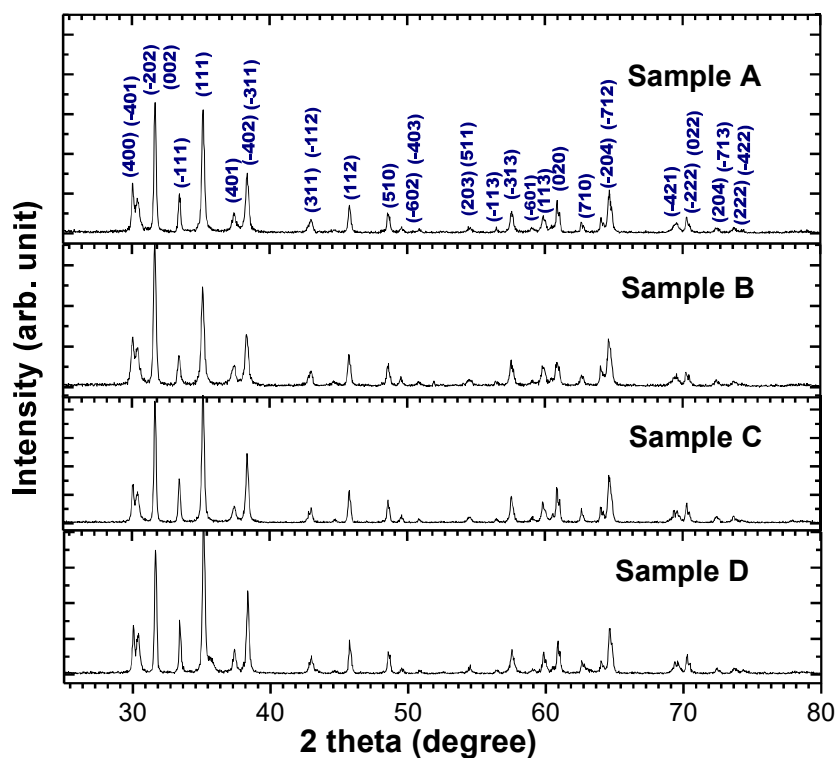


Figure 5.2. The GIXRD pattern of as synthesized β -Ga₂O₃ nanostructures, in sample A, sample B, sample C and sample D.

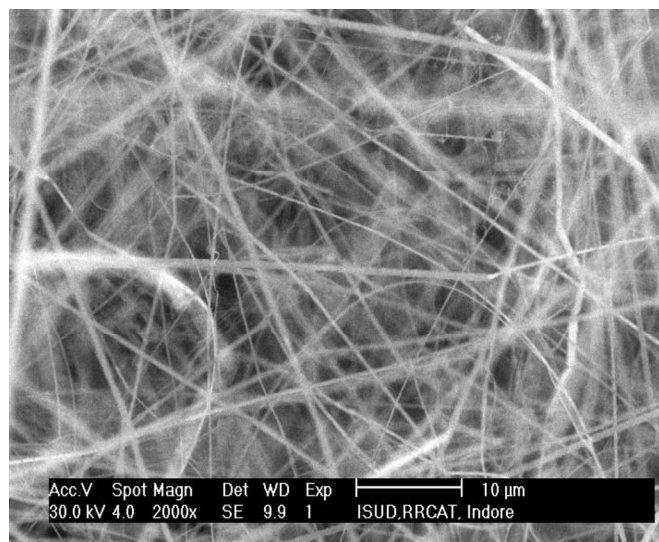


Figure 5.3 The SEM images of β -Ga₂O₃ nanostructures grown on sample A. There is an extensive growth of nanowires which have diameter of around 40-100 nm and length up to a few hundred microns.

Figure 5.3 shows the SEM images of the as synthesized β -Ga₂O₃ nanowires and nano belts grown on Si substrate. Figure 5.3 shows that there is an extensive growth of nanowires. The nanowires are found to have diameter between 40-100 nm and length up

for 30 minutes. This was done by flowing 0.5 lpm N_2 through a water filled beaker (as shown in fig.5.1). As the N_2 gas flows through the beaker, it gets saturated with water vapor. This sample is denoted as sample C. Similar to water vapor; the fourth piece was annealed in ammonia solution vapor (35% NH_3 in water) at $800^\circ C$ for 30 minutes and is denoted as sample D.

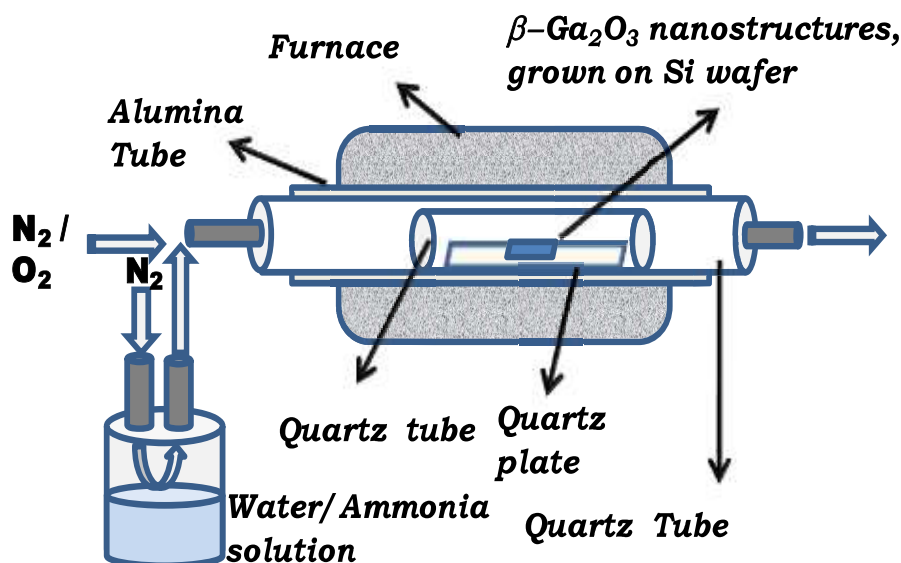


Figure. 5.1. A schematic illustration of the experimental setup for annealing of $\beta\text{-Ga}_2\text{O}_3$ nanostructures.

5.3 XRD and SEM results

Figure 5.2 shows typical GIXRD pattern of the $\beta\text{-Ga}_2\text{O}_3$ nanostructures deposited on Si substrates for samples A, B, C and D. All the diffraction peaks in the pattern are indexed to $\beta\text{-Ga}_2\text{O}_3$ with monoclinic structure. They are in good agreement with the lattice constants $a=1.223$ nm, $b=0.304$ nm, $c=0.580$ nm, $\beta=103.7^\circ$ (JCPDS card no. 76-0573). All the XRD peaks have been indexed to the above structure thereby confirming the formation of single phase $\beta\text{-Ga}_2\text{O}_3$. From Fig. 5.2 it is also confirmed that the crystal structure of these samples do not change due to annealing in different atmospheres.

Chapter 5

Effect of post growth annealing of β -Ga₂O₃ nanostructures in different environments on the photoluminescence properties

5.1 Introduction and background

β -Ga₂O₃ is one of the most suitable materials for high temperature gas sensing, due to its high melting point and stable structure. Since nanostructure have large surface to volume ratio, it may be also possible that there is a permanent effect on the performance of the device at high temperature due to chemical reaction with surrounding gases. This has been characterized by comparing the intensity of the UV and visible luminescence. Hence, in this chapter, results of the effects of annealing at high temperature in different atmosphere (namely oxygen, water vapor and moist ammonia) on the structural and optical properties of the β -Ga₂O₃ nanostructures have been reported. The effects of annealing in different environments on the PL response to the O₂ concentration have also been discussed. This study explores the issues that affect the applicability of this system in moist high temperature environments.

5.2 Experimental procedure

The Gallium oxide nanostructures were synthesized by vapor transport method discussed in **chapter 3**. The Si substrate, on which β -Ga₂O₃ nanostructures were deposited, was divided in four parts. One piece was retained as untreated and denoted as sample A. The second piece was annealed at 800°C in O₂ at a flow of 0.5 lpm for 30 minutes and denoted as sample B. The third piece was annealed in water vapor at 800°C

In_2O_3 is primarily due to deep donor-acceptor recombination and hence insensitive to changes at the surface.

7.7 Summary

In summary, we report the fabrication of high quality In_2O_3 wire structures with hexagonal and square cross-section using vapor transport method on gold coated Si (100) substrates in the temperature range of 875-925°C. We have grown very long (greater than 100 micron) hexagonal cross section In_2O_3 microwires. It has been observed that by changing the growth parameters (growth temperature and distance from the source), the cross-section of the In_2O_3 wire changes from hexagonal to square with the change of their growth direction from $\langle 111 \rangle$ to $\langle 100 \rangle$. The variation in the growth morphology and shape have been analyzed and explained. These results indicate a way to grow In_2O_3 microwires / nanowires of the desired cross-section by varying the growth parameters. The PL spectra of In_2O_3 micro/nanostructures exhibit orange-yellow emission bands. From the PL results, it is concluded that the growth temperature is not the only parameter, but the morphology of the grown products is also important, which influence the PL transition energy of In_2O_3 . These nanostructures are found to be insensitive for the adsorption/desorption of the O_2 gas and hence unsuitable for applications to PL based sensors.

oxygen deficiency. In this work, due to high growth temperature, oxygen vacancies generate because of incomplete oxidation. These oxygen vacancies act as deep defect donors and these results in the formation of defect levels in the band gap. The emission thus results from the radiative recombination of a photo-generated hole with an electron that belongs to ionized oxygen vacancies.

In our case, it is observed that the PL transition energy is same for the sample A1, B1 and C1, irrespective of their growth temperature (shown in fig. 7.12(a)). Apart from this, in samples B2 and C2, the growth morphology changes from microwire to nanosheet and nanowire, with the decrease in the growth temperature. This leads to another PL band at 430 nm with the PL band centered at 610 nm (shown in fig. 7.12(b)). Similarly, the morphology of the structures in samples A1, B2 and B1, C2 are different despite their same growth temperatures. This also leads to difference in their PL spectra. It has been reported that the transition energy gets red shifted with increase in the growth temperature [146] which is contrary to our observed results. From these results, it is concluded that the growth temperature is not the only parameter that influences the optical transition energy of the In_2O_3 , the morphology of the grown products also modifies the transition energy.

A comparison of In_2O_3 nanostructures with the isoelectronic $\beta\text{-Ga}_2\text{O}_3$ nanowire system have been made by studying the dependence of PL intensity on the environmental oxygen partial pressure (similar to the ones carried out for $\beta\text{-Ga}_2\text{O}_3$ nanostructures). No significant sensitivity to oxygen exposure was observed. Since the PL originates from deep donor to acceptor pair (DAP) transition in In_2O_3 , the carriers (electrons and holes) are localized in the donor and acceptor sites. This localization makes the carriers (PL intensity) insensitive to the changes on the surface of the nanostructure. Thus, the results reveal that unlike $\beta\text{-Ga}_2\text{O}_3$, where a significant component of the PL intensity arises due to electrons in conduction band recombining via self trapped excitons, the PL intensity in

direction to the energetically favorable orientation. The diameter of the In_2O_3 wires at the tip region is in the range of microns (0.8-2 μm) in sample A1 and in the range of nanometers (40-200 nm) in sample C3. For the large diameter wire, the second term in the eqns. (7), (8) dominate. The surface energy of the (111) surface is lower than the surface energy of the (100) surface and hence to minimize the total surface energy the microwire grow in $\langle 111 \rangle$ direction. As the diameter of the wires reduce, the first term in the eqns. (7), (8) also becomes important. Since, the surface energy of the (100) surface is lower than the surface energy of the (110) surface, the growth direction changes from $\langle 111 \rangle$ to $\langle 100 \rangle$ to minimize the total surface energy.

7.6 PL results

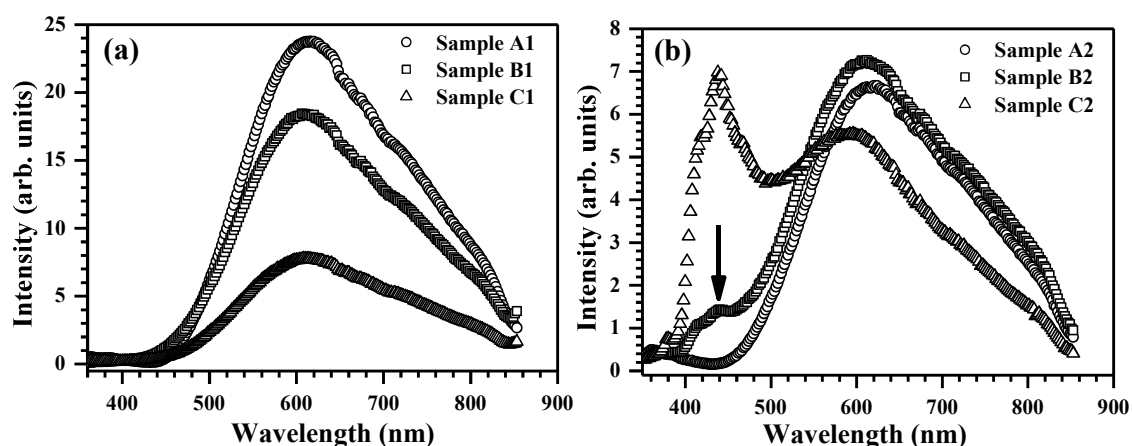
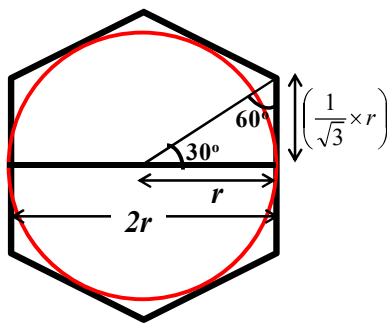


Figure 7.12. (a) Room temperature PL spectra of In_2O_3 nano/microstructure samples A1, B1 and C1; (b) room temperature PL spectra of In_2O_3 nano/micro structure samples A2, B2 and C2.

The results of the PL measurement on In_2O_3 nanostructures, prepared by different growth conditions, are shown in fig.7.12. Previous reports have demonstrated room temperature PL in nanoscale In_2O_3 centred at 480 nm and at 520 nm from In_2O_3 nanoparticles [141], 470 nm from In_2O_3 nano-fibers [142], 637 nm from the In_2O_3 films [143], and 426 nm and 398 nm for In_2O_3 nanowires [144, 145]. We have observed a broad PL centred at 610 nm in all samples. PL emission is considered as an effect of the

where surface energy for the three low index planes of indium oxide are related as follows; $\gamma\{111\} < \gamma\{100\} < \gamma\{110\}$ [140].

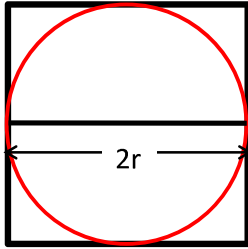


For hexagonal cross section wire with width = $2r$ and length = L : -

$$\begin{aligned} \text{Crosssection area} &= 12 \times \left(\frac{1}{2} \times r \times (r \times \tan(30)) \right) = 12 \times \left(\frac{1}{2} \times r \times r \times \left(\frac{1}{\sqrt{3}} \right) \right) \\ &= 2\sqrt{3} \times r^2 \end{aligned}$$

$$\text{Six side surface (along the length of wire) area} = 6 \times \left(\frac{2}{\sqrt{3}} \times r \right) \times L$$

$$\text{Volume} = \text{cross section area} \times \text{length} = 2\sqrt{3} \times r^2 \times L$$



For square cross section wire with width = $2r$ and length = L : -

$$\text{Crosssection area} = (2 \times r) \times (2 \times r) = 4 \times r^2$$

$$\text{Four side surface (along the length of wire) area} = 4 \times (2 \times r) \times L$$

$$\text{Volume} = \text{crosssection area} \times \text{length} = 4 \times r^2 \times L$$

Figure 7.11. Schematic pictures of hexagonal and square cross section wires and area calculations for the different faces. For the comparison with the cylindrical wire, dimensions are taken in the form of diameter ($2r$) and length (L). In the both hexagonal and square cross section wires, length of apothem is taken as r .

In the hexagonal cross section wire, six long side surfaces are set of (110) planes. In the square cross section wires, four long side surfaces are set of (100) planes. The wire structures grow on the In_2O_3 film which initially grows on the Si substrate and gold only acts as an initial nucleation centre for the growth. Hence γ_{ss} can be ignored for the sake of simplification. The width of LS zone (L_C) is important. Within this zone, change of the micro/nanowire growth direction is triggered in order to favor a lower energy state [62]. For samples A1 and C3, the growth temperature is same and hence the L_C is fixed for both these samples. In such a case, the diameter of the wire is critical. If the diameter of the wire is large, the contribution of the two interfaces in the total system energy will be dominant whereas in nanowires, within the critical thickness, the contribution from the side surfaces will be relatively large. This triggers the transition of nanowire growth

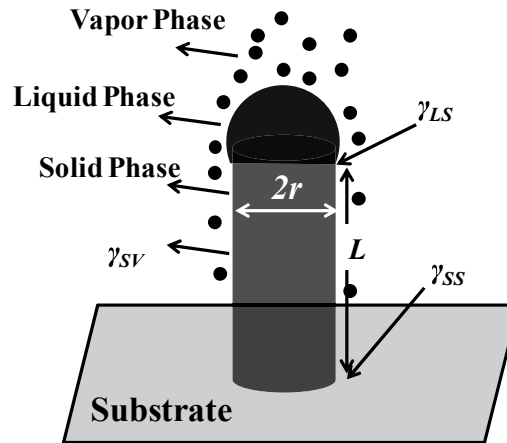


Figure 7.10. Schematic pictures of circular cross section wires showing with different surface/interface energies.

The behavior of change in the growth direction can be understood in terms of surface/interface energy. For cylindrical micro/nanowire with radius r and length L , the total surface/interface energy F is expressed as [62];

$$F = (2 \times \pi \times r \times L) \times \gamma_{SV} + (\pi \times r^2) \times \gamma_{LS} + (\pi \times r^2) \times \gamma_{SS}$$

and the surface/interface energy per unit volume f is expressed as;

$$f = \frac{F}{(\pi \times r^2 \times L)} = \frac{2 \times \gamma_{SV}}{r} + \frac{\gamma_{LS}}{L} + \frac{\gamma_{SS}}{L} \quad (6)$$

where γ_{sv} is the solid–vapor interface energy (cylindrical side surface), and γ_{ls} is the LS (Liquid-Solid) interface energy (circular cross section surface) between Au-In or In catalyst and In_2O_3 . γ_{ss} is the interface energy (circular cross section surface) between In_2O_3 and the silicon substrate. Similar to cylindrical wires, the surface/interface energy per volume f , for $\langle 111 \rangle$ direction and $\langle 100 \rangle$ direction growth of In_2O_3 , can also be expressed as

$$f_{\langle 111 \rangle} = \frac{2 \times \gamma_{(110)}}{r} + \frac{\gamma_{(111)}}{L} \quad (7)$$

$$f_{\langle 100 \rangle} = \frac{2 \times \gamma_{(100)}}{r} + \frac{\gamma_{(001)}}{L} \quad (8)$$

cross section as shown in the fig. 7.9(a). Figures 7.9(b) and (c) show a defect-free electron diffraction pattern and high resolution image of the In_2O_3 nanowire with an inter-atomic spacing of 4.9 \AA , which corresponds to the (200) lattice planes. The selected area electron diffraction (SAED) pattern of this nanowire is indexed to the [100] zone axis. The TEM results indicate the growth direction of the nanowire in $\langle 001 \rangle$ direction. Figure 7.9(d) shows SEM picture of the hexagonal cross section microwire of sample A1. From the top, it can be seen that wire has a horizontal triangular top surface surrounded by three pentagon shaped surfaces. Since the In_2O_3 is a cubic system, the top surface should be (111). From the symmetry of cubic system, the three surrounding side-surfaces are (100), (010) and (001). This is indicated in the inset of fig. 7.9(d). These observations indicate that the growth directions of In_2O_3 microwires are $\langle 111 \rangle$.

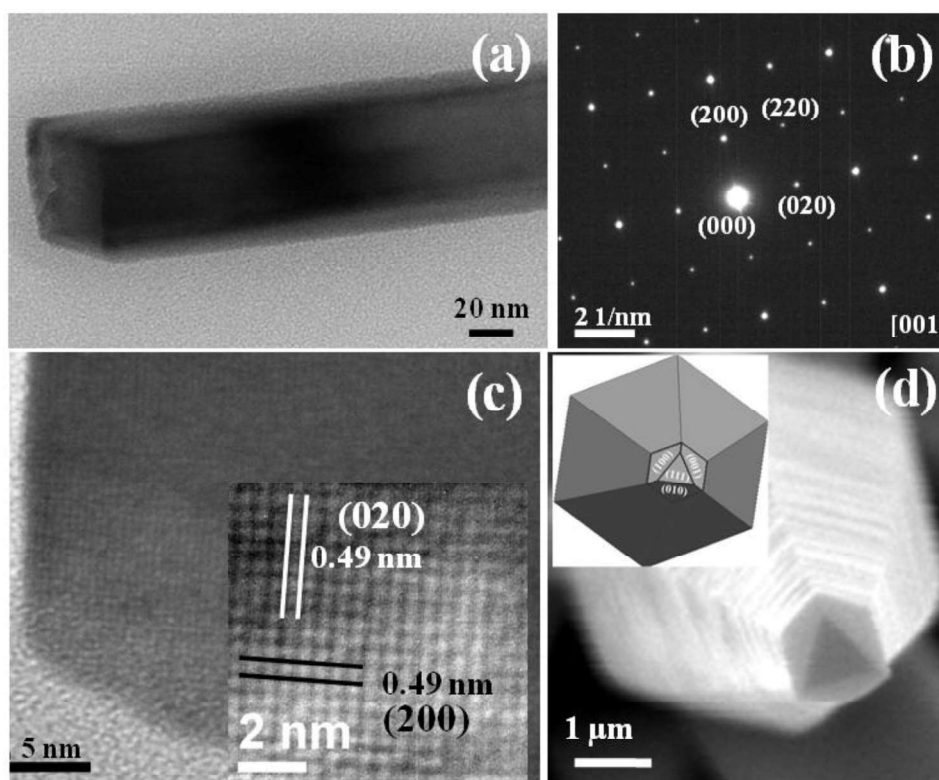


Figure 7.9. (a-c) shows TEM, SAED and HRTEM images of the In_2O_3 nanowire of sample C3. The nanowire is 45 nm in diameter with lattice spacing 0.49 nm which corresponds to the (200) plane, SAED pattern is indexed to [100]; (d) The SEM picture of hexagonal cross section micro wire with the (111) top surface.

than or equal to 850°C, no growth of In₂O₃ micro/nanostructures was observed; they have only In₂O₃ film-like structures.

In the second case, growth temperature (~875°C) is same for samples A1, B2, and C3 and only the distances from the source changes. From eqn. (5), the concentration of the reactant species at the substrate surface decreases with the distance from the source. Therefore, sample C3 receives less vapor concentration (incoming flux) in comparison to the samples B2 and A1. The reduction in the incoming flux leads to reduction in the available flux per nucleation site. Thus the diameter of the In₂O₃ wire changes from micron size to nanometer [134, 135]. Similar to samples A1 and C3, samples B1 and C2 have same growth temperature (~ 900°C) while the distances from the source are different (10 mm and 50 mm respectively). It is clear from the figs. 7.5(a) and 7.6(b) of sample B1 and sample C2 respectively that the diameters of In₂O₃ wires reduce, as the distance from the source increase similar to sample C3. But the branched In₂O₃ wire structures have been observed instead of In₂O₃ nanowires observed in sample C3. This is possibly because of different growth conditions (growth temperature and concentration of reactants) [131, 132]. These branched structures are observed due to a spontaneous branch formation [136], or self catalyst branch growth [137-139].

7.5 Discussion on the TEM Results and growth orientation of In₂O₃ micro/nanowires

From the SEM results, it has been concluded that the diameter of In₂O₃ wire reduces from micrometers to nanometers in sample A1 and sample C3 respectively. On analyzing in details using SEM and TEM, we have observed that their growth directions are also different. Figure 7.9(a) shows a TEM image of a single In₂O₃ nanowire (of sample C3) that is 45 nm in diameter. The nanowire is straight and smooth with square

observed a reduction in the length of the In_2O_3 wires in the sample B1 and C1. We have observed two phenomena in the sample C1. First, the side growth increases (shown in the inset of fig. 7.6(a)). Second, the In_2O_3 wire has a square cross section which can be seen in the fig. 7.6(a). Hence the cross section (growth directions) of the In_2O_3 microwire changes with the growth temperature. Due to the side growth and change in the cross-section, the growth rate along the length of the In_2O_3 wire slows down and consequently the length becomes short. In the case of samples A2, B2 and C2, all were kept at a distance of 50 mm from the source and have growth temperatures 25°C less as compared to samples A1, B1 and C1 respectively. Hence the resultant flux reaching the substrates reduces as compared to the set (A1, B1 and C1) due to the term $x^{1/2}$ in the denominator and $T^{3/2}$ in the numerator in eqn. (5). This leads to the observation of different kind of structures in these samples as compared to sample A1, B1 and C1. If we compare samples A2, B2 and C2 which have growth temperature 850°C , 875°C and 900°C respectively, the concentration of the reactant species at the surface increases as temperature increases due to the temperature term in eqn. (5). Hence the morphology of the samples A2, B2 and C2 changes from the film-like structure to nanostructures with sheet-like growth and branched structures respectively, as shown in figs. 7.4(b), 7.5(b) and 7.6(b) respectively. The local growth temperature along with the concentration of reactants greatly affects the formation of the branched structure and this leads to branched structures in the high temperature region whereas In_2O_3 nanobelts/nanosheets are found in the lower temperature region [131-133]. In the third set (sample A3, B3 and C3), In_2O_3 nanostructures are observed in sample C3 only. This result indicates that the growth temperature should be higher than a particular temperature (in our case 850°C) to activate the nanostructure growth. Since the growth temperature of sample A2, A3 and B3 are less

component is In_2O . As the In_2O vapor transports downstream to the substrate, it captures by the catalytic droplets on the substrate and decomposes to liquid indium and solid In_2O_3 . In our study, the source temperatures range from 875°C to 925°C . This temperature range is significantly below the indium boiling point of 2072°C and hence the concentration of indium vapor in all the three cases is expected to be the same. Thus primary evaporating species is In_2O , whose boiling point ($\sim 527^\circ\text{C}$) is much below the source temperature. Further, in all these cases, the pressure of the chamber, which defines the concentration of the O_2 gas, is kept constant at 20 mbar. Hence, the concentration of In_2O is not expected to vary in this temperature range, as it mainly depends on the O_2 concentration in the growth chamber which is kept constant. Under these circumstances, it is assumed that the initial concentration of In_2O over the source is nearly same in the all three source temperatures.

The transport flux of these reactant species (In_2O) to the substrate can be defined as [130]

$$J = h_g \Delta C \quad (5a)$$

$$\propto \frac{T^{3/2}}{x^{1/2}} \quad (5b)$$

where gas phase mass transfer coefficient $h_g = D/\delta(x)$; $\delta(x)$ defines the thickness of the boundary layer which is proportional to $x^{1/2}$, D is diffusion coefficient which is proportional to $T^{3/2}$ and $\Delta C = C_g - C_s$; C_g defines concentration of the reactant species in the gas phase (or at the boundary layer) and C_s defines the concentration of the reactant species at the surface.

Using equation (5), we can explain the observed SEM results. In the first case, the temperature is in increasing order from sample A1 to C1. All the three samples A1, B1 and C1 were close to the source material at the same distance. As the growth temperature increases, J increases in samples B1 and C1 as compared to A1. However, we have also

increases keeping the substrate temperature constant; this contains two set of samples 1) samples A1, B2 and C3, and 2) samples B1 and C2.

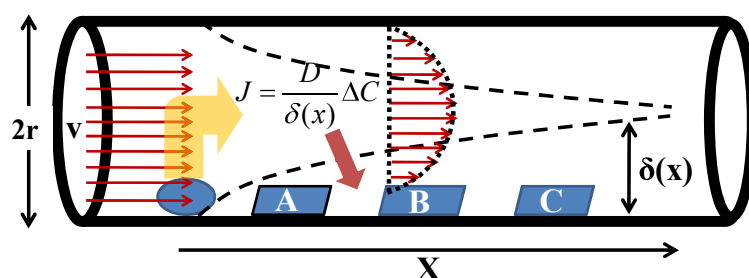
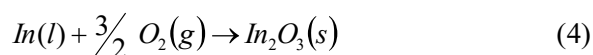
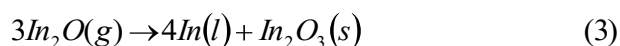
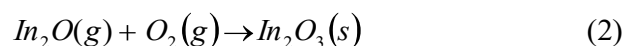
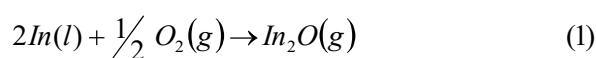


Figure 7.8. The schematic of the chemical vapor deposition process and boundary layer thickness profile for the furnace. The source and substrate positions are also indicated.

To understand and explain the observed results, we model the reactor geometry by a hot wall chemical vapor deposition (CVD) system. The samples are placed on the quartz tube at a distance from the source as shown in fig. 7.8. It shows the development of boundary layer with distance from the source. Across this boundary layer, reactants transport to the surface and reaction by-products diffuse back into the main gas stream. The positive value of ΔG_1 of liquid indium at 860°C indicates that transformation of liquid indium to indium gas is not possible at this temperature [127]. It has been reported that the phase transformation of the indium to In_2O_3 in an O_2 atmosphere occurs through intermediate reactions. These are listed below [127, 129];



Due to the low melting point of indium ($\sim 160^\circ\text{C}$ at 1 atm) and low boiling point of In_2O (527°C at 1 atm), indium exists in liquid phase and In_2O exists in the vapor phase at the growth temperatures used in this work. Thus, the predominant evaporating

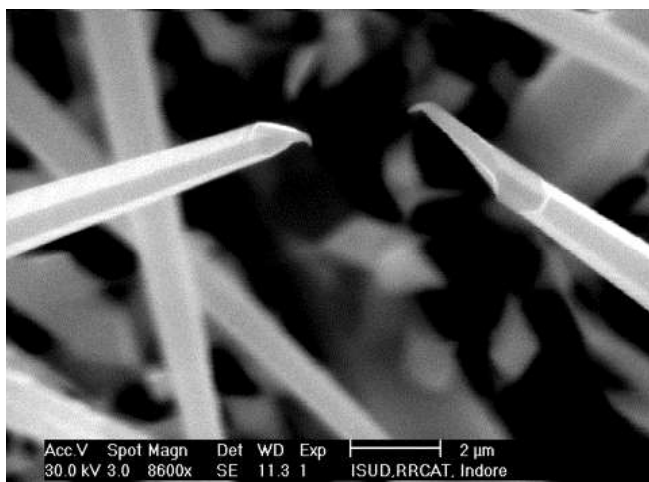


Figure 7.7. The SEM image of In₂O₃ microstructures shows the bending tips, which is related to the displacement of the catalyst particle from the apex due to growth related instability, resulting in the deflection of the growth direction.

Figure 7.7 shows the SEM image of the In₂O₃ micro-wires, where one sees that they grow straight and then taper gradually towards the top, with bending tips. The possible reason of this spontaneous bending could be related to the displacement of the catalyst particle from the apex due to growth related instability, resulting in the deflection of the growth direction [125]. There are various reports explaining the growth of these kinds of In₂O₃ structures in which the growth of In₂O₃ micro-structures is governed by Au-catalytic vapor-liquid-solid (VLS) mechanism in the initial stage and subsequently governed by self-catalytic VLS mechanism with continuous lateral growth, controlled by a vapor-solid (VS) mechanism [126-128].

In this work, growth temperature and the incoming reactant vapor concentration (distance from the source material) are the two parameters that are different between the samples. Based on these parameters and SEM images, we have pointed out two cases to explain our results (details of sample parameters are explained in fig. 7.2). Case I: When the substrate temperature increases while keeping the distance from the source constant; this contains three set of samples; 1) samples A1, B1 and C1, 2) samples A2, B2 and C2, and 3) samples A3, B3 and C3. Case II: When the substrate distance from the source

observed with slightly smaller length as compared to sample A1. In the case of sample B2, growth of thin nanosheets with some In_2O_3 nanowires (less than 100 nm diameter) is observed. Similar to sample A2, film like structure of In_2O_3 were observed in sample B3 (Figure not shown).

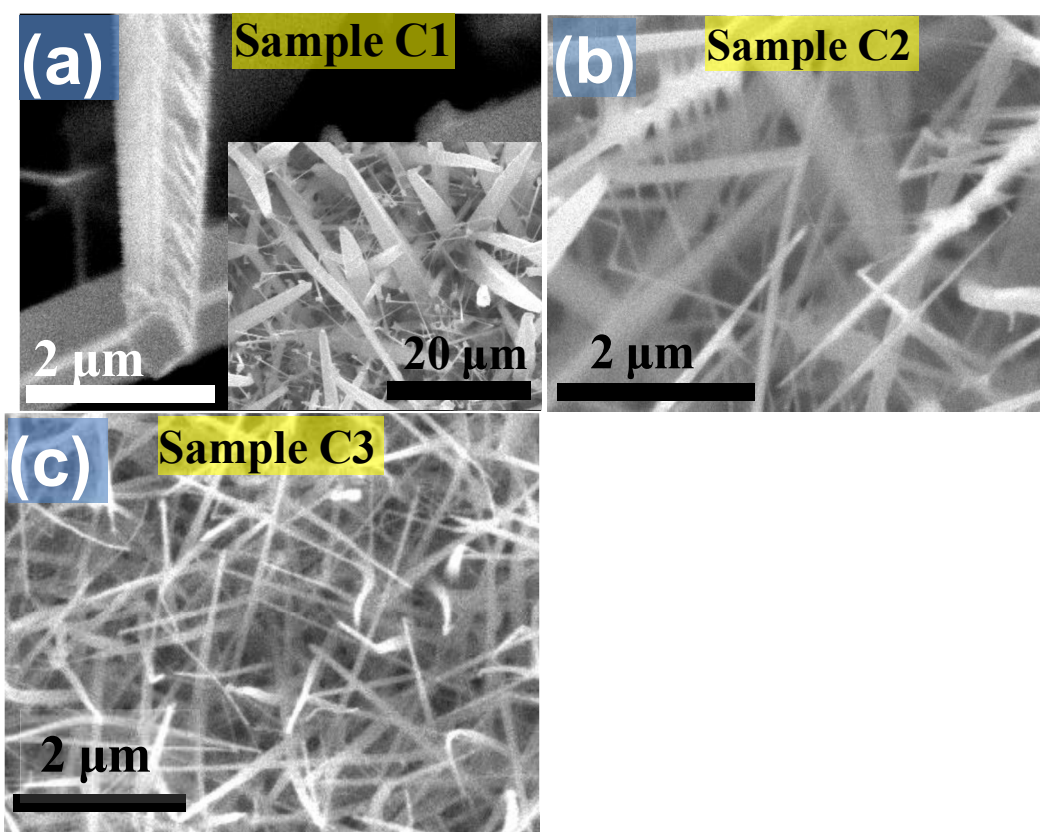


Figure 7.6. The SEM images of (a) In_2O_3 microwire structures, (b) In_2O_3 nanowire with branched structures and (c) In_2O_3 nanowires, grown in samples C1, C2 and C3 respectively.

Figures 7.6(a), (b) and (c) show the SEM pictures of sample C1, C2 and C3 respectively. Sample C1 shows the growth of In_2O_3 microwires with smaller lengths as compared to that in samples A1 and B1. Sample C2 shows an extensive growth of branched In_2O_3 nanowire structures which have backbone structures of about 200 nm wide. The In_2O_3 wires in the branches have diameters around tens of nanometer. In_2O_3 nanowires all over the sample (diameter of the nanowires varies 40-200 nm) are observed in sample C3.

7.4 SEM Results and growth mechanism

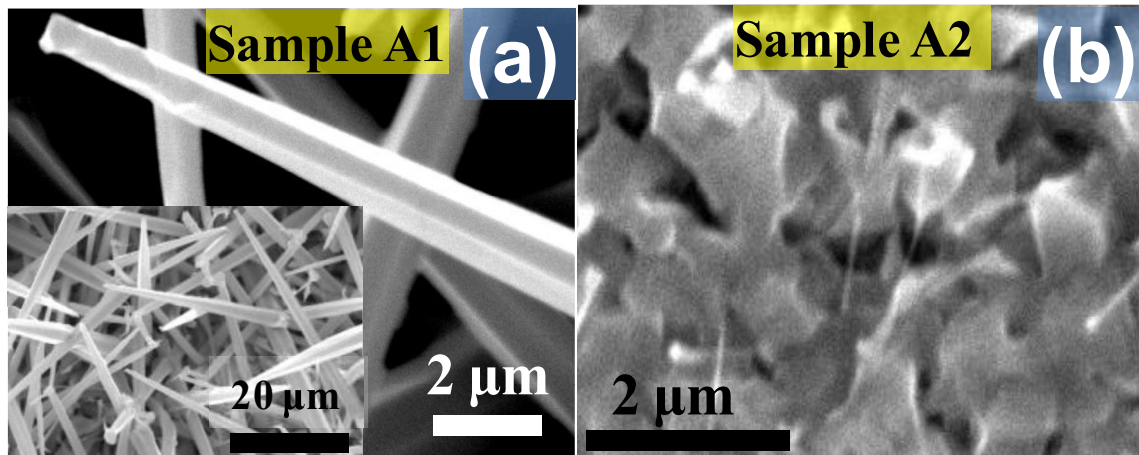


Figure 7.4. SEM images of (a) In_2O_3 microwire structures and (b) In_2O_3 film, grown in sample A1 and sample A2 respectively.

Figure 7.4 shows the SEM images of the as synthesized In_2O_3 wire structures grown on Si substrates. Figures 7.4(a) and 7.4(b) show the SEM picture of sample A1 and A2 respectively. Sample A1 shows an extensive growth of hexagonal cross section micro-wires with diameter of around $0.5\text{--}2\ \mu\text{m}$ near the tip region and length up to $100\ \mu\text{m}$. In_2O_3 film like structure along with some nanowires is observed in sample A2. In sample A3, similar structures as observed in sample A2 were observed (Figure not shown).

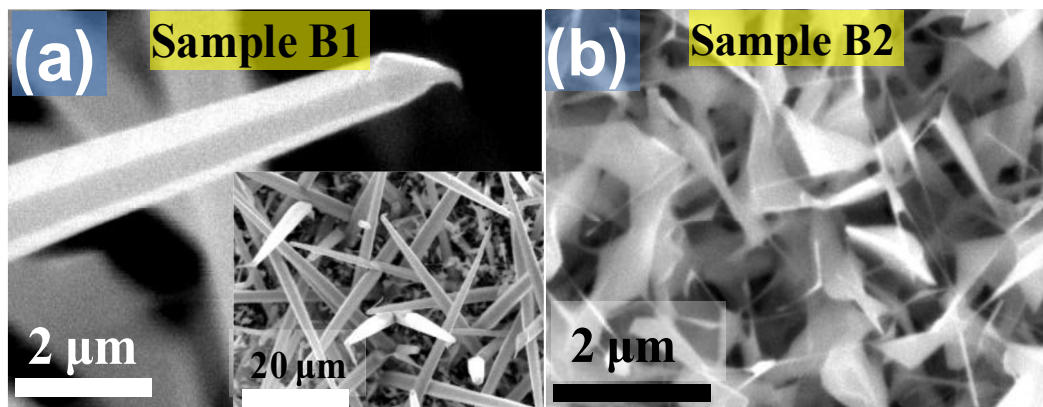


Figure 7.5. SEM images of (a) In_2O_3 microwire structures and (b) In_2O_3 nanowire with thin nanosheet structures, grown in sample B1 and sample B2 respectively.

Figures 7.5(a) and (b) show the SEM pictures of sample B1 and B2 respectively. In sample B1, the growth of hexagonal cross-section micro-wires similar to sample A1 is

were measured with 266 nm laser as the excitation source and a photo-multiplier tube as the detector.

7.3 XRD Results

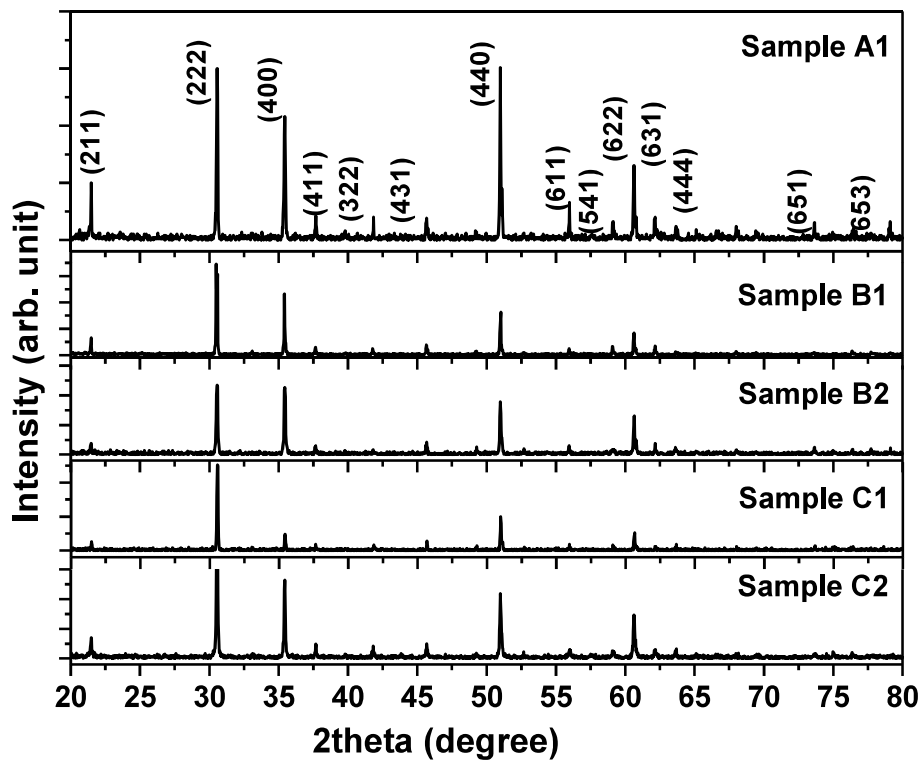


Figure 7.3. The GIXRD pattern of the as-synthesized In_2O_3 nano/micro structures for samples A1, B1, B2, C1 and C2.

The structure of the as-synthesized products was characterized by GIXRD. Figure 7.3 shows the GIXRD pattern of the In_2O_3 wire structures deposited on Si substrates for samples A1, B1, B2, C1 and C2. All the diffraction peaks in the pattern are indexed to body centered cubic In_2O_3 . They are in good agreement with the lattice constant $a=1.0118$ nm (JCPDS card no. 06-0416). All the XRD peaks have been indexed to the above structure thereby confirming the formation of single phase In_2O_3 .

and A3 (samples set A). The growth temperatures of sample A1, A2 and A3 were 875°C, 850°C and 825°C respectively. Two more growths were also carried out at indium source temperatures of 900°C and 925°C, with all other condition kept the same as in case of sample set A. These samples are denoted as B1, B2, B3 (samples set B) with growth temperatures of 900°C, 875°C, 850°C respectively and C1, C2, C3 (samples set C) with growth temperatures of 925°C, 900°C, 875°C respectively. The samples A1, B1 and C1 were put near the source (indium metal); hence growth temperatures were nearly equal to the source temperature. The details of the samples along with their distances from the source and growth temperatures are given in the fig. 7.2.

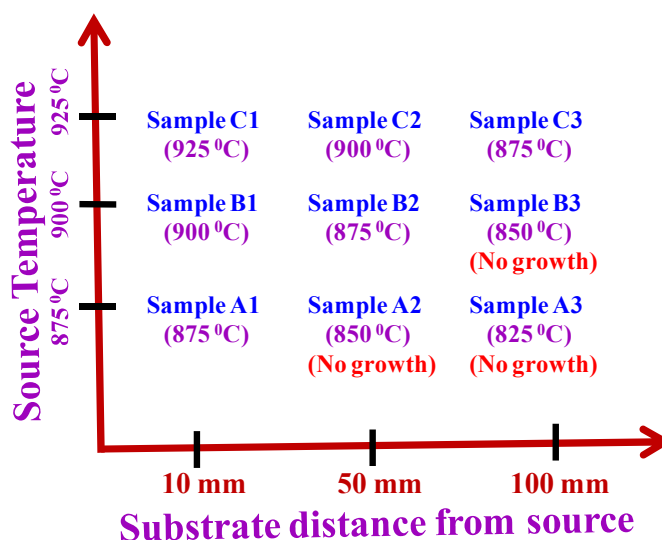


Figure 7.2. Details of the samples with the growth temperature (in parenthesis) and distance from the source. The source temperature (ST) is also shown in the Y-axis.

The structural properties and morphology of the as prepared products were characterized by Grazing Incidence X-Ray Diffraction (GIXRD) on Brukers D8 system with Cu K α radiation, Scanning Electron Microscopy (SEM) on Philips XL30CP, and Transmission Electron Microscopy (TEM) on Philips CM200 system. For the TEM measurements, In₂O₃ layer was scraped from the Si wafers, ultrasonically dispersed in methanol, and a drop was placed on a copper grid. The photo-luminescence (PL) spectra

tube of a tube furnace as shown in fig. 7.1. The furnace temperature defined in this work is the temperature of the centre of the furnace and temperature stability of the furnace was pre-calibrated within $\pm 2^\circ\text{C}$. The indium source was kept at the centre of the furnace; the source temperature was equal to the furnace temperature. The substrates were kept further downstream from the source. Since, the temperature gradient in the furnace was 5 degree/cm outward from the centre in the gas flow direction and samples were placed 10 mm, 50 mm and 100 mm away from the source (shown in fig. 7.1), the temperature difference between the samples was 25°C (fig. 7.2).

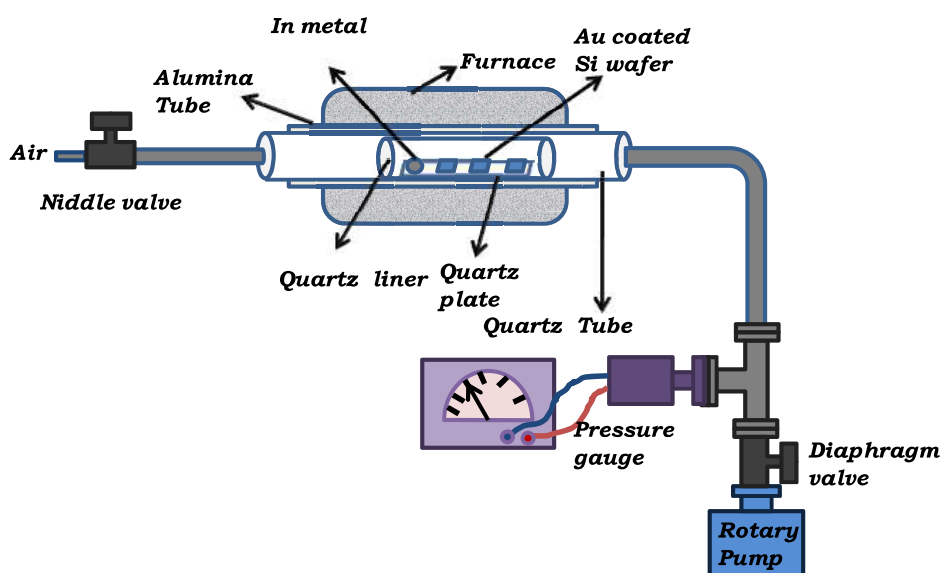


Figure 7.1. A schematic illustration of the experimental setup for the growth of In_2O_3 nano/micro structures.

After putting the source material and Si substrates, the furnace was evacuated up to 10^{-3} mbar and then its temperature was raised. After reaching 800°C , air (N_2 and O_2 in the ratio of 80/20) was leaked through a needle valve and the pressure was kept at 20 mbar. The growth was maintained for one hour at 875°C . After the reaction, the furnace was naturally cooled down to room temperature. A thick light yellow layer of In_2O_3 was observed on the surface of the Si substrate. These samples are denoted as Sample A1, A2

catalyzed ZnSe nanowires epitaxially grown on GaAs/GaP substrates [62, 120 and 122]. The control of the nanowire growth direction has several practical, technological and fundamental scientific implications [123, 124]. Considering these facts, dependence of the growth of In_2O_3 wires on the growth parameters have been investigated in detail using vapor transport method. In this work, two growth parameters: 1) growth temperature and 2) incoming reactant vapor concentration have been used to study the growth behavior of In_2O_3 wires. It has been found that as the growth temperature and incoming reactant vapor concentration were changed, various types of structures like thin nanosheet, branched wire structures, hexagonal shaped micro-wires and square cross-section nanowires were observed. Change in the incoming reactant vapor concentration at the same growth temperature showed two phenomena. First, diameter of the wires changed from micrometers to nanometers. Second, the growth directions of the wires changed from $\langle 111 \rangle$ to $\langle 001 \rangle$ respectively. The mechanism behind the observed growth characteristics is discussed. Optical properties have also been investigated in details by photo-luminescence experiments.

7.2 Experimental method

Indium wire was used as the indium source for the growth of In_2O_3 nanostructures. The Si (100) substrate (15 mm x 15 mm) was first cleaned by boiling in TCE (trichloroethylene), acetone, methanol and dried in nitrogen gas. They were then coated with about 10-20 nm of gold film by thermal evaporation at 10^{-6} Torr. Indium metal (~ 0.1 gm) and gold coated Si samples were placed on a quartz plate at distance of 10 mm, 50 mm and 100 mm from the indium source material as shown in fig.7.1. The quartz plate was inserted into a 25 mm quartz tube and this 25 mm quartz tube was inserted into another 42 mm quartz tube, which was then loaded into a 2 inch alumina

Chapter 7

Influence of growth parameters on the morphology and growth orientation of In_2O_3 wires

7.1 Introduction and background

Similar to $\beta\text{-Ga}_2\text{O}_3$, Indium oxide (In_2O_3) is also an important wide band gap ($E_g \approx 3.6\text{eV}$ at 300 K) transparent semiconductor. It is widely used in optoelectronic devices such as solar cells [100-101], flat panel display materials [102-103] and gas sensors [104-105]. Micro-/nanowires with hexagonal cross-section have attracted particular interest due to their optical properties and wide range of potential applications [106-108]. However, the investigations reported so far are limited to ZnO hexagonal resonators primary due to the difficulty in synthesizing high quality hexagonal microcavities with other materials. In recent years, one dimensional (1D) cubic In_2O_3 nanostructures have emerged as attractive photonic materials because of their hexagonal cross-section that allows whispering gallery mode (WGM) resonance. These are useful for lasing, sensing and optical modulation [109]. Most of the reported 1D nanostructures have been found to be of square cross section [110-116] and reports on hexagonal cross section 1-D In_2O_3 nanostructures are quite limited [109, 117 and 118].

Nanowires generally grow in the crystal directions that minimize the total free energy, which is mainly dominated by the surface free energy of the interface between the nanowire and the metal catalyst. Apart from the surface energy minimization, various factors like diameter of the wire, growth conditions and substrate crystal orientation also affect the growth orientation of the nanowires [119]. The dependence of growth direction on the diameter of the nanowires has been reported in detail for Si nanowires and Au-

by the time resolved PL technique and ultra fast pump probe technique. Hence, this leaves a scope for further investigation in this direction using these techniques.

micro/nanostructures. A strong dependence of PL emission band on the morphology of the structures has been observed. Further, no significant PL sensitivity to oxygen exposure has been observed in the PL measurements carried out at different oxygen partial pressure (similar to the ones carried out for β -Ga₂O₃ nanostructures). We conclude that the electrons and holes are localized in the donor and acceptor traps and hence PL from donor-acceptor pair transitions is observed. This localization makes the PL intensity insensitive to the changes on the surface of the nanostructure. Similar results have also been observed in the β -Ga₂O₃ nanostructures. In the case of sub bandgap excitation using 3.81 eV from He-Cd laser, PL is observed from the deep levels and is found insensitive to the surface modifications in the β -Ga₂O₃ nanostructures. Only self trap exciton transition and shallow DAP transition in the β -Ga₂O₃ nanostructures are found sensitive to the surface modifications in which carriers are in the conduction band or thermal equilibrium with the conduction band. Since both type of transition are not observed in the In₂O₃ micro/nanostructures, these nanostructures are found to be insensitive for the adsorption/desorption of the oxygen gas and hence unsuitable for applications to PL based sensors.

Our study indicates that there is a vast scope in the field of optical sensing in the oxide nanostructures, which can be an alternate method of gas sensing apart from the electrical ones. The available studies are reported only for few oxide materials (like ZnO, SnO₂) including this work on β -Ga₂O₃, and other oxide nanostructures are left unexplored. In spite of numerous studies already reported in the literature, the microscopic mechanisms of gas sensing are still not clearly understood. The microscopic mechanism of gas sensing requires full understanding of various recombination mechanisms in the material. These recombination mechanisms can be effectively probed

The effect of post growth annealing in different atmosphere on the structural and optical properties of β -Ga₂O₃ nanostructures have also been investigated. The PL study confirms the presence of defects on the surface of β -Ga₂O₃ nanostructures due to annealing in moist ambient. These effects have been found to be nonrecoverable. It has also been found that at high temperatures, adsorption of water dominates over the effects of other gases. O₂ partial pressure dependent PL study reveals that these permanent surface defects reduce the effective surface area on the surface of the nanostructures for the O₂ adsorption/desorption. This study highlights the issues that will be helpful to explore the applicability of β -Ga₂O₃ nanostructure in the moist environments at high temperatures.

Since Ga₂O₃ has large band gap, it has attracted large attention for applications to phosphors. Various methods have been reported for the doping in β -Ga₂O₃ to tune the energy of the luminescence band. Thermal annealing method has been used to grow the β -Ga₂O₃ nanostructures. The effect of doping, present in the GaAs substrate, on the luminescence band energy has been investigated. The PL spectra indicate that the impurities (doping) present in the GaAs substrates diffuse into the β -Ga₂O₃ nanostructures as dopants, thereby modifying the defect level structures of β -Ga₂O₃. Modification in the defect levels shifts the PL emission band of β -Ga₂O₃ nanostructures. The tuning of optical properties of β -Ga₂O₃ nanostructures indicates the possible applications of these nanostructures in optoelectronic nano-devices.

Detail growth mechanism of In₂O₃ micro/nanowires has been investigated using vapor transport method. It has been found that the morphology and growth directions of In₂O₃ micro/wires can be manipulated by controlling the growth parameters like growth temperatures and incoming reactant vapor concentrations. This work highlights a route to grow the In₂O₃ micro/nanostructures with a desired growth direction ($\langle 111 \rangle$ or $\langle 100 \rangle$) and morphology. Orange-yellow emission bands have been observed in the PL spectra of In₂O₃

large probability of getting trapped at the surface states. However, in the case of visible luminescence, both the electrons and holes are trapped in the donor and acceptor sites respectively and hence less prone to be affected by the surface trapping centers. The relatively smaller decrease in the visible luminescence is due to the fact that the electron concentration in the donor band is in thermal equilibrium with the conduction band. The equilibrium carrier concentration in the conduction band changes due to trapping at the surface defects and thus the intensity of the visible luminescence also decreases, but significantly less as compared to the UV luminescence. These results indicate that UV luminescence band is more prone to be effected by the surface defects as compared to the visible luminescence band.

Considering the close relationship between the presence of surface states and the intensity of the UV luminescence exist in β -Ga₂O₃, PL data has been analyzed for the nanostructures, synthesized by different techniques. Three growth methods (thermal annealing, thermal evaporation and vapor transport) have been used for the synthesis of β -Ga₂O₃ nanostructures. The structural, morphology and optical properties of the β -Ga₂O₃ nanostructures synthesized by these three techniques have been compared. The study shown that among all the three methods vapor transport method with dry N₂ carrier gas is the best method for the β -Ga₂O₃ nanostructures. The lack of morphology control and the presence of surface defects in the thermal annealing and thermal evaporation method make vapor transport, a more suitable method for the growth of good quality β -Ga₂O₃ nanostructures. In the vapor transport method, effects of different carrier gas (dry N₂ and moist N₂) have also been investigated. The effect of the surface defects on the oxygen sensitive PL properties of β -Ga₂O₃ nanostructures that arise due to the carrier gas has also been examined.

detail PL studies have been carried out on Gallium oxide (β -Ga₂O₃) and indium oxide (In₂O₃) nanostructures.

β -Ga₂O₃ nanostructures are used extensively for O₂ sensing. All the reported sensors are based on the principle of electrical conductivity. In this thesis, effect of O₂ adsorption/desorption on the PL properties of β -Ga₂O₃ nanostructures have been investigated in details. The PL spectra of β -Ga₂O₃ nanostructures consist of two emission bands centered at UV and visible region, which correspond to self trap exciton and shallow DAP transition respectively. It has been observed that both UV and visible luminescence intensity depend strongly on the ambient O₂ gas pressure. This intensity variation with ambient O₂ gas pressures is found to be repeatable and reversible. The change in the PL intensity with oxygen pressure has been fitted with the Langmuir equation, which relates adsorption/desorption of a gas on the surface of material with ambient gas pressure. Our results thus confirm the role of surface states, induced by the adsorption/desorption of O₂, in modifying the PL intensity. Considering the large surfaces to volume ratio in the nanostructures, which enhance the role of surface states in PL properties, modified band model have been proposed by inclusion of surface states. The experiment of sub-band gap excitation (with 3.81 eV) has also been carried out to identify the tentative location of the surface states inside the bandgap. All the observations have been explained by the proposed band model. These results provide an understanding of the gas adsorption/desorption related mechanism in β -Ga₂O₃ nanostructures and a PL based route for room-temperature sensing of O₂ by β -Ga₂O₃ nanostructures.

It has also been observed that the integrated intensity of UV PL band reduces about 8000 times, whereas the integrated intensity of visible PL band reduces only 80 times. According to our model, the UV band is more prone to be affected by the surface state trapping centers because the electrons in conduction band are mobile and hence have a

Chapter 8

Summary and future scope

Method of sensing via PL measurements is an alternative route of electrical conductivity based gas sensing. It enables us to get rid of the complications that arise due to the electrode fabrication and contact making. The working of these sensors is based on this fact that the photo-excited charge carriers (electron or hole) interact with the defect states on the surface of the nanostructure. If the carriers are trapped in deep traps located inside the bulk of the system, they cannot see the changes on the nanostructure surface and hence are not useful for sensing applications. The most important recombination mechanisms in the metal oxide materials are band to band transition, excitonic recombination, self trap exciton, shallow donor-acceptor pair (DAP) transitions, donor to valance band transition and conduction band to acceptor transition etc.. In all the cases charge carriers are either in the conduction/valance band or in thermal equilibrium with the conduction/valance band. In the conduction/valance band, charge carriers can freely propagate in the crystal and because of large surface to volume ratio in the nanostructures, it can easily respond to the surface change due to gas adsorption/desorption. The adsorption and desorption of the gas on the surface of the nanostructure produce surface defects, which lead to capture or release of these charge carriers. This capture and release of the electrons can be directly observed in the form of PL intensity variation. The presence of surface defects are related to the growth parameters and post growth processing, all of which can also be probed effectively using PL techniques. Thus, the complete understanding of the knowledge of the luminescence mechanism in a material is necessary to explore the applicability of the material for applications and devices. Considering the importance of PL technique, in this thesis,

137. Y. X. Chen, L. J. Campbell and W. L. Zhou, *Journal of Crystal Growth* **270**, 505 (2004).
138. C. S. Lao, P. X. Gao, R. S. Yang, Y. Zhang, Y. Dai and Z. L. Wang, *Chemical Physics Letters* **417**, 359 (2005).
139. Z. L. Wang, X. Y. Kong and J. M. Zuo, *Phys. Rev. Lett.* **91**(18), 185502 (2003).
140. Y. Hao, G. Meng, C. Ye and L. Zhang, *Crystal Growth & Design* **5**(4), 1617 (2005).
141. H. J. Zhou, W. P. Cai and L. D. Zhang, *Appl. Phys. Lett.* **75**, 495 (1999).
142. C. H. Liang, G. W. Meng, Y. Lei, F. Phillipp and L. D. Zhang, *Adv. Mater.* **13**, 1330 (2001).
143. M. S. Lee, W. C. Choi, E. K. Kim, C. K. Kim and S. K. Min, *Thin Solid Films* **279**, 1 (1996).
144. K. C. Kam, F. L. Deepak, A. K. Cheetham and C. N. Rao, *Chem. Phys. Lett.* **397**, 329 (2004).
145. H. Q. Cao, X. Q. Qiu, Y. Liang and Q. M. Zhu, *Appl. Phys. Lett.* **83**, 761 (2003).
146. T. S. Ko, C. P. Chu, J. R. Chen, T. C. Lu, H. C. Kuo and S. C. Wang, *Journal of Crystal Growth* **310**, 2264 (2008).

125. C. J. Chen, M. Y. Chern, C. T. Wu and C. H. Chen, *Materials Research Bulletin* **45**, 230 (2010).
126. N. Singh, T. Zhang and P. S. Lee, *Nanotechnology* **20**, 195605 (2009).
127. S. T. Jean and Y. C. Her, *Crystal Growth & Design* **10** (5), 2104 (2010).
128. Y. G. Yan, Y. Zhang, H. B. Zeng and L. D. Zhang, *Crystal Growth & Design* **7**(5), 940 (2007).
129. C. A. Pan and T. P. Ma, *J. Electrochem. Soc.* **1981**, 128 (1953).
130. *Organometallic vapor-Phase Epitaxy: Theory and Practice*; Gerald, B.; Stringfellow Academic Press 1999 and *Chemical Vapour Deposition; An Integrated Engineering Design for Advanced Materials*; Xu, Y.; Yan, X. T. Springer-Verlag London 2010.
131. X. Xu, M. Wu, M. Asoro, P. J. Ferreira and D. L. Fan, *Crystal Growth & Design* **12**(10), 4829 (2012).
132. C. Ma and L. Wang, *Adv. Mater.* **17**, 1 (2005).
133. Y. Ding, C. Ma and Z. L. Wang, *Adv. Mater.* **16**(19), 1740 (2004).
134. C. Ye, X. Fang, Y. Hao, X. Teng and L. Zhang, *J. Phys. Chem. B* **109**, 19758 (2005).
135. S. H. Dalal, D. L. Baptista, K. B. K. Teo, R. G. Lacerda, D. A. Jefferson and W. I. Milne, *Nanotechnology* **17**, 4811 (2006).
136. C. Y. Nam, D. Tham and J. E. Fischer, *Mater. Res. Soc. Symp. Proc.* **1058**, JJ04-03 (2008).

112. H. J. Chun, Y. S. Choi, S. Y. Bae and J. Park, *Appl. Phys. A: Mater. Sci. Process.* **81**, 539 (2005).
113. C. Li, D. Zhang, X. Liu, S. Han, T. Tang, J. Han and C. Zhou, *Appl. Phys. Lett.* **82**, 1613 (2003).
114. Y. Li, Y. Bando and D. Golberg, *Adv. Mater.* **15**, 581 (2003).
115. D. H. Zhang, C. Li, S. Han, X. Liu, T. Tang, W. Jin and C. Zhou, *Appl. Phys. Lett.* **82**, 112 (2003).
116. C. H. Liang, G. W. Meng, Y. Lei, F. Phillipp and L. D. Zhang, *Adv. Mater.* **13**, 1330 (2001).
117. C. J. Chen, W. L. Xu and M. Y. Chern, *Advanced Materials* **19**, 3012 (2007).
118. J. S. Jeong and J. Y. Lee, *Materials Letters* **65**, 1693 (2011).
119. S. A. Fortuna and X. Li, *Semicond. Sci. Technol.* **25**, 024005 (2010).
120. V. Schmidt, S. Senz and U. Gosele, *Nano Lett.* **59**, 31 (2005).
121. Y. F. Chan, X. F. Duan, S. K. Chan, I. K. Sou, X. X. Zhang and N. Wang, *Appl. Phys. Lett.* **83**, 2665 (2003).
122. Y. Cai, S. K. Chan, I. K. Sou, Y. F. Chan, D. S. Su and N. Wang, *Adv. Mater.* **18**, 109 (2006).
123. W. T. Moon, K. S. Lee, Y. K. Jun, H. S. Kim and S. H. Hong, *Sensors and Actuators B* **115**, 123 (2006).
124. Y. V. Kaneti, Z. Zhang, J. Yue, Q. M. Zakaria, C. Chen, X. Jiang and A. Yu, *Phys Chem Chem Phys.* **16**, 11471 (2014).

98. G. Wang, J. Park, X. Kong, P. R. Wilson and Z. Chen, J. Ahn, *Crys. Growth & Design* **8**, 1940 (2008).
99. K. Shimamura, E. G. Villora, T. Ujiie and K. Aoki, *Appl. Phys. Lett.* **92**, 201914 (2008).
100. K. Sreenivas, T. S. Rao, A. Mansingh and S. Chandra, *J. Appl. Phys.* **57**, 384 (1985).
101. I. Hamberg and C. G. Granqvist, *J. Appl. Phys.* **60**, 123 (1986).
102. X. Li, M. W. Wanlass, T. A. Gessert, K. A. Emery and T. J. Coutts, *Appl. Phys. Lett.* **54**, 2674 (1989).
103. Y. Shigesato, S. Takaki and T. Haranoh, *J. Appl. Phys.* **71**, 3356 (1992).
104. J. Tamaki, C. Naruo, Y. Yamamoto and M. Matsuoka, *Sens. Actuators B* **83**, 190 (2002).
105. M. Liess, *Thin Solid Films* **410**, 183 (2002).
106. T. Voss, G. T. Svacha, E. Mazur, S. Müller, C. Ronning, D. Konjhozic and F. Marlow, *Nano Lett.* **7**, 3675 (2007).
107. H. X. Jiang, J. Y. Lin, K. C. Zeng and W. Yang, *Appl. Phys. Lett.* **75**, 763 (1999).
108. M. H. Huang, S. Mao, H. Feick, H. Yan, Y. Wu, H. Kind, E. Weber, R. Russo and P. Yang, *Science* **292**, 1897 (2001).
109. H. Dong, Z. Chen, L. Sun, J. Lu, W. Xie, H. H. Tan, C. Jagadish and X. Shen, *Appl. Phys. Lett.* **94**, 173115 (2009).
110. X. Y. Kong and Z. L. Wang, *Solid State Commun.* **128**, 1 (2003).
111. J. Lao, J. Huang, D. Wang and Z. Ren, *Adv. Mater.* **16**, 65 (2004).

85. C. Y. Zhi, X. D. Bai and E. G. Wang, *Appl. Phys. Lett.* **85**, 1802 (2004).
86. J. Zhang, F. Jiang and L. Zhang, *Physics Letters A* **322**,363 (2004).
87. X. Xiang, C. B. Cao and H. S. Zhu, *Journal of Crystal Growth* **279**, 122 (2005).
88. K.F. Cai, S. Shen, C. Yan and S. Bateman, *Current Applied Physics* **8**, 363 (2008).
89. J. Zhang, X. Zhang, L. Chen, J. Xu, L. You, H. Ye and D. Yu, *Appl. Phys. Lett.* **90**, 233104 (2007).
90. J. Giber, I.V. Perczel, J. Gerblinger, U. Lampe and M. Fleischer, *Sensors and Actuators B* **18-19**, 113 (1994).
91. E. G. Villora, M. Yamaga, T. Inoue, S. Yabasi, Y. Masui, T. Sugawara and T. Fukuda, *Jpn. J. Appl. Phys.* **41**, L622 (2002).
92. T. Harwing, F. Kelledonk and S. Slappendel, *J. Phys. Chem. Solids* **39**, 675 (1978).
93. S.M. Prokes, W.E. Carlos and E.R. Glaser, *International Journal of Nanotechnology* Vol. **5**, No.4/5 475 (2008).
94. F. Reti, M. Fleischer, H. Meixner and J. Giber, *Sensors and Actuators B* **18-19**, 138 (1994).
95. Y. Pan, C. Liu, D. Mei and Q. Ge, *Langmuir* **26**(8), 5551 (2010).
96. E. Nogales, B. Sanchez, B. Mendez and J. Piqueras, *Superlattice, Microstructures* **45**, 156 (2009).
97. R. Jalilian, M. M. Yazdanpanah, B. K. Pradhan and G. U. Sumanasekera, *Chem. Phys. Lett.* **426**, 393(2006).

73. Y. Huang, S. Yue, Z. Wang, Q. Wang, C. Shi, Z. Xu, X. D. Bai, C. Tang and C. Gu, J. Phys. Chem. B **110**, 796-800 (2006).
74. P. Feng, J. Y. Zhang, Q. Wan and T. H. Wang, J. Appl. Phys. **102**, 074309 (2007).
75. X. Xiang, C. B. Cao, Y. J. Guo and H. S. Zhu, Chem. Phys. Lett. **378**, 660 (2003).
76. I. Bhaumik, R. Bhatt, S. Ganesamoorthy, A. Saxena, A. K. Karnal, P. K. Gupta, K. Sinha and S. K. Deb, Appl. Optics **50**, 6006 (2011).
77. L. Binet and D. Gourier, J. Phys. Chem.Solids **59**, 1241 (1998).
78. Urbach and F., Wiener, Ber. Ila, **139**, 363 (1930).
79. J. Langmuir The Adsorption of Gases on Plane Surfaces of Glass, Mica and Platinum. J.Am. Chem. Soc. 40, 1361 (1918) and Coalbed Methane: Principles and Practice by R. E. Rogers (Prentice Hall Petroleum Engineering) chapter 3 (Sorptions) page no.143-189 (2007).
80. J. Zhang, B. Li, C. Xia, G. Pei, Q. Deng, Z. Yang, W. Xu, H. Shi, F. Wu, Y. Wu and J. Xu, Journal of Physics and Chemistry of Solids **67**, 2448 (2006).
81. Y. P. Song, H. Z. Zhang, C. Lin, Y. W. Zhu, G. H. Li, F. H. Yang and D. P. Yu, Phys. Rev. B **69**, 075304 (2004).
82. T. Oshima, T. Okunu and S. Fujita, Jap. J. Appl.Phys, Vol. **46**, 7217 (2007).
83. R. Jangir, S. Porwal, P. Tiwari, P. Mondal, S. K. Rai, T. Ganguli, S. M. Oak and S. K. Deb, J. App. Phys. **112**, 034307 (2012).
84. R. Jangir, T. Ganguli , S. Porwal, P. Tiwari, S. K. Rai, I. Bhaumik, L. M. Kukreja, P. K. Gupta and S. K. Deb, J. App. Phys. **114** (7), 074309 (2013).

59. M. Ghosh, R. S. Ningthoujam, R. K. Vatsa, D. Das, V. Nataraju, S. C. Gadkari, S. K. Gupta and D. Bahadur, *J. Appl. Phys.* **110**, 054309 (2011).
60. G. Faglia, C. Baratto, G. Sberveglieri, M. Zha and A. Zappettini, *Appl. Phys. Lett.* **86**, 011923 (2005).
61. S. Barth, F. H. Ramirez, J. D. Holmes and A. R. Rodriguez, *Progress in Materials Science* **55**, 563 (2010).
62. N. Wang, Y. Cai and R. Q. Zhang, *Materials Science and Engineering R* **60**, 1 (2008).
63. R. S. Wagner and W. C. Ellis, *Appl. Phys. Lett.* **4**, 89 (1964).
64. S. Y. Bae, H. W. Seo and J. H. Park, *J. Phys. Chem. B* **108**, 5206 (2004).
65. X. Liu, C. Li, S. Han, J. Han and C. W. Zhou, *Appl. Phys. Lett.* **82**, 1950 (2003).
66. J. M. Wu, H. C. Shih, W. T. Wu and Y. K. Tseng, I. C. Chen, *J. Cryst. Growth* **281**, 384 (2005).
67. Z. R. Dai, J. L. Gole, J. D. Stout and Z. L. Wang, *J. Phys. Chem. B* **106**, 1274 (2002).
68. L. Dai, X. L. Chen, J. K. Jian, M. He, T. Zhou and B. Q. Hu, *Appl. Phys. A Mater. Sci. Process.* **75**, 687 (2002).
69. P. C. Chang, Z. Y. Fan, W. Y. Tseng, A. Rajagopal and J. G. Lu, *Appl. Phys. Lett.* **87**, 222102 (2005).
70. M. Z. Rahman, *International Journal of Renewable Energy Research*, Vol. **2**, No. **1**, 117 (2012).
71. R. Hall, *Physics Review* **87**, 387 (1952).
72. W. Shockley and W. Read, *Physical Rev.* **87**, 835 (1952).

47. J. G. Lu, P. Chang and Z. Fan, *Materials Science and Engineering R* **52**, 49 (2006).
48. M. Ogita, K. Higo, Y. Nakanishi and Y. Hatanaka, *Applied Surface Science* **175-176**, 721 (2001).
49. Z. Liu, T. Yamazaki, Y. Shen, T. Kikuta, N. Nakatani and Y. Li, *Sensors and Actuators B* **129**, 666 (2008).
50. K. J. Choi and H. W. Jang, *Sensors* **10**, 4083 (2010).
51. M. Law, H. Kind, B. Messer, F. Kim and P.D. Yang, *Angew. Chem. Int. Ed.* **41**, 2405 (2002).
52. J. D. Prades, R. Jimenez-Diaz, F. Hernandez-Ramirez, S. Barth, A. Cirera, A. Romano-Rodriguez, S. Mathur and J.R. Morante, *Sens. Actuat. B* **140**, 337 (2009).
53. L. Peng, Q. Zhao, D. Wang, J. Zhai, P. Wang, S. Pang and T. Xie, *Sens. Actuat. B* **136**, 80 (2009).
54. Z. Fan and J.G. Lu, *Appl. Phys. Lett.* **86**, 123510 (2005).
55. P. Feng, X. Y. Xue, Y. G. Liu, Q. Wan and T. H. Wang *Appl. Phys. Lett.* **89**,112114 (2006).
56. S. Bianchi, E. Comini, M. Ferroni, G. Faglia, A. Vomiero and G. Sberveglieri *Sensors and Actuators B* **118**, 204 (2006).
57. C. Li, D.H. Zhang, X.L. Liu, S. Han, T. Tang, J. Han and C.W. Zhou, *Appl. Phys. Lett.* **82**, 1613 (2003).
58. D. H. Zhang, Z.Q. Liu, C. Li, T. Tang, X.L. Liu, S. Han, B. Lei and C.W. Zhou, *Nano Lett.* **4**, 1919 (2004).

36. M. V. Artemyev, U. Woggon, R. Wannemacher, H. Jaschinski and W. Langbein, *Nano Lett.* **1**, 309 (2001).
37. T. Nobis and M. Grundmann, *Phys. Rev. A* **72**, 063806 (2005).
38. J. Z. Liu, S. Lee, Y. H. Ahn, J. Y. Park, K. H. Koh and K. H. Park, *Appl. Phys. Lett.* **92**, 263102 (2008).
39. T. Nobis, E. M. Kaidashev, A. Rahm, M. Lorenz and M. Grundmann, *Phys. Rev. Lett.* **93**, 103903 (2004).
40. H. Dong, S. Sun, L. Sun, W. Xie, L. Zhou, X. Shen and Z. Chen, *Appl. Phys. Lett.* **98**, 011913 (2011).
41. H. Dong, L. Sun, S. Sun, W. Xie, L. Zhou, X. Shen and Z. Chen *Appl. Phys. Lett.* **97**, 223114 (2010).
42. H. Dong, Z. Chen, L. Sun, J. Lu, W. Xie, H. H. Tan, C. Jagadish and X. Shen *Phys. Status Solidi C* **7**, No. 6, 1672 (2010).
43. M. Passlack, E. F. Schubert, W. S. Hobson, M. Hong, N. Moriya, S. N. G. Chu, K. Konstadinidis, J. P. Mannaerts, M. L. Schnoes and G. J. Zydzik, *J. Appl. Phys.* **77**, 686 (1995).
44. J. J. Coleman, A. C. Bryce and C. Jagadish *Semiconductors and Semimetals*, Volume 86, Burlington: Academic Press, (2012)
45. E. Nogales, J. Á. García, B. Méndez and J. Piqueras, *Appl. Phys. Lett.* **91**, 133108 (2007).
46. X. J. Huang and Y. K. Choi, *Sensors and Actuators B* **122**, 659 (2007).

24. M.Y. Liao, Y. Koide, J. Alvarez, M. Imura and J.P. Kleider, *Phys. Rev. B* **78**, 045112 (2008).
25. D. Zhang, C. Li, S. Han, X. Liu, T. Tang, W. Jin and C. Zhou, *Appl. Phys. A* **77**, 163 (2003).
26. D. H. Zhang, C. Li, S. Han, X.L. Liu, T. Tang, W. Jin and C.W. Zhou, *Appl. Phys. Lett.* **82**, 112 (2003).
27. C. Li, D. H. Zhang, S. Han, X.L. Liu, T. Tang and C.W. Zhou, *Adv. Mater.* **15**, 143 (2003).
28. P. Feng, J. Y. Zhang, Q. H. Li and T. H. Wang, *Appl. Phys. Lett.* **88**, 153107 (2006)
29. T. Nobis, E. M. Kaidashev, A. Rahm, M. Lorenz and M. Grundmann, *Phys Rev Lett.* **93**, 103903 (2004).
30. H. Dong, Z. Chen, L. Sun, J. Lu, W. Xie, H. H. Tan, C. Jagadish and X. Shen, *App. Phys. Lett.* **94**, 173115 (2009).
31. C. Czekalla, C. Sturm, R. Schmidt-Grund, B. Q. Cao, M. Lorenz and M. Grundmann, *Appl. Phys. Lett.* **92**, 241102 (2008).
32. V. N. Astratov, J. P. Franchak and S. P. Ashili, *Appl. Phys. Lett.* **85**, 5508 (2004).
33. L. Maleki, A. A. Savchenko, A. B. Matsko and V. S. Ilchenko, *Proc. SPIE* 5435, 178 (2004).
34. A. Francois and M. Himmelhaus, *Appl. Phys. Lett.* **92**, 141107 (2008).
35. D. K. Armani, T. J. Kippenberg, S. M. Spillane and K. J. Vahala, *Nature (London)* **421**, 925 (2003).

13. T. Miyata, T. Nakatani and T. Minami, *Journal of Luminescence*, **87-89**, 1183 (2000).
14. E. Nogales, J. Á. García, B. Méndez and J. Piqueras, *J. Appl. Phys.*, **101**, 033517 (2007).
15. G. Sinha and A. Patra, *Chemical Physics Letters*, **473**, 151 (2009).
16. T. S. Ko, C. P. Chu, J. R. Chen, T. C. Lu, H. C. Kuo and S. C. Wang, *Journal of Crystal Growth* **310** 2264 (2008).
17. Q. Zhao, H. Z. Zhang, Y. W. Zhu, S. Q. Feng, X. C. Sun, J. Xu and D. P. Yua, *Appl. Phys. Lett.*, **86**, 203115 (2005).
18. G. Shen, Y. Bando, B. Liu, D. Golberg and C. J. Lee, *Adv. Funct. Mater.*, **16**, 410 (2006).
19. S. Fan, M. G. Chapline, N. R. Franklin, T. W. Tomblor, A. M. Cassell and H. Dai, *Science*, **28**, 3512 (1999).
20. K. B. K. Teo, M. Chhowalla, G. A. J. Amaratunga, W. I. Milne, G. Pirio, P. Legagneux, F. Wyczisk, D. Pribat and D. G. Hasko, *Appl. Phys. Lett.* **80**, 2011 (2002).
21. G. Sinha, A. Datta, S. K. Panda, P. G. Chavan, M. A. More, D. S. Joag and A. Patra, *J. Phys. D: Appl. Phys.* **42**, 185409 (2009).
22. H. Jia, Y. Zhang, X. Chen, J. Shu, X. Luo, Z. Zhang and D. Yu, *Appl. Phys. Lett.* **82**, 4146 (2003).
23. Y. Jiang, W.J. Zhang, J.S. Jie, X.M. Meng, X. Fan and S.T. Lee, *Adv. Funct. Mater.* **17**, 1795 (2007).

References

1. Z. L. Wang, Nanowires and Nanobelts Vol I, Kluwer Academic, New York, (2003).
2. X. Fang and L. Zhang, J. Mater. Sci. Technol., Vol.22 No.1, (2006).
3. P. J. Pauzauskie and P. Yang, Materials today Vol. 9, No. 10, 36 (2006).
4. H. E. Schaefer, Nanoscience: The Science of the Small in Physics, Engineering, Chemistry, Biology and Medicine (Springer-Verlag Berlin Heidelberg (2010)).
5. K.E. Drexler, Engines of creation: The coming era of nanotechnology, (Oxford University Press, Oxford, (1986)).
6. K.E. Drexler, C. Terson and G. Pergamit, Unbounding the Future: The Nanotechnology Revolution (Morrow, New York, (1991)).
7. K.E. Drexler, Nanosystems: Molecular Machinery, Manufacturing, and Computation, (Wiley, New York, (1992)).
8. C. Soci, A. Zhang, X. Y. Bao, H. Kim and Y. Lo, D. Wang, Journal of Nanoscience and Nanotechnology Vol.10, 1 (2010).
9. E. Lai, W. Kim and P. Yang, Nano Res **1** 128 (2008).
10. S. Xu, C. Xu, Y. Liu, Y. Hu, R. Yang, Q. Yang, J. H. Ryou, H. Kim, Z. Lochner, S. Choi, R. Dupuis and Z. L. Wang, Adv. Mater. **22**, 4749 (2010).
11. R. Könenkamp, Robert C. Word and C. Schlegel, Appl. Phys. Lett., **85**, 24, (2004).
12. T. Zhang, R. Liang, L. Dong, J. Wang, J. Xu and C. Pan, Nano Research Volume **8**, Issue 8, 2676 (2015).